University of Wollongong

Research Online

University of Wollongong Thesis Collection 2017+

University of Wollongong Thesis Collections

2021

Dosimetry of Photon and Proton MRI Guided Radiotherapy Beams using Silicon Array Dosimeters

Trent James Causer
University of Wollongong

Follow this and additional works at: https://ro.uow.edu.au/theses1

University of Wollongong

Copyright Warning

You may print or download ONE copy of this document for the purpose of your own research or study. The University does not authorise you to copy, communicate or otherwise make available electronically to any other person any copyright material contained on this site.

You are reminded of the following: This work is copyright. Apart from any use permitted under the Copyright Act 1968, no part of this work may be reproduced by any process, nor may any other exclusive right be exercised, without the permission of the author. Copyright owners are entitled to take legal action against persons who infringe their copyright. A reproduction of material that is protected by copyright may be a copyright infringement. A court may impose penalties and award damages in relation to offences and infringements relating to copyright material. Higher penalties may apply, and higher damages may be awarded, for offences and infringements involving the conversion of material into digital or electronic form.

Unless otherwise indicated, the views expressed in this thesis are those of the author and do not necessarily represent the views of the University of Wollongong.

Recommended Citation

Causer, Trent James, Dosimetry of Photon and Proton MRI Guided Radiotherapy Beams using Silicon Array Dosimeters, Doctor of Philosophy thesis, School of Physics, University of Wollongong, 2021. https://ro.uow.edu.au/theses1/1420

Research Online is the open access institutional repository for the University of Wollongong. For further information contact the UOW Library: research-pubs@uow.edu.au

Dosimetry of Photon and Proton MRI Guided Radiotherapy Beams using Silicon Array Dosimeters

Trent James Causer, Bachelor of Medical Radiation Physics (Honours)

This thesis is presented as required for the conferral of the degree:

Doctor of Philosophy

Supervisors:
Senior Professor Peter Metcalfe & Doctor Brad M. Oborn & Associate Professor Susanna Guatelli

The University of Wollongong
School of Physics

December, 2021

This research has been conducted with the support of an Australian Government Research Training Program Scholarship.

Declaration

I, *Trent James Causer, Bachelor of Medical Radiation Physics (Honours)*, declare that this thesis is submitted in fulfilment of the requirements for the conferral of the degree *Doctor of Philosophy*, from the University of Wollongong, is wholly my own work unless otherwise referenced or acknowledged. This document has not been submitted for qualifications at any other academic institution.

Trent James Causer, Bachelor of Medical Radiation Physics (Honours)

December, 2021

Abstract

The integration of online magnetic resonance imaging (MRI) with photon and proton radiotherapy has potential to overcome the soft tissue contrast limitations of the current standard of care kV-image guided radiotherapy in some challenging treatment sites. By directly visualising soft tissue targets and organs at risk, removing the dependence on surrogates for image guidance, it is expected there will be a decrease in the geometric uncertainties related to daily patient setup. This new approach to image guided radiotherapy presents unique challenges due to the permanent magnetic field of the integrated MRI unit. The trajectory of charged particles including dose depositing secondary electrons are perturbed by the magnetic field, adding to the challenge of calculating the patient dosimetry and validating the calculation with measurement as is standard practice in radiotherapy. The magnetic field may also effect the operation and response of radiation detectors and a method of accurately characterising the influence of the magnetic field on detector response and operation is required.

This thesis reports progress made towards real time high spatial resolution dosimetry of photon and proton MRI guided radiotherapy beams using novel monolithic silicon detectors designed at the Centre for Medical Radiation Physics (CMRP). One challenge in experimentally characterising the magnetic field effects on a radiation detectors operation is how to perform dosimetry measurements with and without a magnetic field of varying strength and orientation from a single radiation source as this is not feasible on existing MRI linacs with a permanent magnetic field of fixed strength. A bespoke semi-portable magnet device was developed to meet this need. The device employs an adjustable iron yoke and focusing cones to vary the magnetic field of the central volume, a 0.3 T field can be achieved for volume to 10 x 10 x 10 cm^3 and up to a 1.2 T for a volume of at least 3 x 3 x 3 cm^3. The device is designed to be used with a clinical linear accelerator in both inline and perpendicular magnetic field orientations to meet the challenge of detector characterisation. The performance of the magnetic field generated by the device was within ±2 % of finite element modelling predictions of all configurations tested.

Dosimetric characterisation of a high spatiotemporal resolution monolithic silicon strip detector mounted to a flexible polymide carrier is presented with preliminary work towards determining optimal detector packaging for use in 1.2 T magnetic field carried out using the semi-portable magnet device with a clinical Varian 2100iX linear accelerator.

In an MRI guided proton radiotherapy system the proton beam is deflected via the Lorentz force, creating unique challenges in calculating the patient dosimetry and validating the calculation with measurement. The first experimental application of a high spatiotemporal resolution monolithic silicon array detector for proton Bragg peak detection of proton pencil beams of clinical energy and size in a 0.95 T magnetic is presented. The lateral shift of the Bragg peak induced by the 0.95 T magnetic field were mapped out accordingly and a Monte Carlo simulation was used to aid in interpretation of the experimental results.

The final sections of the thesis present the development of a device for characterising the coincidence of the imaging, radiation and optical isocenter for the Australian MRI-Linac. The alignment of the imaging and radiation isocenter is an essential component of linac commissioning and quality assurance (QA) program, as any geometrical offset between them results in a population wide geometrical error for all image-guided treatments on that machine. The widely used Winston-Lutz method (WL) typically uses a mega voltage (MV) imaging panel or multiple film exposures. MV imaging panels are not available on all commercial MR-linacs and using multiple films is time consuming potentially restricting the frequency the test may be performed. The final design of the device uses a pixelated monolithic silicon array detector to identify the beam central axis (CAX), the detector is mounted in a PMMA phantom containing MR visible gel around the detector with 10 MR fiducials within 3 cm radial distance of the centre of the phantom used to locate the MRI imaging isocenter.

Acknowledgments

This thesis has allowed me the opportunity to meet a community of incredible individuals, whom have supported and encouraged me throughout my PhD journey. The experiences of the past few years have inspired my passion for both academic research and clinical medical physics alike. I would like to first thank my supervisors. Senior Professor Peter Metcalfe, thank you for all your guidance, always making experimental work enjoyable and ensuring I am maintaining a high caffeine intake. Dr Brad Oborn thank you for your encouragement and support, your enthusiasm for exploring ideas and your patience. Associate Professor Susanna Guatelli thank you for your support, particularly in the beginning of my PhD studies, the accountability of the routine Geant4 meetings was an essential source of motivation.

I would like to thank all the staff at the Centre for Medical Radiation Physics (CMRP) particularly Distinguished Professor Anatoly Rosenfeld, whose support for all the students cannot be overstated. Thank you Associate Professor Marco Petasecca, Dr Iolanda Fuduli, Dr Dean Cutajar and Karen Ford for all your help.

I would like to thank the staff that have helped me at the Ingham Institute and Liverpool hospital, especially Associate Professor Lois Holloway, Dr. Urszula Jelen, Bin Dong, Dr. Michael Jameson and Armia George. In particular I want to thank Jarrad Begg for always taking the extra time to always explain the finer details and for being an exceptional role model.

Thank you to all my colleagues at the Illawarra Cancer Care Centre, especially Professor Martin Carolan for providing the workplace support for me to complete this thesis and Dean Wilkinson for his support and encouragement.

I would like to recognise all my fellow students that helped me over the years with experiments, analysis and contributing to making my time at the University of Wollongong enjoyable and memorable. Particularly Sarah Alnaghy, Meagan Gargett, Saree Alnaghy, Thahabah Alharthi and Natalia Roberts for all the help with experiments and also your friendship. Thank you to my friends Lachlan Chartier, Mitchell Duncan, Anthony Espinoza and Matthew Newall.

To my family, thank you for a lifetime of love and encouragement, I would not be who I am today without all of you.

This research was supported by an Australian Government Research Training Program Scholarship and the South Western Sydney Local Health District Radiation Oncology Student Scholarship.

Finally a special thanks to my partner and best friend Lauren who is always there for me with endless love and support.

Contents

List of Figures

List of Tables

Chapter 1

Introduction

Globally cancer is the second leading cause of death, and is estimated to be responsible for 9.6 million deaths in 2018 [1]. This is approximatly one in six of all deaths globally. By the age of 85 an Australian has a one in two chance of being diagnosed with cancer [2]. The Collaboration for Cancer Outcomes Research and Evaluation (CCORE) estimated for the Australian population 48.3% of cancer cases would benefit from utilising radiation therapy as part of the course of treatment [3]. External Beam Radiation Therapy (EBRT) is the most common type of radiotherapy in Australia. EBRT is a non-invasive treatment that typically uses x-ray or electron beams to irreparably damage cancer cells. Other particles such as protons and carbon ions are also sometimes used for EBRT. Due to high capital cost they are not used in Australia at this point in time, although an Australian first proton beam is currently under construction [4]. For x-ray and electron EBRT, a linear accelerator generates the radiation beams and either statically or dynamically uses a combination of beam direction and shapes that has been optimised for the patients disease and anatomy (called the patients treatment plan) to deliver the required dose of radiation to the tumour volume and minimise normal tissue damage.

The patient's treatment plan is generated based on a computed tomography (CT) scan of the patient in the treatment position and external landmarks (typically tattoo dots) are placed on the patient's skin to aid with positioning on treatment. The external landmarks are a surrogate for the internal anatomy being targeted with the spatial relationship between the external markers and the internal target assumed to be static if they are to be relied on for daily positioning of the patient. Many internal sites are mobile relative to the patient's external anatomy, for example prostate position can vary with bladder and bowel filling/emptying or a patient may experience weight loss during the course of treatment resulting in a change in location of the treatment site relative to the external markers. To address this issue various forms of imaging have been integrated with the linear accelerators used for treatment to provide internal anatomical information immediately prior to or during treatment, this is called image guided radiotherapy (IGRT). The most common form of imaging used is kilovoltage (kV) imaging, either planar x-ray imaging or kV cone beam CT (kV-CBCT). The positional information acquired from the imaging is used in combination with a robotic couch to correct small daily setup variations. One of the limitations of kV imaging is the soft tissue contrast being too low in some cases to differentiate the target from surrounding tissue. Boney anatomy is used as an internal surrogate for the treatment target in these cases. A novel form of IGRT is the combination of Magnetic Resonance Imaging (MRI) with a linear accelerator into a hybrid treatment system called an MRI-linac. MRI provides superior soft tissue contrast relative to kV imaging and often allows direct visualisation of the treatment target and surrounding internal anatomy.

MRI scanners require a strong magnetic field typically in the order of 0.35 tesla (T) to 3 T. All current technologies employed to generate the main static magnetic field component cannot ramp the magnetic field up/down in a time frame that is feasible to turn off the magnetic field for treatment. The MRI-linac systems require the patient to be treated in the presence of a strong magnetic field and this presents unique dosimetry challenges. The dose deposited in the patient during radiotherapy is from the interaction of charged particles. The charged particles may be the primary beam particle such as with electron or proton beams or may be generated as secondary electrons from interactions between the primary x-ray beam and the patient's tissue. Charged particles travelling in a magnetic field experience a force known as the Lorentz force that alters their trajectory. This in turn can alter the spatial distribution of where dose is deposited relative to the case where there is no strong magnetic field. The magnetic field also impacts the functionality of radiation detectors that are relied upon to characterise and monitor radiation beam characteristics and confirm the dosimetry of patient treatment plans.

This thesis will focus on the application of monolithic silicon array dosimeters for beam quality assurance for MRI guided radiotherapy systems. The monolithic silicon array dosimeters have been designed at the Centre for Medical Radiation Physics (CMRP, University of Wollongong, Australia). To quantify effects on the dosimeter introduced by a magnetic field, it is desirable to perform measurements with and without magnetic fields, as well as at multiple magnetic field strengths. As this was not feasible on the current hybrid MRI guided radiotherapy systems, this was addressed through the design and subsequent fabrication of a semi-portable magnetic system that will allow the experimental characterisation of magnetic field effects on dosimeters using a standard clinical linear accelerator. The semi-portable magnetic system was used to characterise the monolithic silicon array dosimeters prior to implementing radiotherapy beam quality assurance measurements utilising the dosimeters. The quality assurance measurements investigated include proton beam profile and Bragg peak measurements on a horizontal proton beamline in the presence of a magnetic field of comparable strength to MRI systems. The dosimeters were used to characterise the optical, MR imaging and radiation isocentre of the prototype Australian MRI-Linac system.

1.1 Aims and Objectives

The aims of this thesis were to:

1. Determine a method to experimentally investigate the effect of a magnetic field on the response of dosimetry systems for varying magnetic field strength and orientations relative to the incident radiation beam direction.
2. Experimentally characterise the radiation detector properties, including the effects of a strong magnetic field on a monolithic silicon array dosimeter proposed for use in quality assurance of radiation beam properties of MRI-guided radiotherapy systems.
3. Use a monolithic silicon array dosimeter to measure therapeutic quality proton beams in a magnetic field environment that is an early prototype for future real-time MRI-guided proton therapy systems.
4. Design a quality assurance device utilising the high spatial resolution of monolithic silicon array detectors to characterise the spatial relationship of the optical, MR imaging and radiation isocentre of MRI-linac systems.

1.2 Contributions and Publications

First Author Publications:

- **Causer, T.**, Metcalfe, P., Rosenfeld, A., Oborn, B.M., “A portable magnet for radiation biology and dosimetry studies in magnetic fields” *Medical Physics*, vol. 49, pp 1924-1931, 2022.
- **Causer, T.**, Schellhammer, S., Gantz, S., Lühr, A., Hoffmann, A,. Metcalfe, P., Rosenfeld, A., Guatelli, S., Petasecca, M., Oborn, B.M., “First application of a high resolution silicon detector for proton beam Bragg peak detection in a 0.95 T magnetic field” *Medical Physics*, vol. 47, pp 181-189, 2020.
- **Causer, T.**, Chapman, T. Oborn, B.M., Davis, J., Petasecca, M., Rosenfeld, A., Metcalfe, P., “Characterization of a high spatiotemporal resolution

monolithic silicon strip detector for MRI-linac dosimetry" *Journal of Physics: Conference Series*, no. 1154 012006, 2019.

- **Causer, T.**, Alnaghy, SJ., Alnaghy, S., Roberts, N., Petasecca, M., Rosenfeld, A., Metcalfe, P., Oborn, B.M., "Imaging and radiation isocentre determination for inline MR-guided radiotherapy systems- proof of principle using MR-phantom with embedded monolithic silicon detector" *Journal of Physics: Conference Series*, no. 1662 012008, 2020.

Co-Author Publications:

- Kueng, R., Oborn, B.M., Roberts, N.F, **Causer, T.**, Stampanoni, M.F.M., Manser, P., Keall, P.J., Fix, M.K., "Towards MR-guided electron therapy: Measurement and simulation of clinical electron beams in magnetic fields." *Physica Medica*, vol. 78, pp 83-92, 2020.

- Alnaghy, S., **Causer, T.**, Roberts, N., Oborn, B.M., Jelen, U., Dong, B., Gargett, M., Begg, J., Liney, G., Petasecca, M., Rosenfeld, A., Holloway, L., Metcalfe, P., "High Resolution Silicon Array Detector Implementation in an Inline MRI-Linac." *Medical Physics*, vol. 47(4), pp 1920-1929, 2020.

- Alnaghy, S., **Causer, T.**, Gargett, M., Roberts, N., Petasecca, M., Oborn, B.M., Rosenfeld, A., Holloway, L., Metcalfe, P., "A Feasibility Study for High Resolution Silicon Array Detector Performance in the Magnetic Field of a Permanent Magnet System." *Medical Physics*, vol. 46(9), pp 4224-4232. 2019.

- Roberts, N., Patterson, E., Jelen, U., **Causer, T.**, Holloway, L., Liney, G., Lerch, M., Rosenfeld, A., Cutajar, D., Oborn, B.M., Metcalfe, P., "Experimental characterization of magnetically focused electron contamination at the surface of a high-field inline MRI-linac." *Medical Physics*. vol. 46(12) , pp 5780-5789, 2019.

- Begg, J., Alnaghy, S., **Causer, T.**, Alharthi, T., George, A., Glaubes, L., Dong, B., Goozee, G., Keall, P., Jelen, U., Liney, G., Holloway, L., "Technical Note: Experimental characterization of the dose deposition in parallel MRI-linacs at various magnetic field strengths." *Medical Physics*, vol. 46(11), pp 5152-5158, 2019.

- Roberts, N., Oborn, B.M., Jelen, U., Dong, B., Begg, J., George, A., Alnaghy, S., **Causer, T.**, Alharthi, T., Holloway, L., Metcalfe, P., "Modelling the x-ray source for the Australian MRI-Linac." *Journal of Physics: Conference Series*. no. 1154 012025, 2019.

- Gargett, M., Oborn, B., Alnaghy, S., **Causer, T.**, Petasecca, M., Rosenfeld, A., Metcalfe, P., "A high resolution 2D array detector system for small-field

MRI-LINAC applications." *Biomedical Physics & Engineering Express.*, vol. 4, no. 3, 2018.

- Alnaghy, S., Begg, J., **Causer, T.**, Alharthi, T., Glaubes, L., Dong, B., George, A., Holloway, L., Metcalfe, P., "Technical Note: Penumbral Width Trimming in Solid Lung Dose Profiles for 0.9 T and 1.5 T MRI-Linac Prototypes." *Medical Physics*, vol. 45(1), pp 479-487, 2017.
- Oborn, B.M., Gargett, M., **Causer, T.**, Alnaghy, S., Hardcastle, N., Metcalfe, P., Keall, P., "Experimental verification of dose enhancement effects in a lung phantom from inline magnetic fields." *Radiotherapy and Oncology.* vol. 125, no. 3, pp.433-438, 2017.
- Begg, J., George, A., Alnaghy, S., **Causer, T.**, Alharthi, T., Glaubes, L., Dong, B., Goozee, G., Liney, G., Holloway, L., Keall, P., "The Australian MRI-Linac Program: measuring profiles and PDD in a horizontal beam." *Journal of Physics: Conference Series.*, no. 777 012035, 2017.
- Liney, G.P., Dong, B., Begg, J., Vial, P., Zhang, K., Lee, F., Walker, A., Rai, R., **Causer, T.**, Alnaghy, S., Oborn, B.M., Holloway, L., Metcalfe, P., Barton, M., Crozier, S., Keall, P., "Technical Note: Experimental results from a prototype high-field inline MRI-linac." *Medical Physics.*, vol. 43(9), pp 5188-5194, 2016.

Conference Presentations:

- **Causer, T.**, Alnaghy, S.J., Alnaghy, S., Roberts, N., Metcalfe, P., Rosenfeld, A., Guatelli, S., Petasecca, M., Oborn, B.M., "Imaging and Radiation isocentre determination for inline MR-guided radiotherapy systems - proof of principle using monolithic silicon detectror " *MMND-ITRO*, Australia, Febuary 2020.
- **Causer, T.**, Alnaghy, S.J. , Roberts N., Jelen, U., Dong, Rosenfeld, A.B., Guatelli, S., Petasecca, M., Metcalfe, P., Oborn, B.M., "Towards real-time high resolution dosimetry in an MRI-Linac: proof of concept" *7th MR in RT Symposium*, Canada, June 2019.
- **Causer, T.**, Oborn, B.M., Schellhammer, S., Gantz, S., Lühr, A., Hoffmann, A., Petasecca, M., Guatelli, S., Metcalfe, P., Rosenfeld, A., "High resolution silicon detector performance measuring proton pencil beam profiles" *EPSM*, Australia, November 2017
- **Causer, T.**, Chapman, T. Oborn, B.M., Davis, J., Petasecca, M., Rosenfeld, A., Metcalfe, P., "Characterisation of monolithic silicon strip detectors for MRI-Linac dosimetry" *MMND-ITRO*, Australia, Febuary 2017
- **Causer, T.**, B Oborn, M Gargett, A B Rosenfeld and P Metcalfe, "Exper-

imental verification of the magnetic field of a new apparatus for performing experiments in MRI-Linac dosimetry” *EPSM*, Australia, November 2016

Chapter 2

Literature review

This chapter will provide a review of the role of magnetic resonance imaging (MRI) in Image Guided Radiation Therapy and the steps taken to achieve the current clinical systems that have intergrated magnetic resonance imaging with radiation therapy delivery. A summary of current MRI-linac facilities is presented along with a look at the current literature related to MRI-proton therapy. The dosimetric challenges associated with the use of current commercial radiation detection systems in magnetic field environments is reviewed along with the detector systems developed at the CMRP used in this thesis.

2.1 Image Guided Radiation Therapy (IGRT)

Image-guided radiotherapy (IGRT) is a technique where images of the patient's treatment site and its surrounding anatomy are taken when the patient is positioned ready for treatment on the device they will be treated with, such as a radiotherapy linear accelerator (linac). The process may take place immediately prior and/or during radiation therapy treatments. Most modern linacs are equipped with patient imaging systems. The most common image guidance techniques for linac based EBRT use on-board Kilovoltage (kV) and Megavoltage (MV) electronic portal imaging device (EPID) systems. A flat panel imager mounted to the linac on the opposite side of the patient to the treatment head is used to take MV transmission images [5, 6]. Imaging with the MV treatment beam produces images with a lower soft tissue contrast than the on-board kV imaging system, however the treatment field information such as field edges relative to the patients bony anatomy may be directly visualised on the MV images. Both the kV and MV beams may be used for on board Cone-Beam Computed Tomography (CBCT) providing volumetric information at a cost of extra delivered imaging dose relative to the planar alternatives [7]. Other less common modalities used for set-up correction that do not use ionizing radiation include ultrasound imaging, implanted electromagnetic (EM) transponders and surface guidance systems.

The ideal imaging technology for image guided radiotherapy should provide 4D realtime volumetric imaging of the treatment target and surrounding anatomy, efficient comparison of the 3D volumetrics, and a process for clinically meaningful intervention. The goal of using IGRT is to decrease the uncertainty in radiotherapy treatment delivery and as a result improve patient outcomes. The technology closest to meeting the requirements for image guided radiotherapy in soft tissue and mobile cancer sites is MRI-guided radiation therapy (MRIgRT) systems. The advantages of MRIgRT systems as an IGRT system are the superior soft tissue contrast available in real time that allows direct monitoring of the target and organs at risk (rather than a surrogate structure or marker).

There is significant current research into using MRI imaging to infer functional information about tumour response that may eventually be used to adapt the treatment [8–10]. Apart from the technical engineering challenges of combining an MRI scanner with a radiotherapy delivery source there are also limitations to MRI imaging. Decreasing the acquisition times for real-time imaging in MRI requires a trade-off in acquisition volume and resolution, MRI imaging acquisition artefacts caused by patient internal motion and significant financial cost relative to kV based systems.

2.2 MRI-Linacs

The idea of a hybrid MRI-linac was first proposed by Lagendijk and Bakker in 1999 [11]. The vision presented was for a hybrid machine where the MRI and linear accelerator function independently but simultaneously using the same isocentre.

The first demonstrated approaches of integrating an MRI with an external beam radiotherapy delivery system was the integrated environment reported by Karlsson et al in 2009, an MRI scanner was installed close to the treatment linac and a trolley was developed for transporting patients who were fixated in their treatment position between the MR unit and the accelerator for the radiotherapy [12]. Another approach to integrating an MRI into the radiotherapy delivery workflow for patient positioning using soft tissue was demonstrated by Jaffray et al at the Princess Margret Cancer Care Centre [13]. The system employs rails to move the MRI into the radiotherapy suite 3.1 m away from the linac isocentre and the patient to this location. The pre-treatment image verification (MR-MR registration) is performed and the rail system is used to move the patient back to the treatment isocentre and the

(a) (b)

Figure 2.1: (a) Visualisation of ViewRay MRIdian Linac (ViewRay Inc., Oakwood, USA), reproduced with permission. Image courtesy of ViewRay. (b) Visualisation of Unity MR-Linac (Elekta AB, Stockholm, Sweden), reproduced with permission. Image courtesy of Elekta.

MRI is retracted from the treatment suite. Both of these systems rely on non-MR guided technologies for feedback during radiotherapy delivery.

There are multiple groups working on hybrid MRI-guided radiation therapy (MRI-gRT) systems where the radiation isocentre and the MR imaging isocentre are coincident. The MRIdian system developed by ViewRay (ViewRay, Ohio, United States of America) was the first to treat patients, starting January 2014 [14]. The system combined three Cobalt-60 (^{60}Co) teletherapy heads, each head has its own multi leaf collimator (MLC), with a split-magnet 0.35 T MRI which has a 50 cm field of view with a 70 cm diameter bore. ViewRay has more recently developed an MRI-Linac system called the MRIdian Linac shown in Fig 2.1(a). This system has been designed as an upgrade to existing MRIdian systems, replacing the three cobalt sources with a single 6 MV standing wave linac. The first patients were treated with the MRIdian Linac in July 2017 [15].

The proof of concept prototype system developed at University Medical Center (UMC) Utrecht in collaboration with Elekta (Elekta AB, Stockholm, Sweden) and Philips (Philips Medical Systems, Best, The Netherlands) integrated a 6 MV Elekta linac and 1.5 T Philips Achieva MRI and demonstrated simultaneous image and irradiation of a phantom [16]. This system was iteratively developed into a clinical prototype, called ‘Unity’ that started patient treatments in 2017 [17]. The Unity system shown in Fig 2.1(b) uses a 1.5 T MRI system with a ring-type gantry and a 7 MV standing wave linear accelerator. The beam is collimated with a non-rotational 160 leaf MLC with 7.1 mm wide leaves at the isocenter plane. The MRIdian and Unity systems both have the radiation beam orientated perpendicularly to the static magnetic field (B_0) direction of the MRI scanner. Other systems under development have chosen to orientate the radiation beam parallel to the B_0 field direction. This

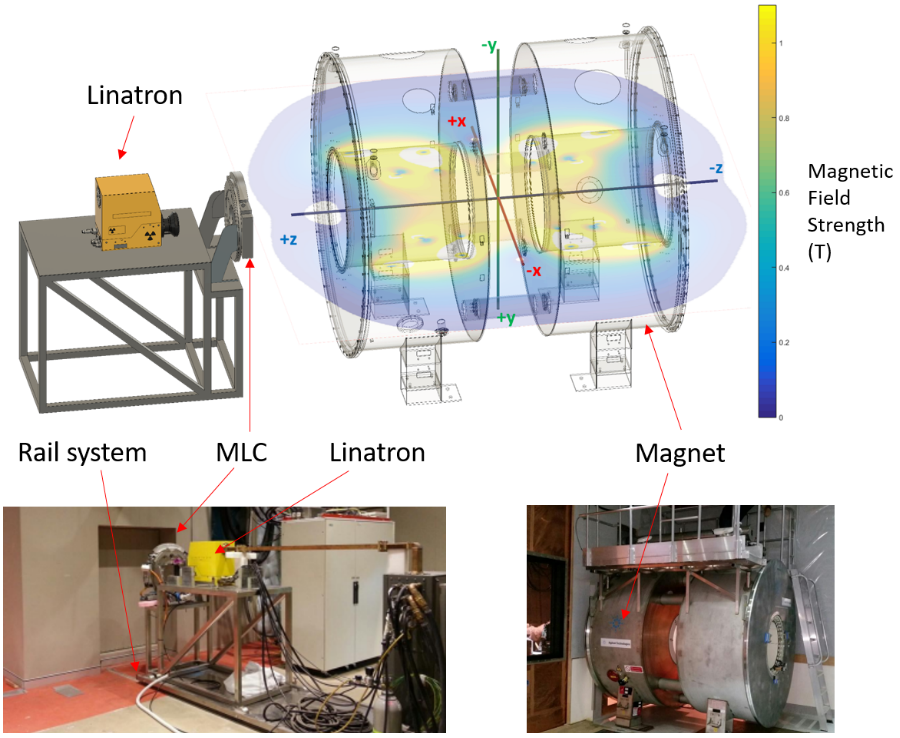

Figure 2.2: Visualisation of Australian MRI Linac showing the magnetic field strength and coordinate system originating at the systems isocentre with photograps of key components.

design choice has been implemented by the group at Cross Cancer Institute. Their system combines a 6 MV linac mounted on the open end of a biplanar MRI magnet, with both the linac and magnet mounted on a gantry that rotates around the patient, they have called this the 'rotating-biplanar' (RBP) geometry. The group's first prototype was a miniature system with a 0.2 T magnet commercially available from MRI Tech Co with a pole-to-pole gap of 27.9 cm [18]. An updated functioning whole-body version has been developed with a 0.6 T MRI and a 60 cm pole gap [19]. The first prototype Australian MRI-Linac combined a 1.5 T Siemens Sonata MRI with a Varian Linatron 6/4 MV linac, beam collimation is provided by a clinical 120 leaf MLC (Millennium, Varian). The linac position is adjustable such that the source to isocentre distance can be varied from 1.8 m - 3.2 m, and the beam is orientated parallel to the MRI B_0 [20]. The prototype was updated with a bespoke replacement 1 T split-bore magnet (Agilent Technologies). In the current setup of the Austrtalian MRI-Linac shown in Fig 2.2 the beam is inline with the B_0 field and the treatment table is positioned perpendicular to the beam. Real-time imaging during beam on to monitor breathing and perform gating has been demonstrated for animal treatments on this system [21].

2.3 Radiation Dosimetry in MRIgRT

In the MV energy range used by radiotherapy linear accelerators the primary photons predominantly interact via Compton scattering resulting in the liberation of the secondary electrons. The trajectory of the secondary electrons are influenced by the MRI's magnetic field. Magnetic fields exert a magnetic force on moving charged particles, known as the Lorentz force. The Lorentz force is orthogonal to the particles velocity altering the particles trajectory. When a particle (in a vacuum) with charge q, mass m and velocity ($\vec{v}$) enters a uniform magnetic field ($\vec{B}$) perpendicularly oriented to the particles velocity the Lorentz force directs it into a circular trajectory with gyration radius r. For the case when the velocity has a component parallel to the magnetic field then the charged particles traverse a helical trajectory.

$$\vec{F_B} = q\vec{v} \times \vec{B} \tag{2.1}$$

$$r = \frac{mv}{qB} \tag{2.2}$$

When considering the case of radiotherapy the secondary electrons are travelling in either air or tissue and hence their path is also strongly governed by Coulomb interactions with the material being traversed. The result being the electrons travel in a series of arc-shaped trajectories between interactions, where each interaction changes the direction of the electron.

To understand the bulk perturbations of dose distributions caused by the MRI's magnetic field it is intuitive to first consider a simplified case of a pointspread kernel (PSK). A pointspread kernel is defined as the energy deposition (or dose) distribution emanating from a point irradiation, in an infinite medium. Energy transport by all possible secondary particles is considered. For the case of a typical 6 MV linac beam incident on water, Compton scattering is the dominating interaction for the production of secondary electrons. Since these electrons will have a short range the kernel will drop off rapidly around the interaction site [22]. The distance the secondary particles travel before interacting again is related to the density of the materials and hence the size of the PSK. This effect is observed by comparing the relative size of the $B_0 = 0$ T PSKs in lung and water shown in Fig 2.3. For the case where the magnetic field is perpendicular to primary photon direction, the result is an asymmetric kernel, less depth penetration and a smaller surface area of the volume of equal enclosed isodoses as field strength increases [23]. For the case where the magnetic field is parallel to primary photon direction the effect of the magnetic

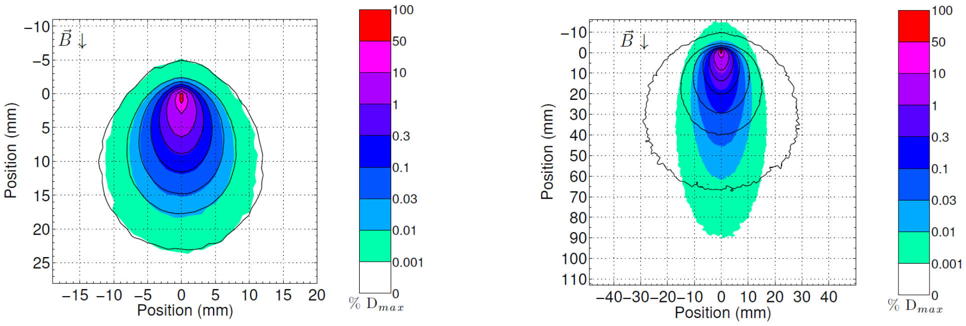

$B_{\|} = 1T$, water.

(a)

$B_{\|} = 1T$, lung.

(b)

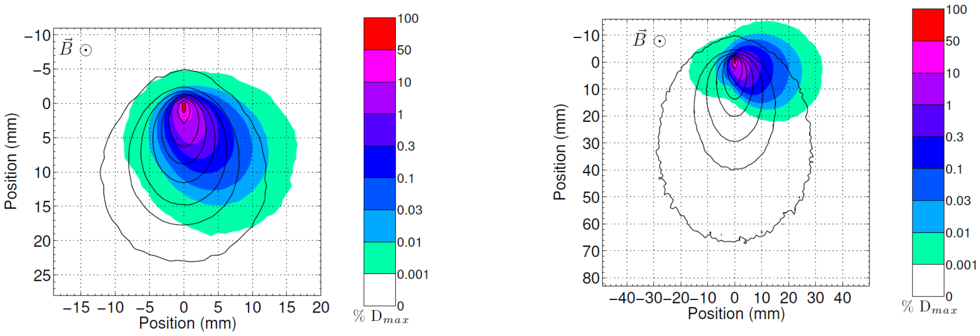

$B_{\perp} = 1T$, water.

(c)

$B_{\perp} = 1T$, lung.

(d)

Figure 2.3: Point spread dose arrays in water and lung for: (a) B parallel, 1T, water (b) B parallel, 1T, lung (c) B perpendicular, 1T, water(d) B perpendicular, 1T, lung. The black isodose lines show the case with no field applied. (From Gargett, M.A., *High Resolution Radiation Therapy Dosimetry in Magnetic Fields using Novel Silicon Array Dosimeters: A Pilot for MRI-linac Applications*, Doctor of Philosophy thesis, with permission)

field results in a narrower PSK stretched in the primary photon direction.

2.3.1 Perpendicular orientation

In 2004, Raaymakers et al published the first study investigating the effects of a 1.5 T perpendicularly oriented magnetic field on dose deposition for 6 MV photons [24]. The study used Monte Carlo simulations of pencil beam dose deposition kernels in water and experiments using film and a 1.1 T permanent magnet (bending magnet from an Elekta SL75/20 medical linear accelerator). The study showed a decrease of the build-up distance in the depth dose, a lateral shift of the beam profile perpendicular to the direction of the magnetic field, and an increase in the penumbra. For field sizes where lateral lateral electron equilibrium is not established at the field centre the penumbra is asymmetric in the direction perpendicular to the magnetic field.

The electron return effect (ERE) was first demonstrated by Raaijmakers et al in

2005 using both Monte Carlo simulation and experimental measurement [25]. Experimental demonstration is achieved by Kodak X-Omat V film measurement in a perspex–air–perspex phantom within a 0.8 T magnetic field produced by an electromagnet. The study reported exit dose increases of 40% relative to the case without magnetic field, and the effect also occurs in air cavities if the cavity is larger than the electron trajectory radius in air. Further experimental verification of transverse magnetic field effects on photon beam percentage depth doses (PDD) was presented by Raaijmakers et al in 2007 [26]. The study presented measurements of PDDs in a Polymethyl methacrylate (PMMA) phantom with a 4 cm air gap at the centre of the phantom inline with the beam direction. An electromagnet was used to provide a 0.6 T and 1.3 T transverse magnetic field, an Elekta SL linear accelerator was used for the radiation source and PDDs were measured using Gafchromic film. The study showed the previously reported reduced buildup distance from phantom surface to the depth of maximum dose and ERE at both the air gap and exit surface of the phantom. A Monte Carlo simulation of the experimental measurements was presented with analysis of the agreement between measurement and simulations. The authors concluded that Geant4 Monte Carlo simulations were suitable to investigate consequences of a magnetic field on the dose distribution for the MRI-accelerator. A follow up study from the group at Utrecht used the previously validated Monte Carlo model to investigate the effect of surface orientation on the entrance and exit surface dose changes due to the ERE [16]. The effects were modelled for magnetic field strengths B = 0 T and B = 1.5 T with phantom exit and entrance surface orientations (−75°, −60°, −45°, −30°, −15°, 0°, 15°, 30°, 45°, 60°, and 75°) relative to the plane perpendicular to the beam direction. The simulations showed the entrance and exit doses are almost linearly dependent on the angle formed between the incident beam and the phantom surface. The build-up distance ranges from 0 mm for 60° and 75° to 35 mm for −75°. The entrance dose is minimal for −30° and increases for large positive angles. The exit dose is maximal for −60° and decreases for increasing phantom exit surface angle.

Also in 2007 the group at Utrecht demonstrated the dosimetry changes for a perpendicular MRI-Linac including decreased build-up distance and a shifted, asymmetrical penumbra and the ERE, do not compromise the ability to achieve clinically acceptable dose distributions with IMRT for prostate cancer, oropharyngeal cancer and laryngeal cancer treatment sites [27]. Differences in the dose distribution between the $B_0 = 0$ and 1.5 T case were minimal, with only the skin dose increasing for $B_0 = 1.5$ T. Homogeneous dose distributions were obtained for target structures located adjacent to air cavities without the use of opposing beams. The relationship between magnetic field strength and ERE dose for MRI-Linacs in a perpendicular orientation was investigated by the group at Utrecht for field strengths of 0.2, 0.75, 1.5 and 3 T. The results published in 2008 showed that generally magnetic field dose effects decrease in magnitude for lower magnetic field strengths [23]. The study investigated ERE in cylindrical air cavities and in lung tissue as well as ERE at the exit side of the beam and beam extending over the lateral side of a phantom. The authors concluded the magnitude of the ERE reduces with decreasing magnetic field strength for lateral ERE, for small air cavities and and for tissue–lung interfaces. The authors also observed that for large irradiation fields the increase in ERE dose may reach equivalent levels as for the case of higher magnetic field strengths. Also in the case of large air cavities significant increase in dose is encountered for all magnetic field strengths investigated.

A Monte Carlo simulation study by the Alberta group was the first to compare the influence of a uniform magnetic field on clinically realistic radiotherapy dose distributions for both fixed cylindrical (FC) geometry and rotating biplanar geometry MRI linac configurations [28]. The study also looked at slab phantom simulations of single beams and parallel opposed beams for water/lung/water slab geometry and 0.2 T and 1.5 T, the authors demonstrated difference in dose profiles near water-lung interfaces and concluded the slab simulation results agreed with Raaijmakers et al [16]. Simulations of four-field box brain treatment showed with RBP setup and magnetic field strength of 0.2 T, radiation dose hotspots of +4% and cold spots of -2% when compared to $B_0 = 0$ T case and for FC with magnetic field strength of 1.5 T, differences in dose of up to +10% and -5%. The five-field lung plan for RBP with $B_0 = 0.2$ T showed hot and cold spots of ±12% in the plan and FC at 0.2 T showed differences of similar magnitude to the RBP case of ±12%. The simulations of FC with $B_0 = 1.5$T showed the largest variation to the plans with hot spots as high as +30% and cold spots as low as -15% near tissue-lung boundaries.

A study by Oborn et al in 2009 used Monte Carlo simulation (GEANT4) to investigate entrance (surface and skin (70 µm, ICRU definition [29])) and exit dose for a transverse field MRI-linac with 6 MV photon beam (Varian 2100C) of various field sizes ($5 \times 5\,\text{cm}^2$, 10 cm × 10 cm, 15 cm × 15 cm, and 20 cm × 20 cm) and various uniform transverse magnetic fields (0.2, 0.75, 1.5, and 3 T) [30]. The study used high resolution dose scoring geometry with 10 µm voxels, and observed the exit doses increased for all magnetic field strengths investigated, as a direct consequence of the ERE. The results of Oborn et al also showed that for large field sizes, lower magnetic field strengths lead to higher skin exit doses for the magnetic field strengths investigated. This agreed with the study by Raaijmakers et al where the beam central axis exit dose (0.25 mm depth) from 5 cm × 5 cm and 10 cm × 10 cm 6 MV beams was predicted to be the greatest for a 0.75 T transverse field and less for

1.5 T and 3 T [23]. The explanation presented by Raaijmakers et al on why these intermediate magnetic fields have a higher exit skin dose relative to the higher magnetic field strengths investigated is the higher magnetic fields increasingly reduce the electron fluence exiting the phantom. Further work investigating surface doseimetry in MRI-guided radiotherapy using Monte Carlo simulation was published by Oborn et al in 2010 [31]. The study investigated the effect on surface and skin dose (beam entry and exit) due to surface orientation relative to the beam for a range of surface orientations ($-75°$, $-60°$, $-45°$, $-30°$, $-15°$, 0°, 15°, 30°, 45°, 60°, and 75°) and for a wider range of radiation field sizes (5 cm × 5 cm, 10 cm × 10 cm, 15 cm × 15 cm, and 20 cm × 20 cm) and magnetic field strengths (0, 0.2, 0.4, 0.6, 0.8, 1, 1.2, 1.4, 1.6, 1.8, 2, and 3 T). Entrance skin dose varied with the entry surface angle. The dose increases if the combination of surface angle and magnetic field effectively reduces the path length required for the electrons to reach the skin. The converse was also observed, and for the case where the surface was angled 30° to 60° and the charged particles travel in an anticlockwise direction, the entrance skin dose was comparable to or less than the zero magnetic field skin dose, regardless of magnetic field strength and field size. The study also investigated the possibility of using exit bolus of 1 cm thickness to reduce the dose delivered to the skin. It was shown that under 1 cm bolus exit skin dose is a more consistent value regardless of magnetic field strength or exit surface angle due to the almost complete absorption of the ERE electrons.

2.3.2 Inline orientation

Prior to the first publications exploring the idea of combining an MRI with a particle accelerator there were studies investigating the effect of an inline magnetic field on dose deposition of radiotherapy photon and electron beams in the literature [32]. A historical study by Bielaiew in 1993 presented a Monte Carlo investigation using EGS4 modified to account for the presence of a magnetic field, the authors investigated the central axis PDD characteristics of a 20 MeV electron beams in water for 0, 3 and 20 T magnetic fields inline with the radiation beam and concluded that the central axis depth dose curve in broad parallel beams should be independent of longitudinal field strength [32, 33]. In the same study the authors described the sharpening of a 20 MeV electron beams penumbra for 3 and 20 T fields. This effect was also shown for a monoenergetic 6 MeV photon beam. Ramahi et al used EGS4 Monte Carlo code to investigate the effect of 0.5 T longitudinal magnetic field relative to a 6 MV photon beam on dose deposition in a water phantom with air cavities 2, 4 and 6 cm long in the direction parallel to the beam [34]. The authors reported on a sharper penumbra in the air cavities. An experimental investigation by Litzenberg et al of dose deposition effects due to a longitudinal field on both electron and photon beams using a high-energy gantry of a two-gantry racetrack microtron accelerator (MM50 Scanditronix, Uppsala, Sweden) and a superconducting solenoidal magnet (Intermagnetics General Corporation, Guilderland, New York), with a 20 cm diameter bore, was used to produce a longitudinal magnetic field with a maximum strength of 3 T near the centre of the magnet [35]. The group reported a focusing effect of a 20 MeV electron beam measured using XV film (Kodak, Ready Pack) in a PMMA phantom. The beam profile was narrower with the inline magnetic field due to the gradient of the magnetic field mostly in the region corresponding to the magnetic centre. With the same setup using a 10 MV photon beam the group did not observe any effects on penumbra when measuring in PMMA. Higher surface dose was observed due to contaminant electrons that are collected and focused near the surface of the phantom.

The Alberta group compared the influence of an inline uniform magnetic field on clinically realistic radiotherapy dose distributions using Monte Carlo simulation for dose calculation for five-field lung plan across a range of magnetic field strengths from 0.2 T through 3.0 T [36]. The group concluded that the longitudinal configuration of MRI linac exhibits a decrease in tissue interface effects relative to transverse configurations and for lung tumour radiotherapy an increase in the dose to the PTV as a function of increased magnetic field due to the focusing of the secondary electrons in the forward direction.

The impact of inline magnetic fields on skin dose due to magnetic focusing of contamination electrons is a possible area of concern for inline MRI-linac designs. The orientation of the magnetic field causes electrons generated from interactions with the beam collimation and air above the patient to all be directed towards the patient surface. Oborn et al has investigated the magnitude of secondary electron focusing due to the effect of field strength from 0 to 3 T for field sizes of $5\,\mathrm{cm} \times 5\,\mathrm{cm}$, $10\,\mathrm{cm} \times 10\,\mathrm{cm}$, $15\,\mathrm{cm} \times 15\,\mathrm{cm}$, and $20\,\mathrm{cm} \times 20\,\mathrm{cm}$ for a 6 MV beam at surface and $70\,\mu\mathrm{m}$ [37]. The study also modelled the MRI fringe field using 1D form for the magnetic field. It was reported in the study that the skin dose increases with field size as the surface area of beam collimation increased. The fringe field and source to isocentre distance also effect the skin dose, increases of up to 1000 % d_{max} were reported for the worst case scenario investigated in the study. The group at Alberta presented a similar study investigating the skin dose increase for both transverse and inline magnetic field MRI linac configurations, the group used finite element modelling to produce a 3D model of the MRI fringe field for use in the Monte Carlo Simulations [38]. The group reported less than 15% increase (relative to d_{max}) in skin dose for all 6 MV beam scenarios investigated. They described their results as contrary to those of Oborn et al and hypothesized the lower skin doses observed is due to their use of a 3D model of the fringe field. The group later presented a simlar study for version 2 of their groups prototype MRI-Linac, reporting skin dose increases of less than 11% for the case of a 6 MV Varian source and less than 7% for a novel 10 MV linac source [39]. The publication has since been retracted at the request of the authors after they identified an incorrect coordinate transform had been applied between the magnetic field modelling software and the Monte Carlo radiation transport simulation package in the work [40].

2.4 MRI Guided Proton Therapy

The earliest literature on the concept of using an MRI combined with particle therapy is a patent awarded in 2004 (Bucholz and Miller 2004). The patent covers the medical treatment devices where a proton beam treats a patient in an MRI scanner and the function of the MRI is described for real-time guidance. An early study by Raaymakers et al investigated the fundamental beam transport and changes in dosimetry for a 90 MeV proton beam incident on a uniform water phantom and separatly a water phantom with an air gap in a 0.5 T magnetic field orientated perpendicularly to the beam direction [41]. The study concluded that a 0.5 T magnetic field would have minimal impact on the dose distribution for all clinically-used proton pencil beam energies. The authors also noted beam transport as a challenge due to the deflection of proton beams by the magnetic fringe field outside the MRI scanner. There have since been multiple studies investigating the challenge of the proton beam deflection due to a magnetic field. Wolf and Bortfield reported on an analytical calculation of the lateral deflection of protons with energies ranging from 50 MeV to 250 MeV, with the beam direction orientated perpendicular to the magnetic field [42]. The authors noted significant deflections (of the order of 1 cm) even at 0.5 T fields with energies around 200 MeV, as well as a small but significant range reduction. In a study by Oborn et al using magnetic modelling of a realistic 1 T split bore MRI and Monte Carlo simulation, the delivery of proton beams to the imaging region of the MRI from both from an inline and perpendicular orientation was reported [43]. The study highlighted the effects of the MRI fringe field used in the magnetic model for both investigated proton beam/MRI orientations. In the inline orientation of magnetic field and proton beam, the beam will exhibit significant rotation around the beam central axis (CAX). The beam will also experience a small degree of focussing toward the CAX. In the perpendicular orientation, there are both significant deflections and distortions.

A comparison of published analytical models describing a proton beams deflection and retraction when incident on a water phantom in a magnetic field was presented by Schellhammer and Hoffmann [44]. The authors presented their own analytical model compared it to the models of Hartman et al (2015) and Wolf and Bortfield (2012), using Monte Carlo calculations as the reference data [45]. For all the analytical models, the differences relative to the Monte Carlo results increase with increasing proton energy and magnetic flux density.

Dose deformation within the Bragg peak of proton beam in the presence of a magnetic field were reported on in a Monte Carlo study (Geant4) by Fuchs el at [46]. This study investigated proton beam energies of 60 to 250 MeV in magnetic fields ranging from 0 to 3 T. Beam deflection (and retraction) as well as dose deformation within the Bragg peak and the impact of material heterogeneities were investigated. Gamma-index (2 %/2 mm of the local maximum) was used to assess Bragg peak changes due the magnetic field, with the distortion of the dose distribution in the Bragg peak found to increase for increasing B-field strength. An increase in dose at water air interface due to ERE was reported in a water phantom with 30 mm air cavity. The magnitude of the effect was observed to be less than for MV x-ray beams in an equivalent magnetic field.

There are several studies looking into the proton radiotherapy treatment planning in magnetic fields. Moteabbed et al used Monte Carlo dose calculation to investigate the effects of a uniform perpendicular 0.5 T and 1.5 T magnetic field on treatment plans for lung, liver, brain, skull-base and spine [47]. Dose volume histogram (DVH) analysis as well as equivalent uniform dose were compared for both the target and organs at risk with and without the two magnetic field strengths. The authors concluded that for magnetic field strength less than 0.5 T all plans analysed excluding prostate were acceptable based on a minimal impact to target coverage and a minimal increase to nearby organ doses. For a 1.5 T magnetic field the dose distortions were more pronounced, with all plans excluding spine requiring corrections to produce an acceptable plan. A framework for intensity modulated proton therapy (IMPT) in the presence of a transverse 1.5 T magnetic field was presented by Hartman et al [45]. The planning framework used Monte Carlo to simulate a large number of possible proton beamlets for three pre-selected gantry angles with just enough statistics to determine the location of the Bragg Peak. The beamlets whose Bragg peaks are determined to be within the target are simulated again with higher statistics. Inverse optimisation is then used used to determine the treatment plan. This planning framework was applied with and without 1.5 T magnetic field to two head and neck tumor datasets and one liver tumor dataset. Comparison of the plans revealed no major dosimetric impact of the magnetic field.

The robustness of pencil beam scanning proton therapy (PBS-PT) plans in a 1.5

T magnetic field has been investigated for prostate cancer patients by Kurz et al [48]. To assess the robustness against anatomical changes and positioning errors in an MRI-guided scenario, five prostate cancer patients with CT scans acquired on three consecutive days were used. PBS-PT plans were optimised with and without B-field. The authors concluded that for the investigated plans, robustness was substantially reduced for the B = 1.5 T case relative to B = 0 T, but could be improved considerably by inverting the magnetic field or by selection of gantry angles where the proton trajectories changes with and without magnetic field are minimized within the patient.

Padilla-Cabal et al demonstrated the adaption of a pencil beam algorithm (PBA) for MRI-guided proton therapy which accounted for the effects induced by a transverse external magnetic field [49]. The beam data for the pencil beam model was based on Monte Carlo simulation in a water phantom. The model was evaluated by analysis of energy deposition maps in homogeneous and heterogeneous slab geometries for proton energies of 80, 150, and 240 MeV in magnetic field regions of 0.5 T, 1.5 T, and 3 T. The authors regarded the agreement between PBA and Monte Carlo dose calculation as excellent for slab-like and lateral heterogeneous phantoms, with gamma index (2 %/2 mm of the global maximum) passing rates above 98 % and mean values between 0.1 and 0.2. The agreement decreased for high-energy protons and higher strength magnetic fields, though the results were still regarded as good enough to be considered for future application in clinical practice.

A “Future of Medical Physics” themed article focused on real-time MRI-guided proton therapy by Oborn et al in 2017 provided a thorough discussion of the software and hardware challenges faced before a clinical MRI guided Proton therapy beamline may be realised clinically, as well as potential treatment workflow [50].

The first published functional proof-of-concept system combining an MRI scanner with a horizontal research proton beamline [see Fig 2.4] has been reported by a research programme at OncoRay in Dresden (Germany) [51]. In keeping with the theme of first imaging a food of cultural significance to the country where the system was developed[a], the group published T1-weighted spin echo images of a mixed sausage without beam, with energised beamline magnets and during proton irradiation at 215 MeV.

---

[a] The group at Utrecht in their first published demonstration of simultanious MR Imaging and irradiation imaged a pork chop, the Australian group used a kangaroo steak for a similar demonstration [20, 52].

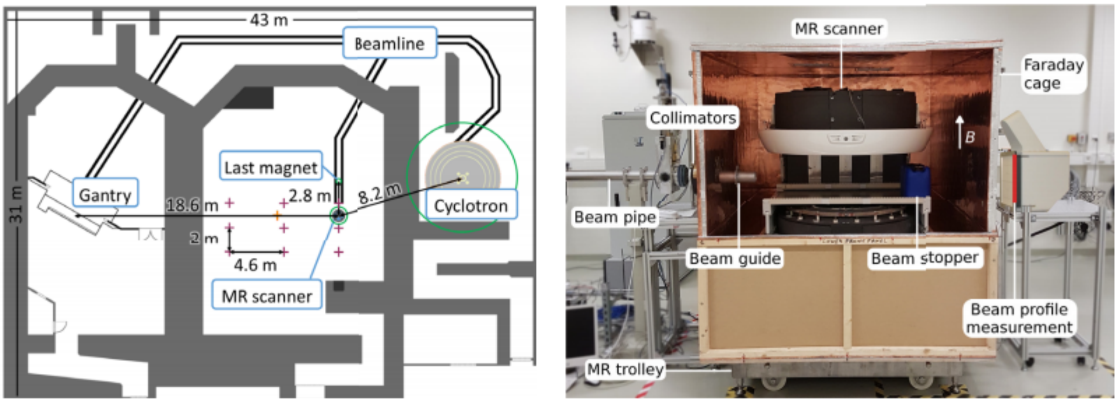

Figure 2.4: Left: Floor plan of the OncoRay Proton facility. Right: Experimantal setup of horizontal beamline with MR scanner, reprinted from [51] (Schellhammer, 2018). Reproduced with permission.

2.5 Magnetic field compatable detector technologies

As the interest in MRI-linacs has increased so to has the interest in magnetic field compatible radiation detectors. Suitable devices are required for the commissioning, routine quality assurance (QA) and patient specific QA for MRI-linacs. In hybrid MR guided radiotherapy devices, the permanent magnetic field influences secondary electrons by means of the Lorentz force effecting the dose distribution. The effects are dependent on the beam energy, magnetic field strength and the relative orientation of the radiation beam to the magnetic field, furthermore the response of radiation detectors may also be influenced by the presence of the magnetic field. The following sections will focus on published literature investigating the application of silicon diode detectors and Radiochromic film for performing radiation dosimetry in the presence of a magnetic field. Ionisation chambers are also an important dosimeter for radiation measurements in radiotherapy and are used for both absolute and relative dosimetry. With the presence of a magnetic field altering the trajectory of electrons in air, the path length traversed by electrons entering the cavity of an ionisation chamber will be effected differently depending on the orientation of the chamber with respect to the magnetic field [53]. This may result in either longer or shorter path lengths, generating more or less electron-ion pairs leading to a chamber response change due to the influence of the magnetic field [54–58].

2.5.1 Silicon diodes

Devices employing semiconductors as the radiation detection medium have been used since the 1960s [59]. Silicon has several characteristics that are advantageous

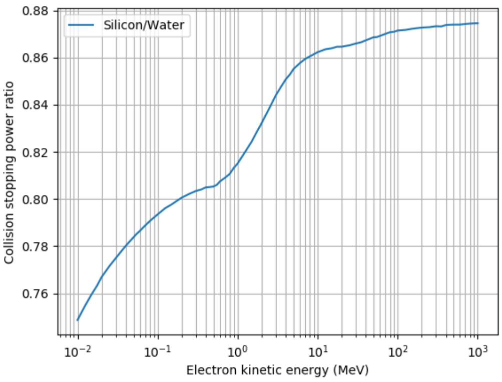

Figure 2.5: The mass collision stopping power ratio for silicon relative to water. Data from http://www.physics.nist.gov.

for its application as a radiation detector. The average energy required to create an electron-hole pair in silicon is 3.6 eV, which is an order of magnitude smaller than the ionisation energy of gases (approx 30 eV). The density of silicon (2.33 g/cm^3) is three orders of magnitude greater than that of a gas. Silicon detectors therefore have a potential radiation sensitivity approximately 18,000 times greater than an equivalent volume ionisation chamber, which allows for construction of small detectors or high resolution array detectors. Another property of silicon that is advantageous for radiation dosimetry in radiotherapy is the constancy of the mass collision stopping power ratio of silicon to water across the energy range used in external beam megavoltage radiotherapy shown in Figure 2.5. Silicon is also mechanically stable, requires no bias voltage to operate and can be operated at room temperature.

Semiconductor devices are created from the combination of p-type and n-type semiconductor materials. P-type and n-type semiconductors are created by intentionally adding a ‘dopant’ either group III or group V elements to a high purity semiconductor to tailor its properties, the process is called doping. A p-n junction is an interface between regions of p and n type doping within a single crystal of semiconductor. When the p-n junction is formed electrons from the n-region are free to diffuse across the junction and combine with holes in the p-region. Filling a hole produces a negative ion and leaves behind a positive ion on the n-side. A space charge builds up, creating what is called the depletion region, which prevents further electron transfer.

The interaction of ionizing radiation with a semiconductor excites electrons that transfer from the valence band to the conduction band of the crystal, leaving a hole in the valence band and resulting in an electron-hole pair (charge carriers). When this process occurs near a p-n junction the charge carriers may diffuse towards the

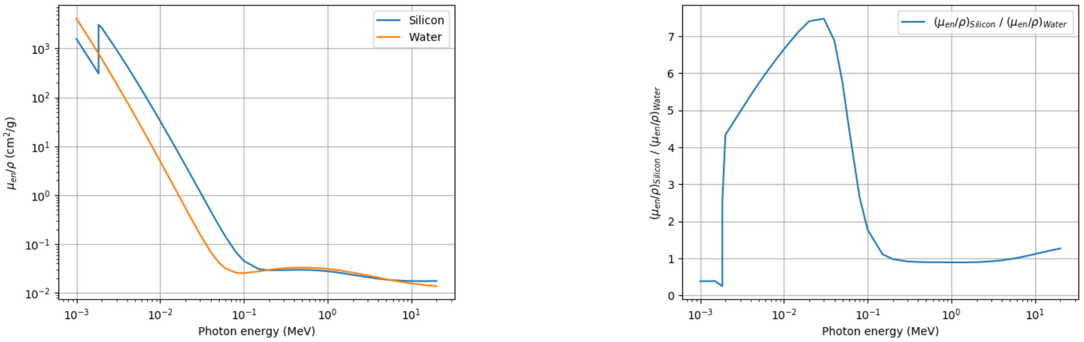

(a) **(b)**

Figure 2.6: Comparison of mass energy absorption coefficients for Water and Silicon. Data from http://www.physics.nist.gov.

depletion region where they are then swept across the junction due to the electric field. A current is generated in the reverse bias direction of the diode, which may be measured using an electrometer. The charge generated is linearly proportional to the energy deposited in the active region. An external bias may be applied to extend the depletion region resulting in an increased charge collection however this also increases leakage current and for this reason diode detectors are usually operated without external bias.

A characteristic of silicon detectors that is disadvantageous for use as a radiation detector is that the crystalline structure of the semiconductor material is damaged by the radiation. This radiation damage increases with dose and results in sensitivity loss, increased leakage and a temperature dependent sensitivity. The effect is reduced by pre-irradiation of the silicon so that a certain level of damage is introduced, but in practice semiconductor detectors may need to be recalibrated regularly and have a limited life-time. Dose measurements where low energy scattered radiation makes up a substantial contribution such as outside the primary beam, silicon diodse will exhibit a non-water equivalent energy response due to the difference in mass energy absorption coefficients for silicon and water below approximately 100 keV [see Fig. 2.6].

In a study by Reynolds et al the IBA PFD Diode Detector was characterised in-air for both inline and perpendicular magnetic fields relative to the zero field magnetic field case with PENELOPE Monte Carlo simulations and experimental measurements for the perpendicular magnetic orientation [60]. The group reported for an inline magnetic field of less than 1.5 T the response of the IBA PFD Diode varied by less than 1% due to the magnetic field, and for a perpendicular magnetic field the response of the diode was close to 20% at 1.5 T. The simulation and experimental measurements matched within 0.5%. The group also simulated the use of the IBA PFD Diode Detector in a water tank for beam scanning for both inline and perpendicular magnetic fields at 0.5 T. These simulations were not experimentally replicated as the electromagnet used for the in-air measurements was not large enough for use with a water phantom. It was reported that the IBA PFD Diode Detector did not accurately measure the shape of the penumbra for the transverse magnetic field case. In a follow up study, Reynolds et al presented experimental measurement of IBA PFD Diode Detector response for the case of an inline magnetic field relative to the radiation beam [61]. The authors reported no appreciable magnetic field dose response at strengths up to 0.21 T for the IBA PFD Diode Detector for an in-air geometry.

The use of a ArcCHECK (Sun Nuclear Corporation, Melbourne, USA) for patient specific QA in an MRgRT system was first reported by Li et al for use in a 0.35 T transverse magnetic field on a ViewRay MR-Cobalt system [62]. The performance of an MRI-compatible version of the Sun Nuclear ArcCHECK diode array (ArcCHECK-MR) was experimentally characterised by Houweling et al [63]. The ArcCHECK-MR is a cylindrical water-equivalent phantom with 1386 SunPoint® diodes arranged in a helical grid at 2.9 cm physical depth. Various inserts can be placed at the centre of the phantom. Houweling et al investigated the effect of a 1.5 T perpendicular magnetic field on the device performance by comparing the short term reproducibility, dose linearity, dose rate dependence, dose per pulse (DPP) dependence, field size dependence and the inter-diode dose response variation using an 1.5 T MR-linac (Unity prototype) and 0 T conventional Linac (Precise treatment system, Elekta). No significant difference was reported for short term reproducibility between 0 T and 1.5 T. The dose linearity was measured for 2 – 500 MU using same diode within the array both 0 T and 1.5 T, and was observed to be less than 0.5% above 10 MU. The dose rate dependence was measured by varying the MU/min delivered, however the two linacs do not have the same selectable dose rates so the authors were unable to use the exact same dose rates in the 0 T and 1.5 T comparison. Nevertheless the authors reported a similar trend and maximum deviation of 1% from nominal dose rate relative to the average of the investigated dose rates for both cases. The field sizes dependence (normalised to 10 cm × 10 cm) was reported to be comparable for both cases, as was the inter-diode dose response variation. The dose per pulse dependence was measured by varying the SSD of the setup on the conventional linac and correcting to a ionisation chamber measurement in solid water at equivalent distances, a 1% maximum deviation was recorded over the range investigated (79.2 to 132.9 cm SSD). However this method could not be reproduced on the MR-linac so a single ratio of two diodes at opposite sides on the array was reported by the authors for 0 T and 1.5 T of 2.7 and 2.9 respectively.

The authors concluded from the study that the ArcCHECK-MR is suitable for use in 1.5 T perpendicular and inline MRI linacs.

A similar study to that of Houweling et al was performed by De Varies, characterising a magnetic field compatible version of the Delta4 diode array detector system (Scandidos AB, Uppsala Sweden) [64]. The Delta4 is a cylindrical PMMA phantom containing 1069 p-type Si-diodes arranged on two orthogonal detector boards. The effect of a 1.5 T perpendicular magnetic field on device performance was assessed by comparing the short term reproducibility, dose linearity, dose rate dependence, field size dependence, angular dependence and DPP dependence using an 1.5 T MR-linac (Unity prototype) and 0 T conventional Linac (Precise treatment system, Elekta). The magnetic field compatible Detla4 was also compared to a non-magnetic field Delta4 on the conventional linac. The authors reported that for the majority of tests the two devices responded equivalently for all Delta4/linac combinations within statistical uncertainty including the dose linearity ($\leq$0.5%), short-term reproducibility (<0.1%), field size dependency (<2.0% for field sizes larger than 5 cm × 5 cm), dose rate dependency (<1.0%) and angular dependency. There was an observed difference in the two devices DPP dependency (<0.8%). The authors attributed this difference to higher total accumulated dose delivered to the diodes in the clinical Delta4-PT (6 years clinical use) compared to the diodes in the MR-Delta4-PT.

The authors also reported deflection of secondary electrons by the Lorentz force within a detector will influence the detectors response. For clinical photon-beam scanning of MRgRT units in a water tank, this effect may cause deviations of measured dose profiles. This effect was investigated both experimentally and using EGSnrc Monte-Carlo by Delfs et al for PTW Diode E 60017 by using a slit beam geometry to investigate 1D dose response in a 0.35 and 1.42 T magnetic field relative to the 0 T case [65]. The PTW Diode E 60017 was reported to have an asymmetric distortion of its lateral dose response in a transverse magnetic field, which will affect the measured signal profiles when used for photon beam scanning in a transverse magnetic field.

Silicon diodes also have a number of desirable properties for use as an in vivo dosimeter for radiotherapy treatments including short processing time, high sensitivity, high reproducibility, mechanical stability, small size and absence of external bias. Choi et al investigated the effect of a 0.35 T transverse magnetic fields on the response QE detectors (Sun Nuclear Corporation, Melbourne, FL, USA), a proprietary radiation-hardened silicon diode, specifically for in vivo dosimetry [66]. The QE detectors are available in three photon energy ranges, a single electron energy range, and a skin detector. The study used a ViewRay system to investigate the influence of 0.35 T magnetic field on two variations of QED detectors (skin QED and 1-4 MV QED), reporting on angular dependence, response variation with depth and detector measured output factors. The study reported the 1-4 MV QED was not affected by the B-field for all examined situations, however the skin QED displayed an angular dependence of up to 2.4 % different relative to 0 T. The response of the skin QED at surface was increased from 0.5 % to 4.3 % for field sizes between 4.2 cm^2 to 27 cm^2 in the presence of the magnetic field, however all depths investigated the response was equivalent to the response without the magnetic field.

Diode detectors are established in their use for relative dose distribution measurements including proton beam depth-doses and lateral beam profiles, and have also been used for absolute dose measurement in proton beams [67, 68]. Liengsawangwong et al. have performed absolute dose calibration of a commercial diode detector array for passively scattered proton beams. Grusell and Medin compared relative dose measurements of a proton beam with initial energy of 174 MeV using a highly doped p-type Si detector and a plane-parallel NACP ionization chamber. The study demonstrated the highly doped p-type Si detector gives a signal proportional to the ionization density in the detector of the measured proton beam [69]. The dosimetric properties of a Scanditronix stereotactic silicon diode (0.06 mm thick) and a PTW natural diamond detector (0.26 mm thick) in low-energy proton beams was investigated by Onori et al [70]. The study concluded that both detectors showed for varying dose rate and proton energy linearity at a therapeutic dose level and reproducibility within 1%. The investigated silicon diode underestimated the dose in the bragg peak of the 21.5 MeV proton beam while the diamond detectors physical size was too large for relative dose measurements of low-energy proton beams. The feasibility of using a monolithic silicon detector to measure clinical proton beam properties has been investigated by Bisello et al, and the same detector technology has been investigated for use in proton imaging [71, 72]. The feasibility of using a monolithic silicon strip detector for angle verification of proton beam has been shown by Merchant et a [73]. The same detector system used by Merchant et al has also been investigated for measuring small field proton beam profiles and depth dose profiles showing excellent agreement with EBT3 film measurements and Monte Carlo simulations [74]. Grant et al investigated the characteristics of the PTW PR60020 proton dosimetry diode using radiation fields and beam energies relevant to radiosurgery applications [75]. In the study depth dose and beam profile data were compared with PTW Markus N23343 ionization chamber, EBT2 Gafchromic film, and Monte Carlo simulations. The PTW PR60020 displayed a linear response with dose and dose rate, a small sensitivity decrease per unit dose of 0.01% per Gy was observed , a less than 1% difference in response was observed for axial/edge-on irradiation. The PTW PR60020 showed negligible LET dependence from entrance to the distal region of the SOBP for particle energies and ranges typical for clinical radiosurgery.

2.5.2 Radiochromic film

Radiochromic film is a high spatial resolution dosimeter with a relatively flat energy response, near tissue-equivalence and a dose sensitivity range that covers most external beam radiotherapy applications [76]. There are numerous models of radiochromic film. They contain an active layer of diacetylene dye monomers that when exposed to ionising radiation undergo polymerisation. The active layer is sandwiched between protective layers that also provide mechanical rigidity. The polymerisation causes a colour change in the film that is proportional to the radiation dose. The colour change is measured (transmittance, optical dentistry or reflectance) using a flat bed scanner and related to the dose with a calibration curve. To obtain accurate and reproducible results with Radiochromic film a protocol for handling, calibrating and measuring dose with film must be followed.

The first study by Reyhan et al (2015) investigating the effect a magnetic field has on the polymerisation of EBT2 radiochromic film, sequentially exposed film to radiation then the magnetic field of an MRI scanner and vise versa [77]. The study used the red channel of transmission scans and observed an underdose effect both when the film was exposed to the MRI's magnetic field before and after irradiation. The magnitude of the effect was 5.1% for both cases at 800 cGy and was higher for lower dose levels. Reynoso et al investigated the effect simultaneous exposure of a 0.35 T magnetic field and irradiation with a Co-60 radiation source on EBT2 radiochromic film using the viewray system and reported a decrease in net optical density of 8.7%, 8% and 4.3% for the red, green and blue channel respectively when the film was irradiation in the presence of the magnetic field [78]. Roed et al investigated the response of EBT3 irradiated with a ^{60}Co radiation source in the presence of a 1.5 T magnetic field induced by an electromagnet [79]. An Epson 10000 XL flatbed scanner with the red-channel was used to analyse the film and an under-response of less than 2% was observed for 2, 4 and 8 Gy of dose delivered to the film. Delfs et al used an electromagnet to produce 0.35 and 1.42 T magnetic fields with a 6 MV linac beam to investigate the response of EBT3 film and observed a decrease in optical density resulting in a of 2.1% increase in dose required to achieve the same optical density as the films irradiated without a magnetic field [80]. The response of EBT3 irradiated using a ^{60}Co source in the 0.35 T field of an MRIdian was investigated by Barten et al, the study described an approximately 1.5% decrease in the dose response for films irradiated in the 0.35T field compared to those irradiated at 0 T [81]. Padilla-

Cabal et al investigated the dosimetric characteristics of EBT3 films using clinical proton beams in the 62.4–252.6 MeV energy range for magnetic field strengths B = 0, 0.5, and 1 T, concluding that the magnetic field had negligible influence on dose response of EBT3 film [82]. Microstructure changes in EBT2, EBT3 and EBT-XD films due to magnetic field and radiation was investigated by Volotskova et al using scanning electron microscopic (SEM) analysis for film irradiated before and after being exposed to 1.5 and 3 T magnetic fields from an MRI. The authors concluded the magnetic field alone did not produce any significant changes in the polymerisation [83]. The effect of 0.35 T magnetic field on EBT3 and EBT-XD film irradiated from 1 Gy to 20 Gy using 6 MV flattening filter free (FFF) x-rays from a MRIdian linear accelerator was investigated by Darafsheh et al using both net optical density and absorbance spectra [84]. They reported no significant differences in either the net optical density or net absorbance of the films due to presence of magnetic field during irradiation.

Studies investigating the use of radiochromic film in a magnetic field have reported inconsistent findings with the observed impact on the response of radiochromic film relative to dose varying in both magnitude and direction. A summary of studies investigating the response of film in a magnetic field is presented in Table 2.1.

EBT3 film dosimetry is widely used in proton therapy for relative dose measurements [85, 86]. Several studies have implemented the use of EBT3 film in proton beams in a magnetic field [82, 87, 88]. The feasibility of using EBT3 film for MRI guided proton therapy dosimetry was investigated by Padilla-Cabal et al. The group determined that within experimental uncertainty that the presence of the transverse magnetic field had a negligible influence on dose response function of the EBT3 film [82]. Schellhammer et al used EBT3 film to measure Bragg peak deflections of 80 Mev to 180 MeV proton beams in a 0.95 T transverse magnetic field [87]. The proton beam electron return effect was investigated by Luhr et al with EBT3 film used to investigate the dose enhancement at the tissue-air interface in a 0.92 T transverse magnetic field [88].

2.6 CMRP detectors/DAQs

This section details the silicon array dosimeters and readout electronics, designed by the Centre for Medical Radiation Physics (CMRP), University of Wollongong that will be investigated in this thesis for application in MR-guided photon and proton radiotherapy.

Study	Film model	B strength	Radiation Source	Observation
Reyhan et al. 2015	EBT2	1.5 T GE MRI	6MV conventional linac	Dose under response between 5.1 and 11.4 % using red channel
Reynoso et al. 2016	EBT2	0.35 T MRIdian	^{60}Co	Under response red channel- 8.7%, green channel- 8%, blue channel – 4.3%
Roed et al. 2017	EBT3	0T 1.5 T	^{60}Co	Under response 1-3%
Defs et al. 2018	EBT3	0.35 T, 1.42 T (electromagnet)	6MV conventional linac	Up to 2.5% under response with average of 0.8% under response
Barten et al. 2018	EBT3	0.35 T MRIdian	^{60}Co and 6 MV conventional linac for 0T	Difference of + 0.9%
Billas et al. 2019	EBT3	0, 0.5, 1, 1.5, 2 T (electromagnet)	^{60}Co	–0.6% at 0.5 T up to 2.4% at 2 T
Padilla-Cabal et al. 2019	EBT3	0, 0.5 1 T (electromagnet)	Between 62.4 to 198 MeV Proton pencil beams	Negligible influence on dose response
Volotskova et al. 2019	EBT2,EBT3, EBT-XD	Siemens 1.5 and 3 T MRI	6 MV, and 6 MV FFF Varian Truebeam	No significant change in polymerization and subsequently in the net OD.
Darafsheh et al. 2019	EBT3, EBT-XD	0.35 T MRIdian	6 MV FFF MRIdian and 6 MV FFF Varian Truebeam	No significant change in film OD or film absorption spectrum.

Table 2.1: Summary of studies investigating the response of radiochromic film in the presence of a magnetic field

2.6.1 Serial Dose Magnifying Glass

The first prototype of the Dose Magnifying Glass (DMG) was an array of 128 phosphor implanted n^+ strips on a p-type silicon wafer. The sensitive area defined by a single n^+ strip was 20 µm × 5000 µm. The thickness of the silicon wafer was 375 µm and the strip pitch was 200 µm, mounted on a ceramic substrate. The characterisation of the prototype DMG for use as an intensity modulated radiotherapy quality device was performed by Wong et al [89]. The detector response was observed to vary of up to 23% for a 390-fold change in DPP, and the PDD for a 6 MV photon beam measured to 20 cm depth matched with Farmer ion chamber within 0.8%. Negligible stem effect and linear response over the range 3-300 cGy was reported. The sensitivity of the 128 channels varied within ±2%, which reduces to within 0.2% with application of a flat field calibration. The angular response of the strip detector was within 3.1% for beam angles 0°-45°, increasing up to 28.1% for the angle of 90° (along the plane of the detector). The use of the device for verification of a step-and-shoot IMRT plan was also demonstrated by Wong et al.

In an effort to reduce the angular dependence of the DMG detector the second generation was mounted on a 0.12 mm thick flexible polymide (kapton) substrate, with a closer density and effective atomix number to water than the original ceramic substrate. The 200 µm pitch and 375 µm thickness of the silicon wafer was preserved and the sensitive area of the strips was changed to 20 µm × 2000 µm. The second generation device was shown to have an improved angular dependence of 15.3% for beam angles along the plane of detector. Wong et al demonstrated use of the second generation DMG for quality assurance and plan verification of cone based stereotactic radiosurgery [90]. An initial study investigating performance of the second generation DMG for use in proton beam radiotherapy was performed by Wroe et al [74]. The study investigated depth dose and lateral beam profiles using 127 MeV and 157 MeV using the DMG and comparing the measurements with PTW parallel-plate ionisation chamber, a PTW proton-specific dosimetry diode, EBT3 Gafchromic film, and Geant4 Monte Carlo simulations. For depth dose measurements, the DMG agreed well with the PTW parallel-plate ionisation chamber and Monte Carlo simulations, for profile measurements of a 5 mm 127 MeV proton beam the full width at half maximum (FWHM) was within 0.1 mm of the Monte Carlo and EBT3 film data across all depths tested.

The number of channels was doubled to 256 for next iteration of the DMG by mounting side by side two of the 128 channel linear arrays from the previous generation on an FR4 printed circuit board (PCB). This generation was called the serial Dose Magnifying Glass (sDMG). The feasibility of using the sDMG for proton beam range

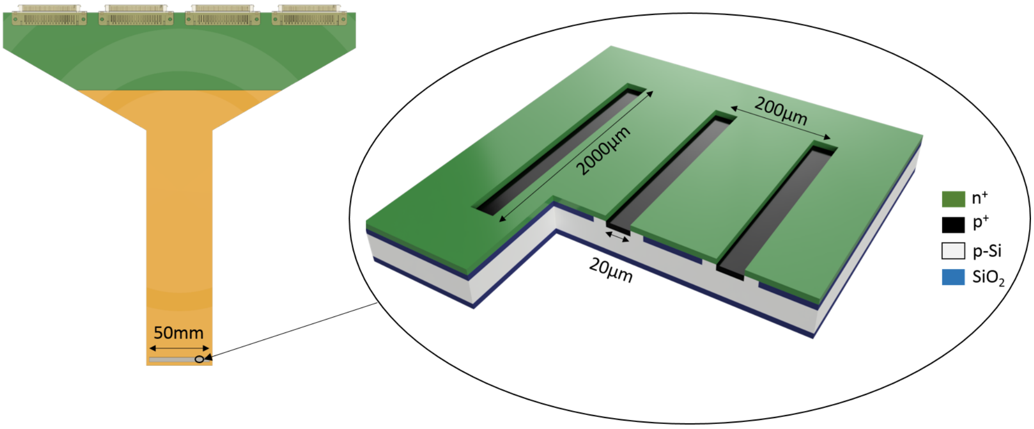

Figure 2.7: Visualisation of “sDMG-256A” with schematic diagram of detector

verification was demonstrated by Merchant et al [73]. A similar study by Debrot et al investigated the application of the sDMG to beam energy and range verification 12C ion beams [91].

The current generation of sDMG used in this thesis, the sDMG-256A has 256 phosphorous implanted (n+) strips of size 20 µm × 2000 µm with 200 µm pitch on a single bulk p-type silicon substrate. The silicon strip array is wire bonded to a kapton PCB carrier. The silicon and wire bonding are covered by an epoxy layer for protection. The kapton substrate has a density of 1.42 g/cm^3, and has an effective atomic number $Z_{eff} = 6.6$.

2.6.2 MagicPlate

The first generation of MagicPlate detector (MP121) utilised 121 epitaxial silicon diodes (1.5 mm × 1.5 mm × 0.38 mm) mounted in an 11 x 11 array to a 0.65 mm thick Kapton substrate using a proprietary “drop-in” technology developed by the CMRP. The MP121 array was designed to be mounted in the accessory slot below the secondary collimation of a conventional megavoltage x-Ray linac for measuring 2D fluence maps.

The performance of the MP121 was characterised by Wong et al using a Varian 2100iX linac [92]. The transmission of the array was measured to be 99% and the surface dose increase for 90 cm SSD for a 30 cm × 30 cm 6 MV field was 6.8%. The reproducibility of individual diodes was 2.1%, the array was reported to be dose rate independent and have a linear dose response over the conventional external beam radiotherapy range. Depth dose measurements agreed with ion chamber to within 0.7%. The arrays angular response was a maximum of 10.8% at gantry angle

180°, and for gantry angles of ±75° was within the range of 3.5%. Espinoza at al mounted the MP121 into a bespoke phantom designed specifically for high dose rate brachytherapy pretreatment QA and using a 1 MHz sampling rate demonstrated real-time source position tracking [93, 94].

The MP121 was the first detector developed by the CMRP to be investigated for use in MRgRT dosimetry. An initial GEANT4 simulation study by Gargett et al investigated the dose response of the MP121 within a water phantom to a 6 MV photon beam, in the presence of inline and perpendicularly aligned uniform magnetic fields of strength 0.5, 1, 1.5 and 3T [95]. For comparison all the simulations were repeated with water equivalent volume replacing the MP121. For the inline magnetic field simulations the MP121 response was within 1% of the equivalent water simulations for all field strengths investigated. For the perpendicular magnetic field orientations, the MP121 simulations showed an over response of the silicone diodes relative to water (maximum of (5.2 ± 0.8)% at 1 T) on one side of the field with an overall decreased dose relative to 0 T and an under response of the diodes on the other side of the field. Gargett et al attributed this occurrence to the relative contributions of low-energy electrons to the spectrum in this penumbra region compared to in-field where the detector response appeared unchanged.

While the MP121 used discrete silicon diodes the second generation magic plate detector (MP512) uses a monolithic bulk p-type 52 mm × 52 mm silicon substrate design with 512 ion implanted planar diodes with pixel pitch of 2 mm and individual diode size of 0.5 mm × 0.5 mm. The performance of the MP512 was characterised by Aldosari et al using a Varian 2100EX linac and a ^{60}Co source for pre irradiation [96]. The dose linearity of the MP512 was measured over 50-500 cGy ($R^2 = 0.998$), diode response varied within 0.25% of the mean after channel response equalisation was applied. The measured depth dose response for a 6 MV 10 cm × 10 cm field size agreed to within 1.3%, when compared to a CC13 ionization chamber for depths up to 30 cm in solid water (Sun Nuclear). Beam profile measurements matched EBT3 film within 2%. The MP512 was used with a HexaMotion 6D moving platform and Calypso radiofrequency tracking to measured temporal dose effects of MLC tracking for stereotactic body radiation therapy (SBRT) of lung tumors by Petasecca et al [97]. The study demonstrated the use of the MP512's pulse-by-pulse dosimetry to investigate latency effects of the tracking algorithm. Stansook et al investigated the angular dependence of the MP512 for small field dosimetry for field sizes ranging from 1 cm × 1 cm to 10 cm × 10 cm for both 6 MV and 10 MV on a Varian 2100iX linac observing up to 18.5 ± 0.5% for 6 MV fields orientation along the detector plane and a minimal effect of field size on angular dependence [98].

The application of the MP512 for relative dosimetry in an MRI-Linac like environment was first investigated by Gargett et al [99]. The study used a semi portable permanent magnet device (discussed in detail in chapter 3) with a Varian 2100iX to investigate the effects of a 1.2 T magnetic field on the response of the MP512. Profile measurements at 1.2 T were performed with the MP512, EBT3 and further investigated using Mote Carlo simulations (GEANT4). The experimental measurements of beam profiles agree within 0.5 mm for penumbral width measurement and FWHM of square fields ranging from 0.75 cm × 0.75 cm to 2.25 cm × 2.25 cm in both perpendicular and inline magnetic field orientations.

The first tests of a CMRP detector system on an MRI-Linac was performed by Alnaghy et al using the MP512 at the Australian MRI-Linac system [100]. The authors successfully measured beam profiles with the MP512 and demonstrated less than 1 mm average differences between the MP512 and film for FWHM and 80–20% penumbral widths when measuring without simultaneous imaging. This study investigated the possibility of dosimetry during magnetic resonance imaging, however the imaging introduced significant noise into the measurements. Aluminium radio frequency shielding was used to reduce the noise in the MP512 system however resulted in a degradation of image quality.

2.6.3 DUO

DUO detector is a monolithic silicon radiation detector designed by the Centre of Medical Radiation Physics (CMRP) at the University of Wollongong (UOW). The detector sensitive volumes are arranged in two orthogonal linear arrays with 253 pixels in each each arm of the array includeing the shared cental pixel, DUO uses a 350 um thick p-type bulk silicon substrate. The central pixel arrangment of the DUO is shown in Fig 2.8, the size of the central pixel is 180 µm × 180 µm. The four pixels immediatly adjacent to the central pixel are 160 µm × 200 µm and the remaining pixels have a size of 40 µm × 800 µm with the long axis orthogonal to the direction of the arms of the array. The detector has a pitch of 200 µm to provide high spatial resolution for measurements of stereotactic radiotherapy beam profiles. The total area of the array is 52 mm × 52 mm. Characterisation of the DUO was performed by Shukaili et al [101]. Detector characterisation included DPP dependence, PDD comparisons, beam profiles and output factors. The DPP response varied by 23% for a DPP variation of 2.78x10^{-4} to 2.1x10^{-5} Gy/pulse. Measurements of PDD were compared to Markus chamber, percentage difference was within 1.5% for depths beyond the surface. Small field beam profiles (0.5 cm^2 - 5 cm^2) compared well with EBT3 film, FWHM agreed within 1%. Small field output factors agreed within 1.8% for field sizes 0.5 cm × 0.5 cm to 30 cm × 30 cm with an air gap of 0.5 mm introduced

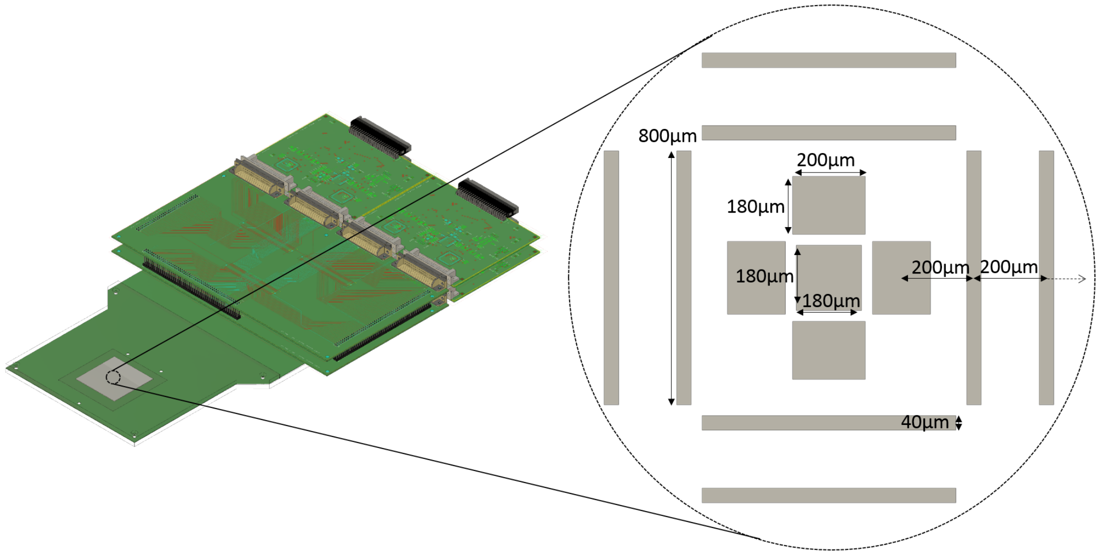

Figure 2.8: Visualisation of "DUO" detector showing the configuration of the central detector sensitive volumes.

to the detector packaging. Shukaili et al also compared the use of the DUO detector to EBT3 film and the IBA Stereotactic diode (SFD) for relative dosimetry of Elekta stereotactic radiosurgery cone collimators, finding the DUO agreed with the EBT3 and SFD within ±0.5 mm in the FWHM, and ±0.7 mm in the penumbra region for profiles and ±2% for output factors for cones ranging from 5 mm to 50 mm diameter [102]. Radiation damage effects of the DUO was investigated by Porumb et al by irradiating the DUO array in 20 kGy steps up to 140 kGy using a ^{60}Co source [103]. The authors demonstrated the DUO's response stabilises after pre-irradiation of 120 kGy with ^{60}Co.

The performance of the DUO in a 1.2 T transverse and 0.95 T inline magnetic field was investigated by Alnaghy et al, comparing dose distribution profile measurements between the DUO, Gafchromic EBT3 film and previously published MP512 results for the same magnetic field arrangement and Varian 2100IX linac source [104]. Field sizes ranging from $0.8\,\text{cm} \times 0.8\,\text{cm}$ to $2.3\,\text{cm} \times 2.3\,\text{cm}$ were measured in solid water and solid lung phantoms, profiles agreed to within ±0.5 mm of the average for the three detectors.

2.6.4 Data Acquisition System

The Data Acquisition (DAQ) System developed by the CMRP used with the sDMG, MP512 and DUO is a modular design allowing readout of up to 512 individual channels simultaneously. The DAQ has two main boards, the analogue front end (AFE) boards and the field programmable gate array (FPGA) board. The AFE boards each have two commercial electrometers named AFE0064 from Texas Instrument (TI)

(Texas Instruments, 2009) coupled to a 16-bit quad channel analogue-to-digital converter (ADC). The 'AFE0064' has 64 parallel inputs, each AFE board may readout 128 individual channels. The FPGA drives the AFE boards, synchronising the devices by a custom designed internal clock manager. Modern medical linacs are based on a pulsed radiation beam with pulse duration in the order of a few milliseconds and pulse repetition rate up to 400 Hz. The DAQ has two trigger modes, synchronised with by an external trigger or asynchronised using an internal trigger. By using a sync signal provided by the pulsed radiation source the effects of electronic noise and leakage current are minimised. The system dead time is managed by reading out the integrators while the beam is off. Further details and characterisation of the DAQ is described in detail by Fuduli et al [105, 106].

Users control the DAQ system via an in-house developed graphical user interface (GUI) that runs on the user's personal computer (PC) that connects to the FPGA board via USB2.0. The GUI is used to set acquisition parameters such as gain range, buffer size, integration time, select triggering mode and acquisition length. The GUI also have various tools to review the data including 2D displays of detector response, or time response profile of an individual detector channel.

Chapter 3

A Portable Magnetic Apparatus for Radiation Oncology Studies

This chapter contains results that have been published in the journal of Medical Physics.

Causer, T., Metcalfe, P., Rosenfeld, A., Oborn, B.M., "A portable magnet for radiation biology and dosimetry studies in magnetic fields" *Medical Physics*, vol. 49, pp 1924-1931, 2022.

Contributions: Causer, T. performed the measurements, analyzed the data, and wrote the manuscript with support from all the authors. Oborn, B.M conceptualized the design of MARDOS. Metcalfe, P., Rosenfeld, A., Oborn, B.M were involved in planning experiments and supervising the work. The University of Wollongong engineering workshop constructed the magnetic device.

3.1 Overview

Real-time MRI-guided radiotherapy has been clinically delivered through the ViewRay MRIdian system since 2014 [14]. The Elekta Unity system has also been treating patients since 2018 [17]. Along with these clinical systems, at least 2 other programs have advanced prototype MRI-linac systems that are pre-clinical. These include the Magnettx Aurora system and the Australian MRI-linac Program system [19, 107]. Along with these MRI-linac based radiotherapy systems, there is attention now on developing MRI-guided particle therapy [50, 51]. Futher to this, there is a surge in the possible potential of FLASH radiotherapy to safely deliver ultra fast radiotherapy fractions [108, 109]. It would be perhaps not an overstatement to predict or expect that robust real-time MRI-guidance would provide the most accurate patient daily anatomy for delivery FLASH radiotherapy with confidence, at least from a classic dosimetry point of view. With all this in mind, the impact of magnetic fields in image guided radiotherapy is at least for the forseeable future unavoidable. This impact, at least in a clear and demonstrated way, is limited mostly to macroscopic dose changes due to the changes in the charged particle transport in radiotherapy. For x-ray based beams, the secondary electron paths are significantly impacted. While for particle beams both the primary beam and secondary electrons are impacted. Somewhat less demonstrated is the impacts at the microscopic level, or biological changes. There is mostly a null result reported for any biological changes caused by strong magnetic fields during radiotherapy. A recent paper however does show a unquie cell death increase in what seems related to magnetic field direction with carbon beams [110]. With the already complicated and largely unknown mechanism behind FLASH radiotherapy, perhaps it would be wise to consider that flash radiobiology should be also studied with the inclusion of magnetic fields.

Cell culture studies may be affected by the heat production of electromagnets used in semi-portable magnet devices that maintain magnetic field strengths being used in clinical MR-Linac systems [111]. Researchers are increasingly interested in investigating the effects of the magnetic field on the operation of existing radiation detectors used for radiation dosimetry and radiotherapy quality assurance measurements and developing new devices that are less affected by magnetic fields [55, 112–114]. Many radiation detector types exhibit a temperature dependent response including ionisation chambers, diodes and plastic scintillation detectors. Accurate experimental characterisation of the influence of the magnetic field on response for such devices would benefit from a stable thermal environment.

The goal was to construct and characterise a portable device capable of producing strong magnetic fields over a volume large enough to support fundamental small scale experiments that mimic the environment of an MRI-linac system. The device was designed to be used with a conventional non-MRI linear accelerator.

3.2 Design and construction of magnetic apparatus

The initial design of the portable magnetic field apparatus is the work of co-spervisor Dr Oborn. The design requirements for the magnetic field apparatus are that it should provide a region of uniform magnetic field strength of at least 1 T, be capable of orienting the radiation beam both parallel and perpendicular to the magnetic field flux, be portable and be capable of mounting a variety of radiation detectors at the centre of the magnetic field. The ability to reproduce the scattering conditions without the magnetic field is also desirable for detector studies.

Using the COMSOL Multiphysic software (v4.4, Sweden (Stockholm)), possible designs of the Magnetic Apparatus for RaDiation Oncology Studies (MARDOS), based on the available neodymium-iron-boron ($Nd_2Fe_{14}B$) magnets and limited weight of the apparatus such that it could be moved on a trolley, were modelled using finite element method to create a three-dimensional (3D) magnetic field map. The final design shown in Fig. 3.1(a) utilises two $Nd_2Fe_{14}B$ permanent magnet banks (5 × 5 matrix without the central magnet to allow passage of radiation beams), an iron yoke with adjustable pole gap and exchangeable focusing cones. An adjustable pole gap is desirable as it allows the magnetic field strength between the cones to be adjusted via moving the magnet banks closer together. The exchangeable focusing cones are required to allow inline and perpendicular beam orientations. A cone set specifically for University of Wollongong detector arrays such as the M512 was designed and constructed to allow detector arrays that are physically wider than the maximum cone gap to be orientated perpendicular to the magnetic field direction [99]. The allowable pole gap between the magnet banks when focusing cones are not attached can be adjusted between 150mm when fully open with a COMSOL simulated field strength of 0.265 T to 50 mm when fully closed with a magnetic field strength of 0.49 T. The flux focusing cones designed specifically to fit the CMRP detectors (cone type A) within MARDOS allow up to a 30mm cone gap with the detectors fitted, this is the cone that is characterised in this chapter and is shown in as part of the magnet system in figures 3.1 and 3.10. Cone tips (cone type B - shown in figure 3.10) that allow an unobstructed beam portal though the apparatus parallel to the magnetic field of various square openings of 15 mm x 15 mm, 25 mm x 25 mm and 35 mm x 35 mm allow up to a 50 mm cone gap. The configurations of the magnetic apparatus have been modelled in COMSOL are summarised in table 3.1.

Construction of the apparatus was performed by the University of Wollongong engineering workshop, 3D computer aided design (CAD) files were provided for precision machining of the focusing cones and iron yoke. The apparatus was attached to a hydraulic jack and trolley system for safety and portability. A four point levelling system was also designed and attached to the frame of the system.

3.3 Finite element modelling of the magnetic field

To characterise the magnetic field of the magnet assembly, finite element modelling (FEM) calculations were used to calculate field data at each point in space. The

Cone Type	Cone portal opening (mm)	Physical Gap (mm)	Magnetic Field Strength at centre of magnet (T)
none	NA	150	0.265
none	NA	100	0.353
none	NA	90	0.373
none	NA	50	0.49
Type A*	NA	30	1.19
Type B	35	50	0.64
Type B	25	50	0.686
Type B	15	50	0.713
Type B	35	30	0.82
Type B	25	30	0.965
Type B	15	30	1.05

Table 3.1: Magnetic field strength of simulated MARDOS configurations. *Configuration of MARDOS experimentally validated in this thesis chapter

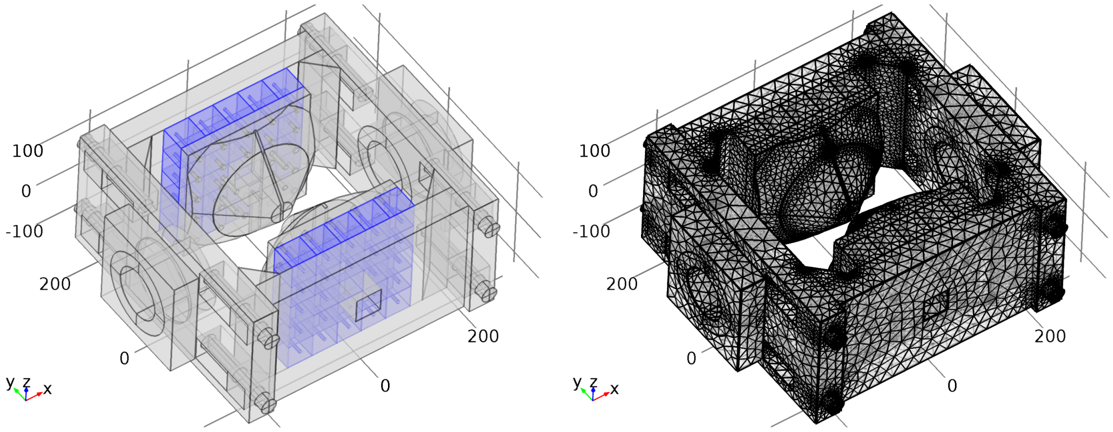

(a) **(b)**

Figure 3.1: (a) COMSOL model of MARDOS, $Nd_2Fe_{14}B$ magnets are shown in blue, iron is shown in grey. (b) COMSOL mesh used in magnetic field calculations. Units are mm.

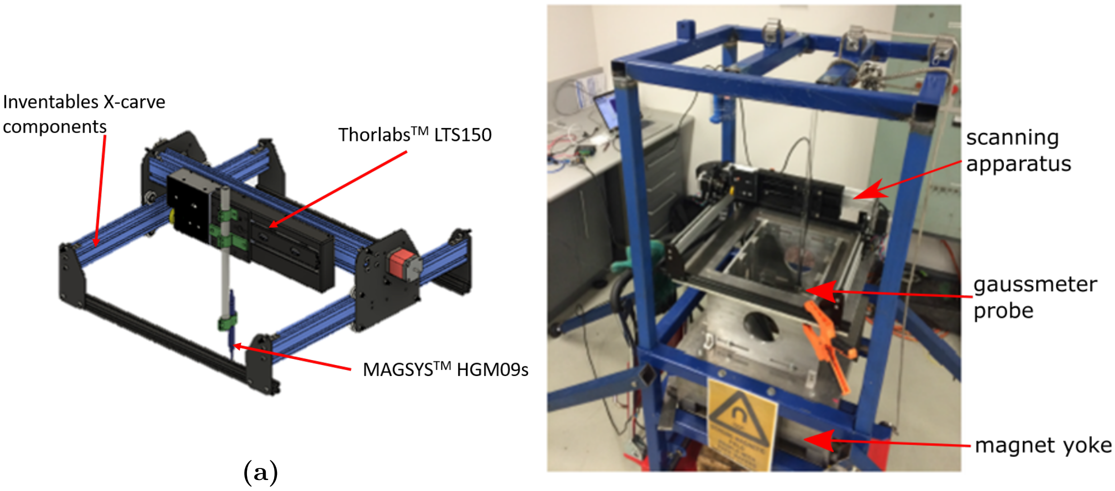

(a)

(b)

Figure 3.2: (a) CAD model of magnetic field scannning system (b) Photograph of MARDOS with magnetic field scanning system

FEM calculations were performed using COMSOL Multiphysics (v4.4). Three materials were used in the calculations; air, $Nd_2Fe_{14}B$ and steel (American Iron and Steel Institute 1020). The material properties for Steel 1020 and air were taken from the COMSOL material library using the predefined material. The remanent field strength $B_r = 1.19$ T of $Nd_2Fe_{14}B$ magnets was obtained from the manufacturer.

3.4 Apparatus magnetic field verification

Although the apparatus was precision machined to the computer aided design models, verification of the modelled magnetic field was required to assess the effects of steel grade in the yoke, $Nd_2Fe_{14}B$ permanent magnet banks, effects of the steel frame and minor machining differences.

An automated two-dimensional (2D) scanning system was designed and constructed using the combination of Thorlabs^{TM} LTS150 Linear Translation Stage with Integrated Controller (New Jersey, USA), open-source Inventables X-carve (Chicago, USA) components, 3D printed mounts and a MAGSYS HGM09s Gaussmeter (Dortmund, Germany) shown mounted on the magnetic field scannning system Fig. 3.2(b). The measurement probe is suspended via an acrylic rod at the central plane between the magnets focusing cones.

3.4.1 Generating of scanning path

The x and y coordinate positions that can be scanned without colliding the probe with the steel cones in each chosen z plane may be calculated by defining a grid in the desired scanning plane and testing each point in that grid falls inside or outside

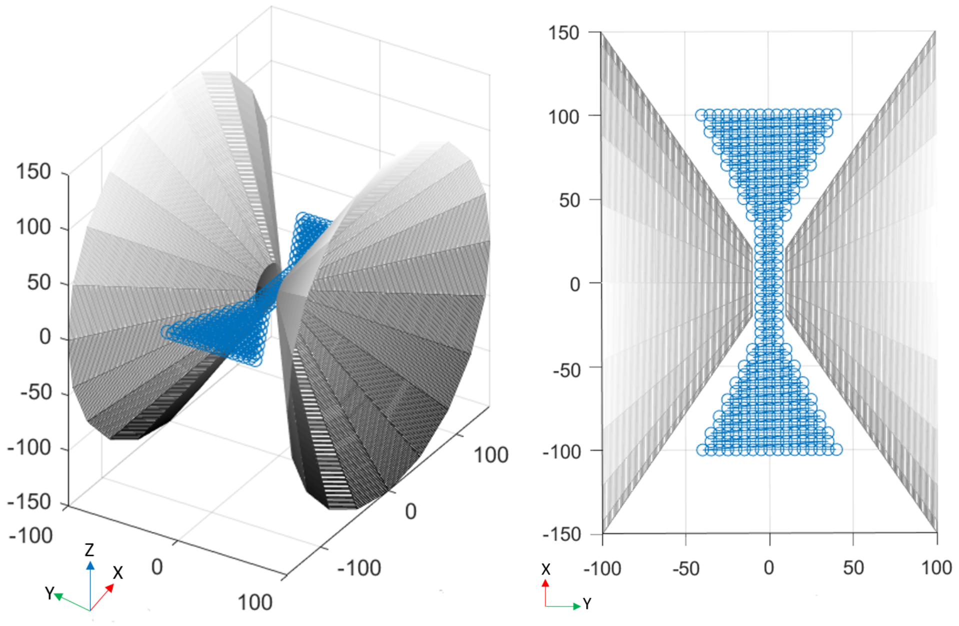

(a) (b)

Figure 3.3: MATLAB visualisation of scan path, blue circles indicate measurement point locations, the blue line indicates the scanning path of the probe (a) 3D view of the scan path between the cones (b) top down 2D view of the scan path in the central XY-plane.

the cones.

Creating a scan path that follows a raster pattern allows each point to be measured without collision and results in an hourglass shape of measured values in the chosen plane as shown for the central XY-plane in Fig. 3.3. The Thorlabs LTS150 linear stage, MAGSYS HGM09s gaussmeter support serial communication and the stepper motors controlling the y-axis position were moved using a Geckodrive G201X stepper motor driver controlled via a Arduino UNO microcontroller. The scanning routine was scripted in MATLAB (R2015b).

3.5 Results

3.5.1 Magnetic field map calculated by finite element modelling

A complete 3D solution of the magnetic field of MARDOS was calculated using COMSOL Multiphysics (v4.4, Sweden (Stockholm)). The calculated magnet flux density (T) at central XY-plane of MARDOS in shown in Fig. 3.4, the magnified view of the central region shows a calculated magnet flux density of 1.19 T.

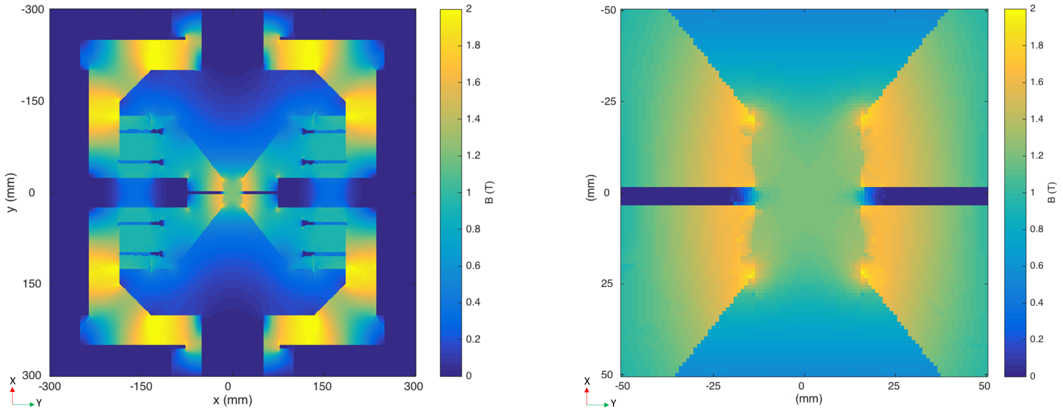

(a)

(b)

Figure 3.4: Calculation result of magnetic flux distribution norm $|B|$ in central XY-plane (z=0) (a) The full geometry implemented in COMSOL. (b) magnified view of the central air gap.

3.5.2 Magnetic field measurements

A comparison of FEM calculation and measured magnetic field in the x and y direction (B_x and B_y) for the central XY-plane are shown in Fig. 3.5 and 3.7 respectively. The histogram displayed in Fig. 3.9 shows that 99.80 % of points measured are within ±2 % of the FEM calculated B_y and 99.26 % of all points measured are within 2 % of the FEM calculated B_x. As presented in Fig 3.6(a), the central x-axis scans of the main field component B_y show a uniform region within the magnet's air gap, with a field maximum of 1.19 T at the magnet systems centre. The gradient of the field strength adjacent to the uniform region displays a sigmoidal drop-off, the location of the inflection point is at the edge of the focusing cones, which is ±15 mm in the x direction. Profile plots of the minor B_x component of the magnetic field along the central x- and y-axis of MARDOS show similar profile between the measured and calculated result as displayed in Fig. 3.8, an offset of 0.02 T is observed between the measured and FEM calculated results.

3.6 Conclusion

A portable permanent magnet based system employing an adjustable iron yoke and magnetic field focusing cones was designed, constructed and tested. The apparatus utilises two $Nd_2Fe_{14}B$ permanent magnet banks totalling around 50 kg in mass to generate a magnetic field across the pole gap. The yoke design allows adjustment of the pole gap and exchanging of the focusing cones. Further to this, beam portal holes are present in the yoke and focusing cones, allowing for radiation beams of up to 5 × 5 cm^2 to pass through the region of high magnetic field between the focusing cone

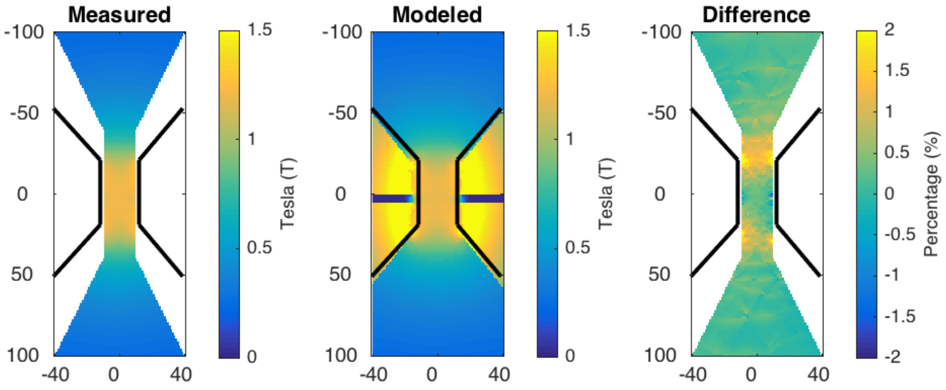

Figure 3.5: Comparison of measured and calculated magnetic field component B_y at central axis of magnet, left: Measured magnetic field strength, Centre: modeled magnetic field strength, Right: difference of measured and modeled field

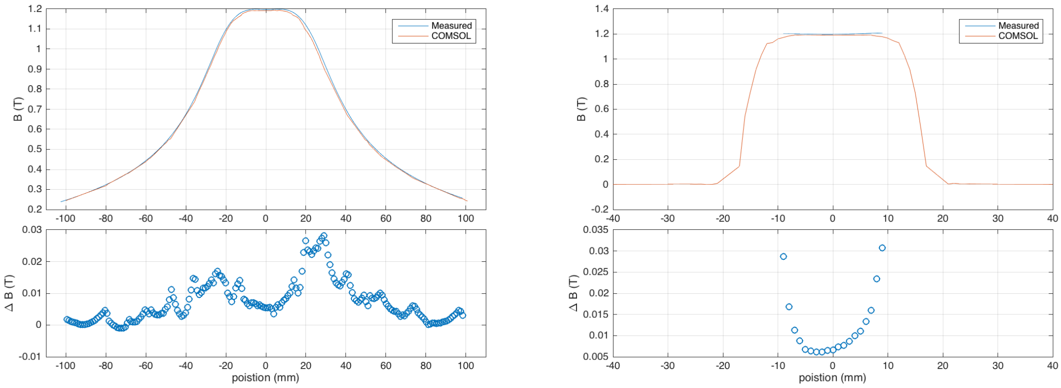

(a) **(b)**

Figure 3.6: Scans of the main magnetic field component B_y along the (a) x-axis and (b) y-axis of the magnet.

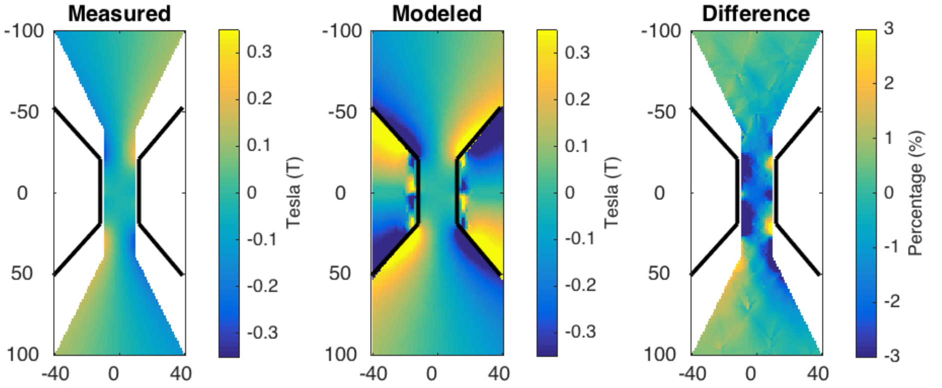

Figure 3.7: Comparison of measured and calculated magnetic field component B_x at central axis of magnet, left: Measured magnetic field strength, Centre: modeled magnetic field strength, Right: difference of measured and modeled field

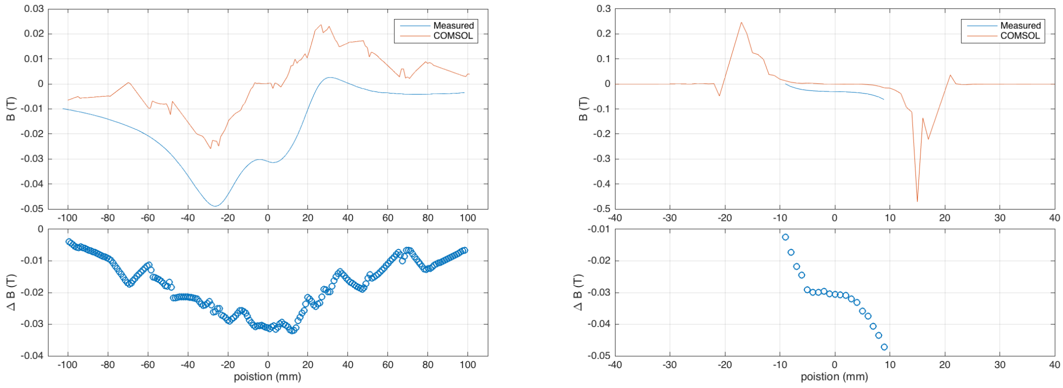

(a) **(b)**

Figure 3.8: Scans of the minor magnetic field component B_x along the (a) x-axis and (b) y-axis of the magnet.

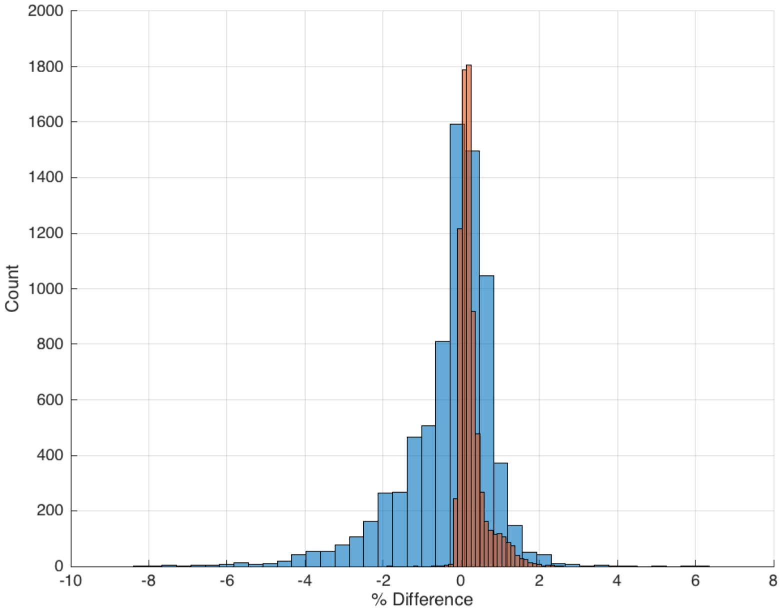

Figure 3.9: Histogram of differences (%) at each measured point to FEM calculation (blue - B_y, red - B_x)

tips. Finite element magnetic modelling has been performed to predict the performance of the device, along with automated physical measurements of the magnetic field components at various locations. The adjustable pole gap and interchangeable cones allows rapid adjustment of the experimental set-up to allow different styles of measurements to be performed. A mostly uniform magnetic field of 1.2 T can be achieved over a volume of at least $3 \times 3 \times 3$ cm^3. The MARDOS apparatus uses detachable trolley wheels to transport the device between the Linac bunker and its storage location at the Hospital. Due to a total weight of approximately 100kg moving the device between hospitals and the University requires the use of a truck or trailer. The University of Wollongong engineering workshop assisted with transporting MARDOS between the University campus and Illawarra Cancer Care where it was used for work outlined in Chapter 4. Alignment of the apparatus with the x-ray beam of a medical linear accelerator is aided by the detachable 4-point levelling system, however a system for fine translational adjustment was not incorporated into the design of MARDOS. Course translation movement of the apparatus are preformed using the removable trolley wheels with finer adjustments made by sliding the device.

University of Wollongong Work Safety Officer was employed to assess the safety of the device as per standard protocol and the device was deemed as having some potential pinch-points. A work perimeter of 1.5 m was setup using barricades around the device where only authorised persons familiar with working with strong magnets are permitted to enter.

The measurement of the main field component B_y showed excellent agreement with the FEM calculated values. The regions close to where the front of the focusing cones meets the edge of the cone are the location where the largest disagreement occurs between the modelled and measured magnetic field for both the B_y and B_x components. The minor field component B_x is two orders of magnitude smaller then the B_y. The observed systematic offset between the measured and calculated values of B_y may be partly due the hall probe alignment in the measurements.

The main aim in performing such a field analysis was the desire to use magnetic field information for Monte-Carlo radiation transport simulations of experiments performed using the portable specialised magnetic field apparatus. The intended x-ray beam paths are shown in Fig 3.10 (A and B vectors). Both the fringe region and central region of the magnetic field have been measured at the central plane for beam path B and greater than 99% of points measured more the 5 mm from the cones, agreeing with the FEM calculations to within 2%.

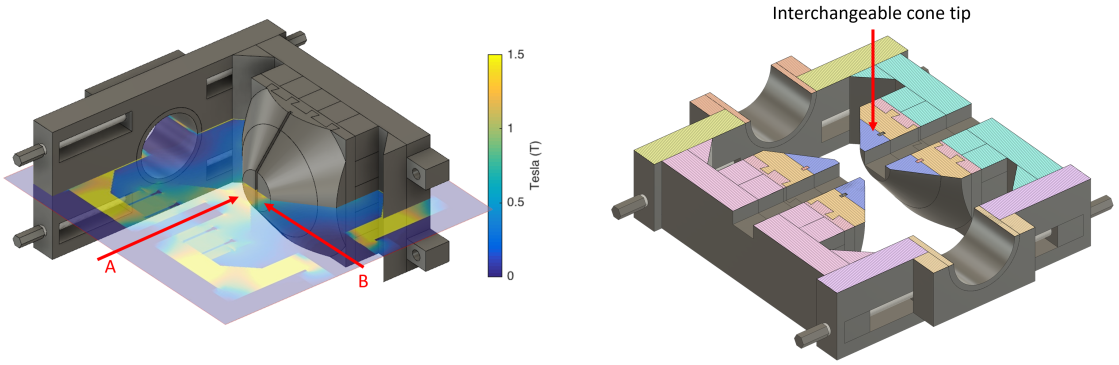

Figure 3.10: Left: Visualisation of MARDOS showing intended x-ray beam paths, A is inline with the main magnetic field component B_y and B is perpendicular to the main magnetic field component B_y. Right: Sectioned view of MARDOS apparatus with cone tips used for inline x-ray beam arrangements

Chapter 4

Characterisation of a high spatiotemporal resolution monolithic silicon strip detector for MRI-linac dosimetry

This chapter contains results that have been published in the Journal of Physics: Conference Series.

Causer, T., Chapman, T. Oborn, B.M., Davis, J., Petasecca, M., Rosenfeld, A., Metcalfe, P., "Characterization of a high spatiotemporal resolution monolithic silicon strip detector for MRI-linac dosimetry" *Journal of Physics: Conference Series*, no. 1154 012006, 2019.

Contributions: Causer T. designed the experiments as well as collected and analysed the data presented in this chapter. Oborn, B.M and Chapman T. assisted with experiments. Metcalfe, P., Rosenfeld, A., Oborn, B.M were involved in planning experiments and supervising the work. Access to linear accelerators was kindly provided by the Illawarra Cancer Care Centre.

4.1 Overview

There are now multiple vendors offering radiotherapy systems with real-time magnetic resonance (MR) image guidance. These systems can provide superior soft tissue contrast compared to kV photon image guidance technologies. The ViewRay MRIdian Linac system combines 6 MV flattening-filter free linac with a 0.35 T MRI scanner [14]. The Elekta Unity integrates a 7 MV flattening-filter free linac

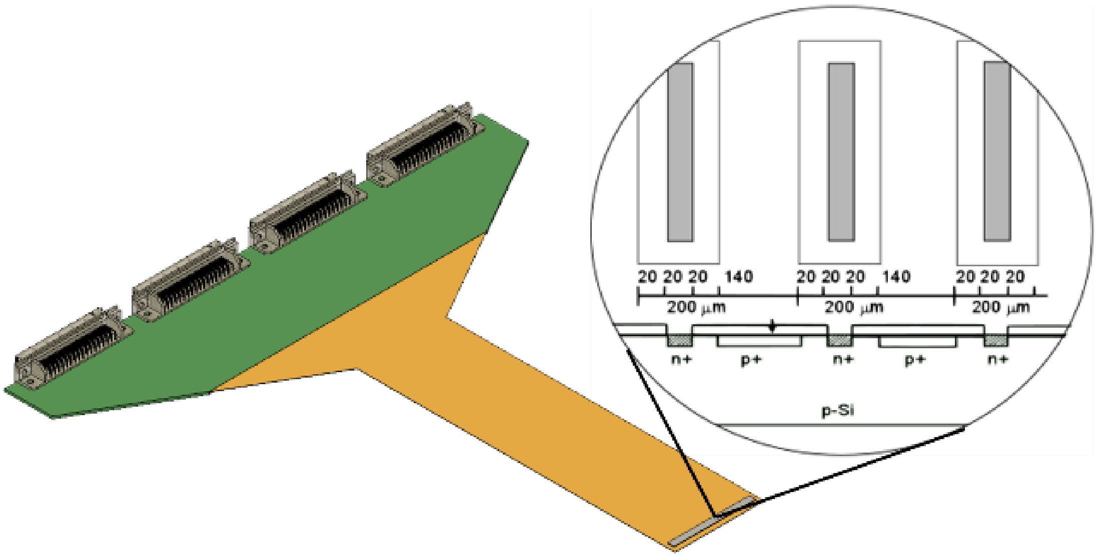

Figure 4.1: sDMG-256A, green is FR4 section of PCB, orange is the flexible polymide

system with a 1.5 T MRI scanner [17]. In both systems the magnetic field axis is perpendicular to the beam axis. With this configuration the Lorentz force that acts on secondary electrons causes electron return effect (ERE) at high/low density interfaces and creates lateral asymmetry in beam penumbra [23].

To meet the needs of quality assurance of small fields delivered in the presence of a strong magnetic field detector systems with high spatial resolution, high temporal resolution and magnetic insensitivity are required. Monolithic silicon strip detectors have been shown to be suitable for small field dosimetry of linac beams [102]. The introduction of magnetic fields presents new challenges in detector design. In this work we characterise the dosimetric performance of a monolithic silicon strip detector mounted to a flexible polymide printed circuit board (PCB) intended for use in MRI-linac dosimetry.

The monolithic silicon strip detector, (sDMG-256A) consists of 256 phosphorous implanted (n+) strips of size 20 µm × 2000 µm with 200 µm pitch on a bulk p-type silicon substrate. The silicon strip array is wire bonded to a flexible polymide (Kapton) PCB carrier, shown in Fig. 4.1. The silicon and wire bonding are covered by a protective epoxy layer. The data acquisition (DAQ) system has been developed in house at the Centre for Medical Radiation Physics, it is based around the AFE0064 multichannel electrometer chip from Texas Instruments. To read out 256 channels, two analog-to-digital converters are used with four AFE0064's all synchronised by a field-programmable gate array (FPGA). The data is passed from the FPGA to the user's computer via USB2.0 and accessed with a custom graphical user interface.

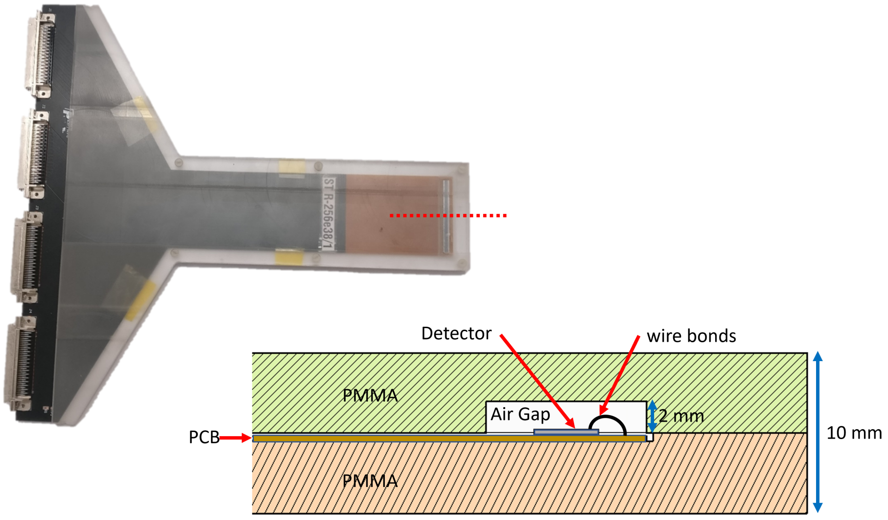

Figure 4.2: Photograph of sDMG-256A mounted in PMMA detector packaging with red dashed line indicating location of cross-section of the detector geometry showing the PMMA phantom and air gap.

4.2 Detector Characterisation

4.2.1 Dose linearity

Linearity measurements were performed using a Varian 2100iX linear accelerator (Varian Medical Systems, Palo Alto, CA). The sDMG-256A was housed in PMMA slab insert shown in Fig 4.2. The detector was placed with the sensitive volume at the depth of maximum dose (dmax) of a 6 MV photon beam with a nominal 10 cm × 10 cm jaw defined field. The source-to-surface distance (SSD) was 100 cm and the detector was irradiated with monitor unit (MU) values from 20-1000. To correct for possible variations in the accelerator output, an IBA CC13 ionization chamber (IBA Dosimetry GmbH, Schwarzenbruck, Germany) was used as the reference detector. The dose response of the sDMG-256A relative to the reference detector for (20-1000) cGy is shown in Fig. 4.3 displaying a linear response (R^2 = 1).

4.2.2 Dose per pulse dependence (DPP)

Dose per pulse dependence (DPP) was measured over the range (0.29-4.66)x10^{-4} Gy/pulse. The measurements were performed on a Varian 2100iX linear accelerator (Varian Medical Systems, Palo Alto, CA) with the gantry at 90° and the detector and phantom setup on a movable trolley. The detector was placed a 5 cm depth in solid water, 10 cm backscatter and the SSD was varied from 70 cm - 300 cm. The dose per pulse at depth of maximum dose for machines reference conditions (field size = 10 cm x 10 cm, 100 cm SSD) the was determined by dividing the time average dose rate for

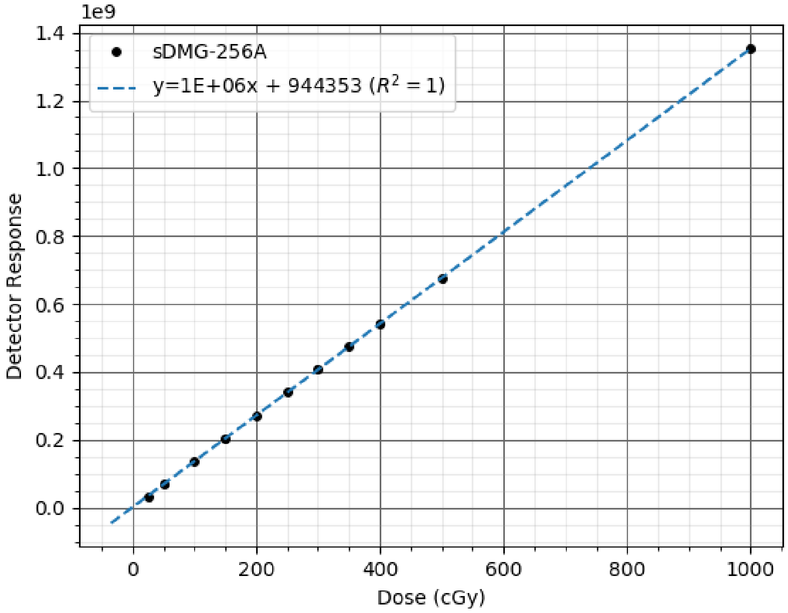

Figure 4.3: Response of the central pixel of the sDMG-256A to accumulated dose. Solid line represents the linear fit.

the Linac's reference conditions (6Gy/min) by the pulse repetition frequency (360 Hz), then correcting for the PDD at 5cm. At each measurement point a IBA CC13 ionisation chamber (IBA Dosimetry GmbH, Schwarzenbruck, Germany) reference measurement was taken and corrected for recombination using two voltage analysis [115]. The dose per pulse dependence relative to the refference CC13 chamber shown in Fig. 4.4 displays a 10.3% variation over the range (0.29-4.65) x 10^{-4} Gy/pulse.

4.2.3 Angular dependence

The angular dependence was investigated using a cylindrical rotating QA phantom the RT-smartIMRT (dose.point GmbH, Wiesloch, Germany) shown in Fig. 4.5(b). The RT-smartIMRT phantom is designed to use solid water slab geometry detector inserts, an acrylic slab was machined to house the sDMG-256A centrally within the phantom such that the central detector channel was coincident with the central axis of rotation of the RT-smartIMRT phantom. Measurements were performed using a Varian 2100iX linear accelerator (Varian Medical Systems, Palo Alto, CA) with the phantom and detector setup at 100 cm source-to-detector distance (SDD), a nominal 10 cm × 10 cm jaw defined field was used with 6MV beam energy. The linac gantry was kept stationary and the RT-smartIMRT phantom was rotated, measurements were taken every 15°. The angular response is given by the ratio of charge readings for a given beam angle of incidence to the case when the radiation beam is perpendicular to detector plane.

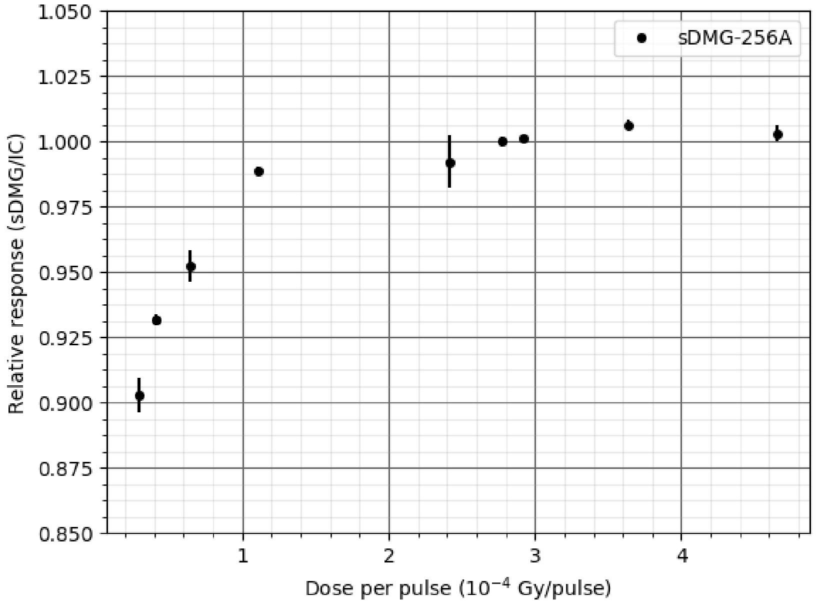

Figure 4.4: sDMG-Dose per pulse response normalized to 2.78x10^{-4} Gy/pulse

$$Angular\ dependence, A_\theta = \frac{R_\theta}{R_{\theta=0}} \tag{4.1}$$

Where, R_θ is the response of the central detector channel at angle θ. The angular response of the central channel of the sDMG-256A is observed to decrease relative to perpendicular incidence for all angles, with a maxiumum 20% decrease at 90° as shown in figure 4.5(a). The polar plot of angular response shows the variation in response is mostly symmetrical about perpendicular angle of incidence 0°. The observed angular response of the central channel of the sDMG-256A is due primarily to the detector packaging resulting in the water equivalent path length of the beam varying with angle of incidence. A cross section of the detector packaging shown in Fig. 4.2 displays the air gap above the silicon wafer required to protect the exposed wire bonds results is a lower water equivalent path length when the detector is exposed from the front as compared to the back. Lateral irradiation at 90° and 270° of the detector results in a beam path along the monolithic silicon detector, due to the higher attenuation of silicon relative to water this results in the observed maximum response variation.

4.2.4 Uniformity of detector channel response

The response of each channel of the sDMG-256A may vary slightly due to a combination of each diodes intrinsic sensitivity and the gain of its corresponding preamplifier channel. The result is that for a uniform irradiation of the detector system a nonuni-

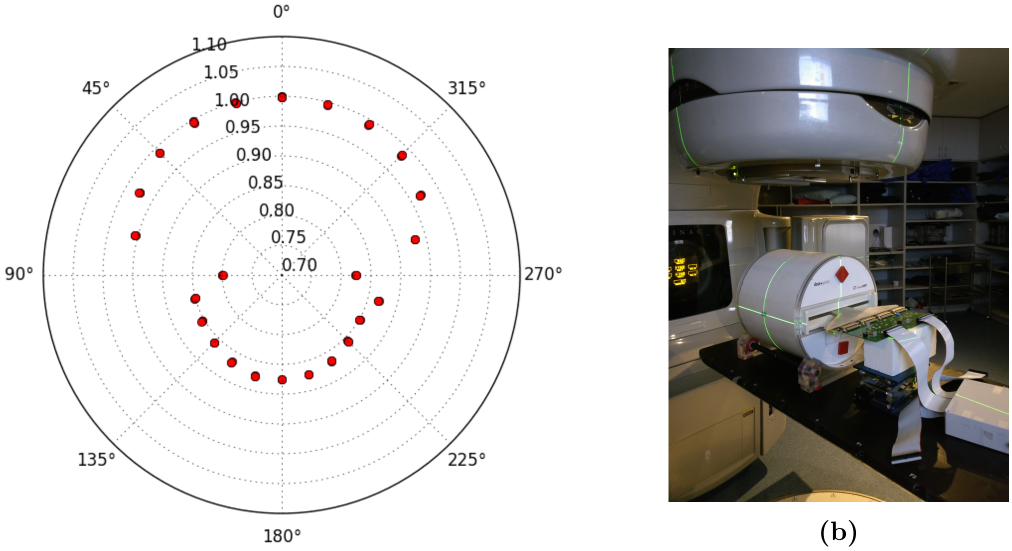

(b)

(a)

Figure 4.5: (a) Angular response of central channel, (b) dosepoint RT phantom setup for angular response assessment

form response is observed. An approach to address this is to has been presented by Wong et al [92]. By exposing the entire diode array to a uniform stimulus, calculating the average response of the diodes in the system and then normalising each channel to the average to calculate the equalisation vector.

$$F_i = \frac{X_i}{\overline{X}} \tag{4.2}$$

Where F_i is the equalisation factor vector, X_i is the individual channel response and $\bar{X}$ is the mean reading of all channels. An individual channels reading is corrected for its response relative to the other channels of the array by applying

$$X_{eq,i} = \frac{X_i}{F_i} \tag{4.3}$$

Where $X_{eq,i}$ is the equalized detector response. The uniform stimulus used was a was accessed using a 6 MV, 20 cm × 20 cm field, with the detector at depth 10 cm in a solid water phantom positioned at 100 cm SSD. Measurements were performed on a Varian 2100iX linear accelerator (Varian Medical Systems, Palo Alto, CA). The uniformity of the sDMG-256A in Fig. 4.6 shows that before applying the equalization vector detectors channel response relative to the central channel for 99% of channels were within ±5%. After channel normalisation the variation of all channels was within 0.2%.

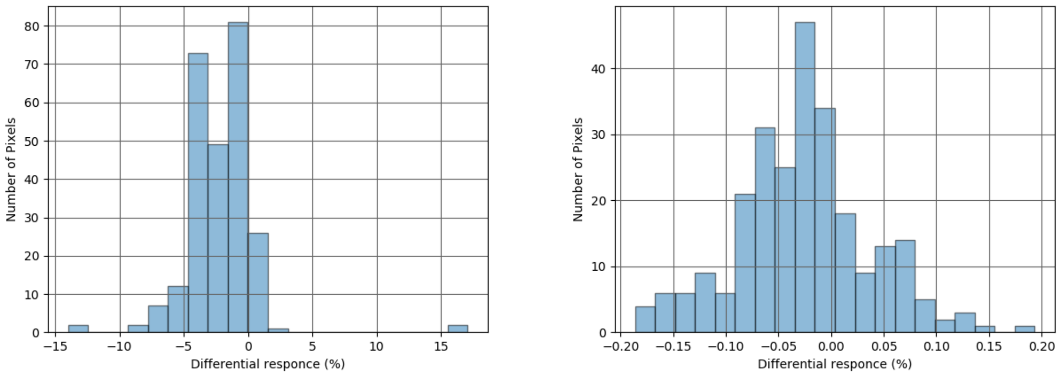

(a) **(b)**

Figure 4.6: (a) Histogram of uniformity results pre equalisation, (b) histogram of uniformity results post equalisation.

4.2.5 Percentage depth dose (PDD)

The sDMG-256A was inserted into a PMMA detector packaging shown in Fig. 4.2, composed of a slab of 3 mm on top and 5 mm on the bottom of the detector. Solid water slabs were was used to measure the PDD with 10 cm of solid water backscatter material. Depths were measured from 0.5 cm to 25 cm. The device was irradiated using a Varian 2100iX linear accelerator (Varian Medical Systems, Palo Alto, CA) with 100 MU with a 10 x 10 cm^2 field at 100 cm SSD by a 6 MV photon beam. The result was compared with measurements taken using an Advanced Markus ionisation chamber (PTW Freiburg, Germany) under the same experimental conditions (in solid water). The PDD measured with the sDMG-256A and Advanced Markus ionization chamber are plotted in Fig 4.7. The PDD curves shown in Fig 4.7 are normalized to dmax. The maximum observed variation between the two was 1.04% and 0.5cm depth, with all other depths measured within 0.4%.

4.2.6 Output factor (OF)

A field output factor is defined as the ratio of absorbed dose to water in any non-reference field to that in a reference field at a given depth [116]. Measurement of output factors may be performed by measuring the detector response as a function of field size and taking the ratio of the response relative to the reference field size as the output factor of a given field size. The response of the sDMG-256A as a function of field size was measured for jaw defined field sizes ranging from 3 cm × 3 cm to 20 cm × 20 cm in solid water. A minimum field size of 3 cm × 3 cm was chosen to maintain lateral charge particle equilibrium conditions for the reference ionisation chamber. The sDMG-256A was placed at 10 cm depth, 100 cm SSD and was irradiated using a Varian 2100iX linear accelerator (Varian

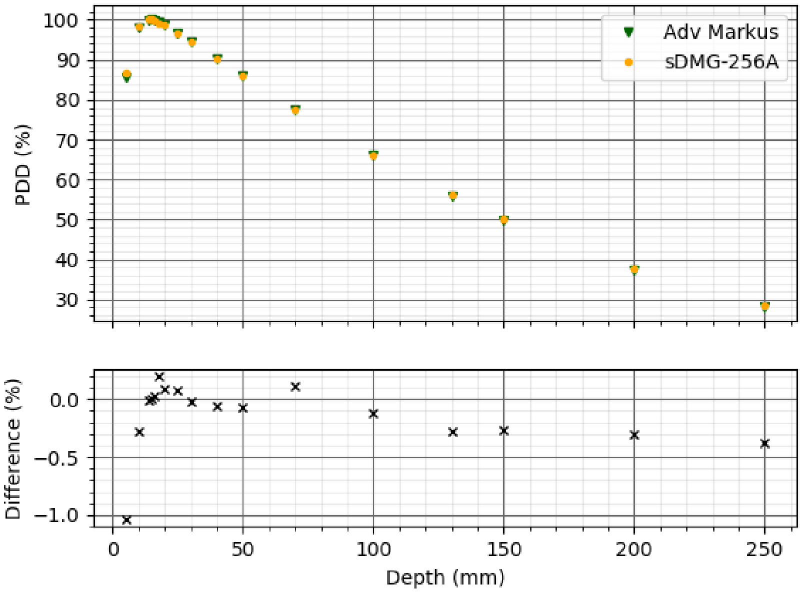

Figure 4.7: PDD measured by the sDMG-256A and Advanced Markus ionization chamber for a 6 MV, 10 cm x 10 cm field in solid water. Percentage differences are shown in the lower panel

Medical Systems, Palo Alto, CA) with 100 MU. Measurements using the same setup and linear accelerator were performed using an IBA CC13 ionisation chamber (IBA Dosimetry GmbH, Schwarzenbruck, Germany) for comparison. Fig 4.8 shows the response of the central diode of the sDMG-256A and IBA CC13 as a function of field size, normalised to the 10 cm × 10 cm field size. For larger field sizes the sDMG-256A overresponds up to 2% at the 20 cm × 20 cm field size, this is constient with other silicon diodes [96].

4.2.7 Small field output factor measurements in the presence of 1.2 T transverse magnetic

The effect of air gap thickness above the silicon chip in the detector packaging for small field output factor measurements in the presence of 1.2 T transverse magnetic field was investigated. The effect of an air gap above the detectors sensitive volume is known to decrease the OF of diodes and has been used to correct for the diodes overresponse to small fields [101]. To investigate if this approach may be feasible in the presence of a magnetic field the change in OF with and without a 1.2T transverse magnetic field was measured. The magnetic field is generated using MARDOS (outlined in Chapter 3) shown in Fig 4.10. A cone gap of 30 mm was used to produce a 1.2T magnetic field. A bespoke phantom was required to position the detector array in the gap between the cones of the permanent magnet and to allow

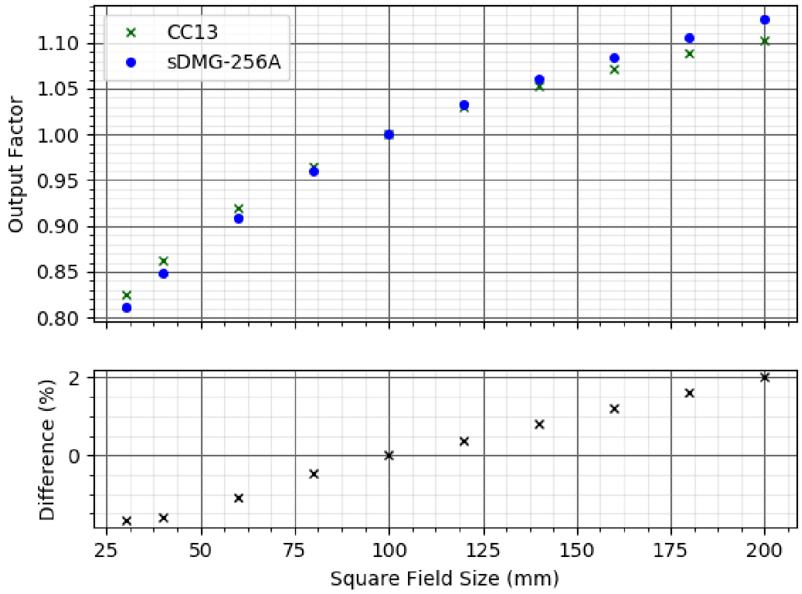

Figure 4.8: OFs measured by the sDMG-256A and IBA CC13 ionisation chambers for a 6 MV beam for field sizes from 30 mm side square field to 200 mm side square field, normalized to 100 mm side square field. Percentage differences are shown in the lower panel.

precise changes to the airgap above the diodes. Measurements are performed at an extended SSD as the magnetic apparatus does not physically fit closer to the linac source, this extended distance also allows the fringe field of the magnet to drop below expected background levels at the head of the linear accelerator as not to affect the linear accelerator operation. Measurements were taken at 150 cm source to detector distance for nominal square field sizes (defined at the 100cm isocentre) of 3 mm^2, 5 mm^2, 10 mm^2 and 15 mm^2 and air gaps of 0 mm, 0.36 mm, 0.72 mm and 1.08 mm. The field sizes were chosen such that the beam only passes though the solid water phantom and detector, avoiding the steel cone tips resulting in only small fields being a physical option. Reproducing the setup without the magnetic field is achieved by an aluminium jig used to support the steel magnetic flux focusing cones, the detector and the phantom in the same geometry as MARDOS, reproducing the scatter conditions of MARDOS, in order to isolate magnetic field effects on the detectors response. The field size and SID constraints limit the scope of the measurements to investigating the relative effect of the magnetic field and air gap on OF, the OF for the case of B=0 may not reflect the dose to water.

Comparing the OF for a range of air gaps and field sizes it is observed as shown in Fig 4.9 that an increase in air gap width results in a decrease in measured OF in a transverse magnetic field with the effect being larger for smaller field sizes compared to the B = 0 T case. This implies that the method used by Shukaili et al

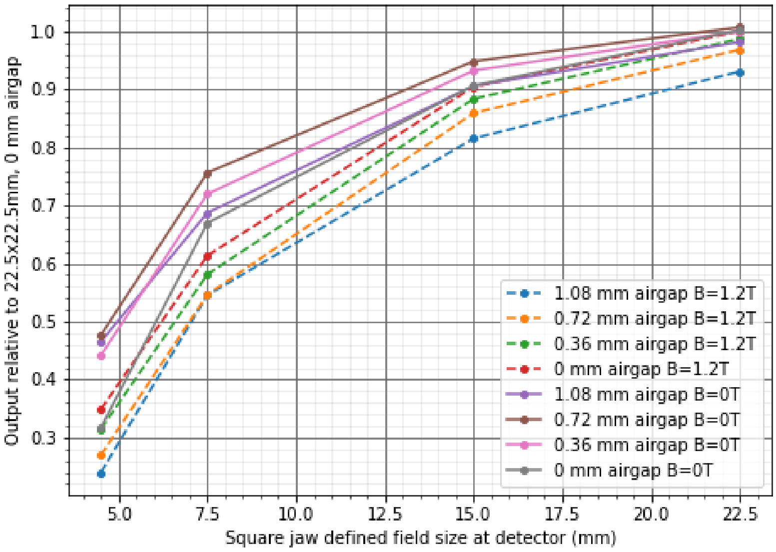

Figure 4.9: Effect of air gap above detector on small field output factor measurement (solid lines – B = 0 T, dashed lines – B = 1.2 T).

of compensating the over response of diodes to small field OF's by using a air gap above the diodes cannot be translated into an MRI-linac environment [101]. This decreased response in the presence of a transverse magnetic field is due to ERE of secondary electrons within the air gap above the silicon diodes.

4.2.8 Small field beam profiles

Beam profiles were measured using sDMG-256A and EBT3 film using a Varian 2100iX linear accelerator (Varian Medical Systems, Palo Alto, CA). Beam energy was 6 MV, with the detector at depth 10 cm in a solid water phantom positioned at 100 cm SSD. The detector packaging used for the small field beam profiles is shown in Fig 4.2. The EBT3 Gafchromic films were scanned with an EPSON expression 10000XL using a 48-bit RGB with a resolution of 72 dpi. All films were pre- and post- scanned six times, discarding the first three scans and using the red channel of the last three scans to calculate optical density. Constant orientation of the film was maintained for pre and post scans. The data for the calibration curve was collected at the same time as the beam profiles, 10 dose points were fit with a third order polynomial to convert optical density to dose. Field sizes from 5 mm^2 to 40 mm^2 were measured, comparisons of measured profiles are shown in figures 4.11 - 4.13. In the figures, profiles were aligned so that the origin lies at the beam central axis. The Full width at Half Maximum (FWHM) and 80-20% penumbral widths (mm) for the cross-plane profiles are shown in Table 4.1. The FWHM values measured with the sDMG-256A were within 0.4 mm of the EBT3 determined values for all measured

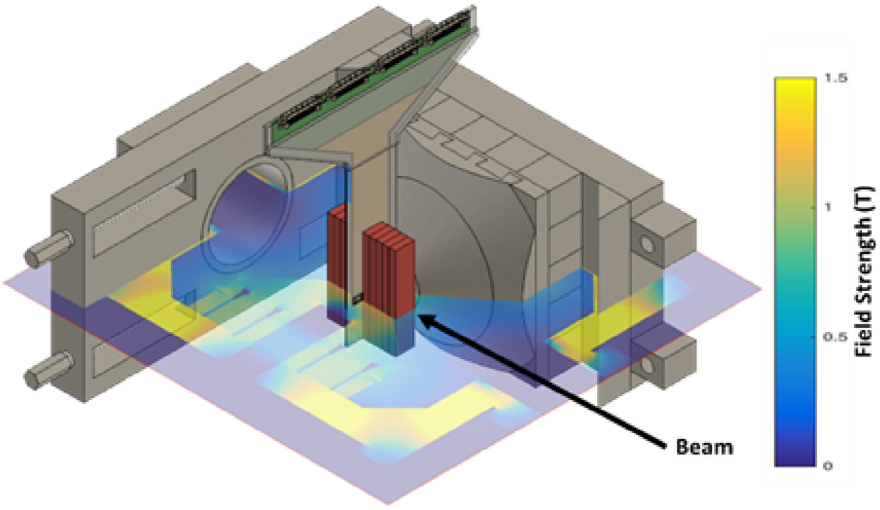

Figure 4.10: MARDOS magnet (only half the magnet is displayed) with sDMG-256A and indicated beam direction for measurements investgating the effect of air gap above the detector on output factor.

Field size	sDMG-256A		EBT3 Film		Difference	
	FWHM	Penumbra	FWHM	Penumbra	FWHM	Penumbra
11	12.2	3.8	12.29	3.69	0.09	0.11
13.2	14.4	3.8	14.7	3.71	0.3	0.09
16.5	17.8	4	18	3.6	0.2	0.4
22	22.8	4.2	22.7	3.6	0.1	0.6
27.5	28	4.2	28.4	3.7	0.4	0.5
33	33.4	4	33.5	3.6	0.1	0.4

Table 4.1: FWHM (mm) and 80-20% penumbral widths (mm) for profiles measured in solid water, the nominal field size (mm) represents the field size at the detector plane (110 cm SAD).

field sizes. The penumbra measurements with the sDMG-256A were within 0.6 mm compared to EBT3 film.

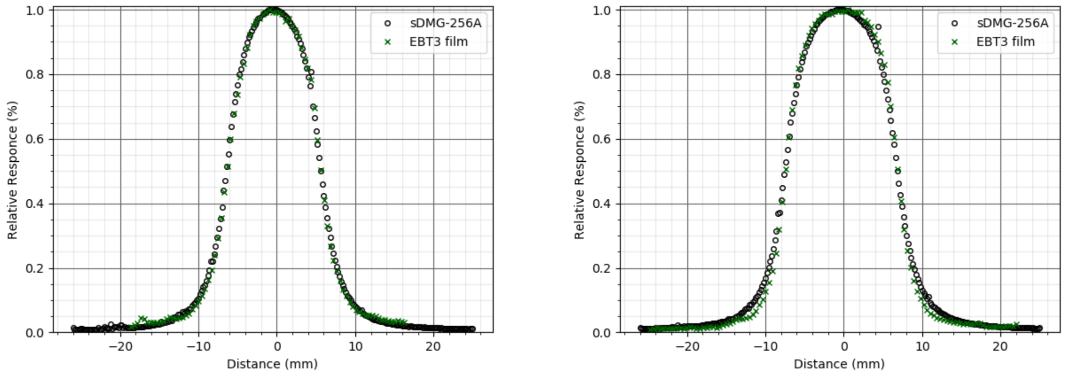

(a) **(b)**

Figure 4.11: 6MV crossline jaw defined dose profiles measured with sDMG-256A and EBT3 (a) 10x10 mm (b) 12x12 mm.

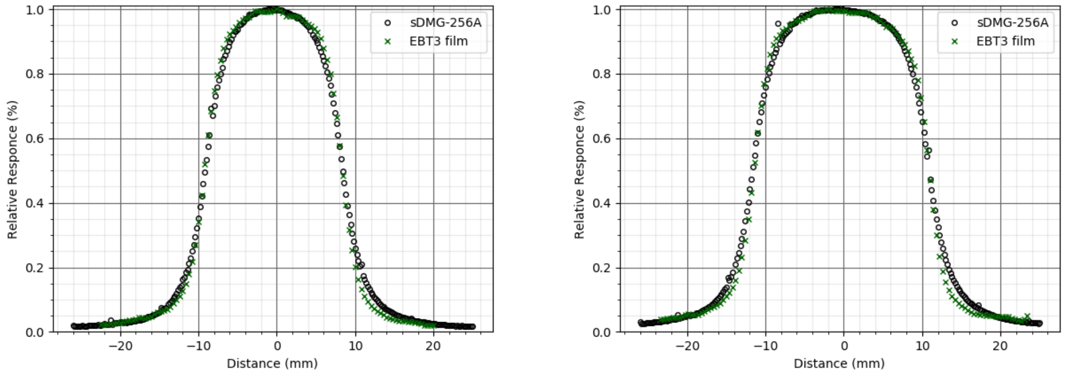

(a) **(b)**

Figure 4.12: 6MV crossline jaw defined dose profiles measured with sDMG-256A and EBT3 (a) 15x15 mm (b) 20x20 mm.

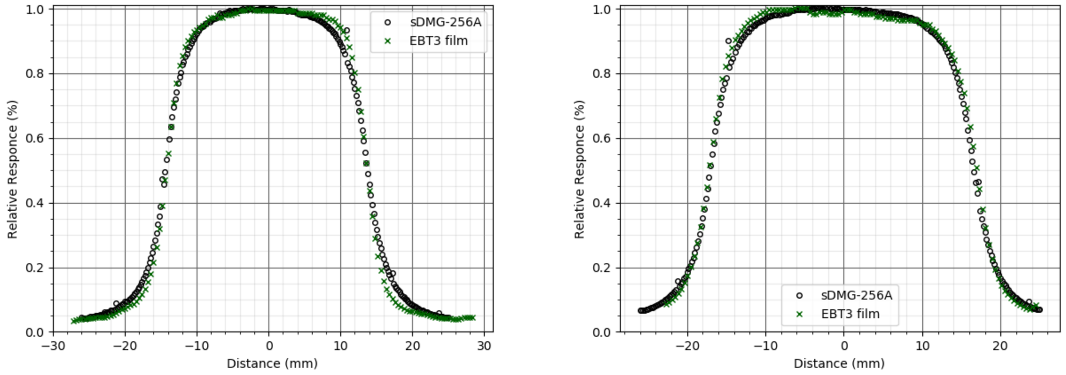

(a) **(b)**

Figure 4.13: 6MV crossline jaw defined dose profiles measured with sDMG-256A and EBT3 (a) 25x25 mm (b) 30x30 mm.

4.3 Conclusion

The preliminary dosimetric characterisation including dose linearity, DPP, angular dependance, uniformity of detector channel response and PDD of a monolithic silicon strip detector mounted to flexible polymide carrier, the sDMG-256A has been carried out. The sDMG-256A over responded relative to a CC13 ionisation chamber by up to 2% for OF measurments for field sizes above 10 cm × 10 cm. The sDMG-256A has been tested with an inline 1.2 T magnetic field, using small fields to investigate if a previously published technique of using a small air gap above the detector to match OFs measured with a 'correction-free' dosimeter for OFs measurements with the monolithic silicon could be used. It was observed that this technique would not work in a magnetic field due to the influence of the ERE. Further work investigating if a suitable detector packaging could ameliorate the effect of the air gap above the dosimeter is being undertaken.

Chapter 5

First application of a high resolution silicon detector for proton beam Bragg peak detection in a 0.95 T magnetic field

The results presented in this chapter have been published in the journal Medical Physics.

Causer, T., Schellhammer, S., Gantz, S., Lühr, A., Hoffmann, A,. Metcalfe, P., Rosenfeld, A., Guatelli, S., Petasecca, M., Oborn, B.M., "First application of a high resolution silicon detector for proton beam Bragg peak detection in a 0.95 T magnetic field" *Medical Physics*, vol. 47, pp 181-189, 2020.

Contributions: Causer T. designed the experiments as well as collected and analysed the data presented in this chapter. Oborn, B.M and Chapman T. assisted with experiments. Metcalfe, P., Rosenfeld, A., Oborn, B.M were involved in planning experiments and supervising the work.

5.1 Overview

Real-time MRI guided x-ray therapy (MRXT) has been operating clinically now since 2014 through the MRIdian system (ViewRay, Oakwood Village, USA) [14, 117]. A second system, the Unity (Elekta, Crawley, UK) has also recently started clinical treatments and at least two 2nd generation prototype systems are under development [17, 19, 24, 107]. Such systems offer superior soft-tissue contrast and information on real-time patient anatomy changes to assist in guiding the x-ray beam radiotherapy.

For proton beam therapy however, daily patient specific image guidance is centred around in-room CT, on-board CBCT or orthogonal kV imaging methods. These methods are typically only used for patient positioning purposes. There is little scope for on-line adaptive replanning to account for any inter-fraction patient anatomy changes such as organ motion or weight gain/loss. Any changes to the plans would likely be performed off-line. Despite the physical advantages of charged particles for cancer treatment, irrefutable demonstration that proton therapy results in lower toxicities than x-ray beam radiotherapy with level 1 evidence has yet to be accomplished [118]. The reason for this could be argued to be caused from suboptimal treatment planning and image guidance for setup correction. This idea is not novel, and so various groups have discussed the concept of real-time MRI-guided proton therapy (MRPT) [41, 43–45, 50, 51]. A detailed overview of the various aspects and future development of this modality is discussed by Oborn et al [50]. One such area of MRPT that will require investigation is proton beam dosimetry in magnetic fields. For proton beam treatment quality assurance, the properties of the proton beams are required to be characterised using techniques such as water tanks with ion chambers and peak-finder detector systems. In an MRPT environment the proton beam is now subject to external magnetic fields and so there is beam deflection via the Lorentz force, and so the detector system must be magnetically compatible. Further to this, the patient/phantom will be inside the bore or gap of an MRI system and so the detector system needs to be small enough to physically fit inside this region. Hence there are new challenges which need to be addressed to ensure that dosimetry for MRPT will be accurate.

In this chapter, we present for the first time the experimental application of a novel high-resolution silicon strip detector array in the presence of a strong magnetic field of 0.95 T for Bragg-peak detection. Proton pencil beams of clinical energy and size were used and the changes induced by the magnetic field to the Bragg-peaks were mapped out accordingly.

5.2 Materials and methods

5.2.1 Real-time high-resolution detector system

The “DUO” detector [see Fig. 5.1(a)] is a unique monolithic silicon diode array developed at the Centre for Medical Radiation Physics (CMRP), University of Wollongong Australia. It comprises of 505 n+ silicon strips positioned in an orthogonal cross-hair arrangement on a p-type silicon wafer. The detector pitch is 0.2 mm and the sensitive area of each diode is 20 µm × 800 µm, with the depth of the sensitive n+ strips being 37 µm [see Fig. 1(b)]. The silicon diode array is wire-bonded to a printed circuit board (PCB) of 300 um thickness that provides connection to the data acquisition system (DAQ). Both the silicon diode array and wire bonds are coated in a 0.3 mm thick protective layer of resin. The DAQ has been developed in house and is based around the AFE0064 multichannel electrometer chip (Texas Instruments). To read out the 505 channels, 4 analog-to-digital converters are used with 8 AFE0064's all synchronised by field programmable gate array (FPGA) [119]. The data is passed from the FPGA to a laptop computer via USB2.0 and accessed with an in-house developed graphical user interface written in C++. A specially designed (PMMA) phantom was used in this experiment to position the detector array centrally within the magnetic field of the permanent magnet device and allow interchangeability of various thickness PMMA absorbers as shown in Fig. 5.1(a).

5.2.2 Research proton beamline

The proton therapy facility in Dresden has a clinical proton beamline with a single treatment room equipped with a 360^o rotating gantry and a dedicated research bunker with a fixed horizontal proton beamline. The system is driven by an IBA C230 (IBA Proton Therapy, Louvain-La-Neuve, Belgium) isochronous cyclotron with a maximum proton energy of 230 MeV. Beam energies between 70 MeV and 230 MeV can be provided to both the clinical bunker and the research beamline. For practical reasons, it is not a strict requirement for the proton beam in the research beamline to have a symmetrical beam profile with small spot size for all energies. Instead the beam is typically mostly symmetrical but has a spot size in the order of 20-30 mm FWHM. For experiments where small beams are required, simple brass collimators are used to produce such beams. Fig. 5.1(d) displays an image of the research beamline used in our experiments. The proton beam exits the beam pipe through a through an aluminium vacuum window, and is then shaped prior to reaching the experimental setup using two 5 cm thick brass apertures, both of which have a central 10 mm diameter hole to allow the beam to pass through. The choice of a 10 mm collimated pencil beam is designed to emulate a typical spot size for a pencil beam scanning system. Three energies were selected for the measurements; 90 MeV, 109 MeV, and 125 MeV. The choice of energy was ultimately governed by the phantom dimensions, see Section 5.2.3.

5.2.3 Experimental measurement setup

The DUO detector and phantom were position 30 cm downstream of the brass collimators [see Fig. 5.1(c)]. For the B = 0 T experiments, the phantom was supported from a nearby table by a custom made Aluminium frame with 2 support arms. This frame allowed for unobstructed addition or removal of the permanent magnet dipole system. The permanent dipole magnet consists of a C-shaped iron yoke and two banks of NdFeB magnets producing a transverse magnetic field of 0.95 T in the central gap. The magnetic field shown in Fig. 5.1(e), is greater than 0.5 T in all regions of the volume between the two magnet banks [87]. The faces of the magnet poles are 150 mm × 200 mm and are separated by a 40 mm gap. The PMMA phantom was designed to position the DUO detector at the centre of the magnetic field with the axes' of the diode array perpendicular and parallel to the beam central axis. The detector and phantom were suspended laterally from a separate table to the one the magnet was mounted on, as shown in Fig. 5.1(c), allowing measurements to be repeated without the magnet in place. Three beam energies were selected (90 MeV, 109 MeV, and 125 MeV), in order to investigate any potential magnetic field induced effects on altering the lateral scatter of protons that take longer paths before stopping. These energies were selected, in combination with additional 10 mm thick slabs of PMMA on the phantom entrance to deliberately cause the Bragg peak to fall in alignment with the detector cross-hairs. For the 90 MeV experiments no additional PMMA slabs were used. While for the 109 MeV beam 20 mm was added, and for 125 MeV 40 mm of PMMA was added to the entry side of the detector phantom. The additional PMMA essentially acts to reduce the beam energy down to 90 MeV, the same energy as the setup without additional PMMA.

5.2.4 Data processing

The experimental prototype detector system contains a small number of both dead channels and channels with erroneous signal fluctuations due to manufacturing/wire bonding imperfections. These channels were identified via either a zero response or a response more than 50% different to the neighbouring channels when exposed to a calibration flood field. These channels were less than 1 in 50 and are removed from the results. To account for small differences in the sensitivity of each channel, a measurement of a uniform radiation field was used to calculate an equalization vector as described by Wong et al [89]. A subtraction of background signal is performed for each channel for every measurement and is sampled prior to each measurement. Dose profiles were normalized with respect to the maximum response in the depth axis.

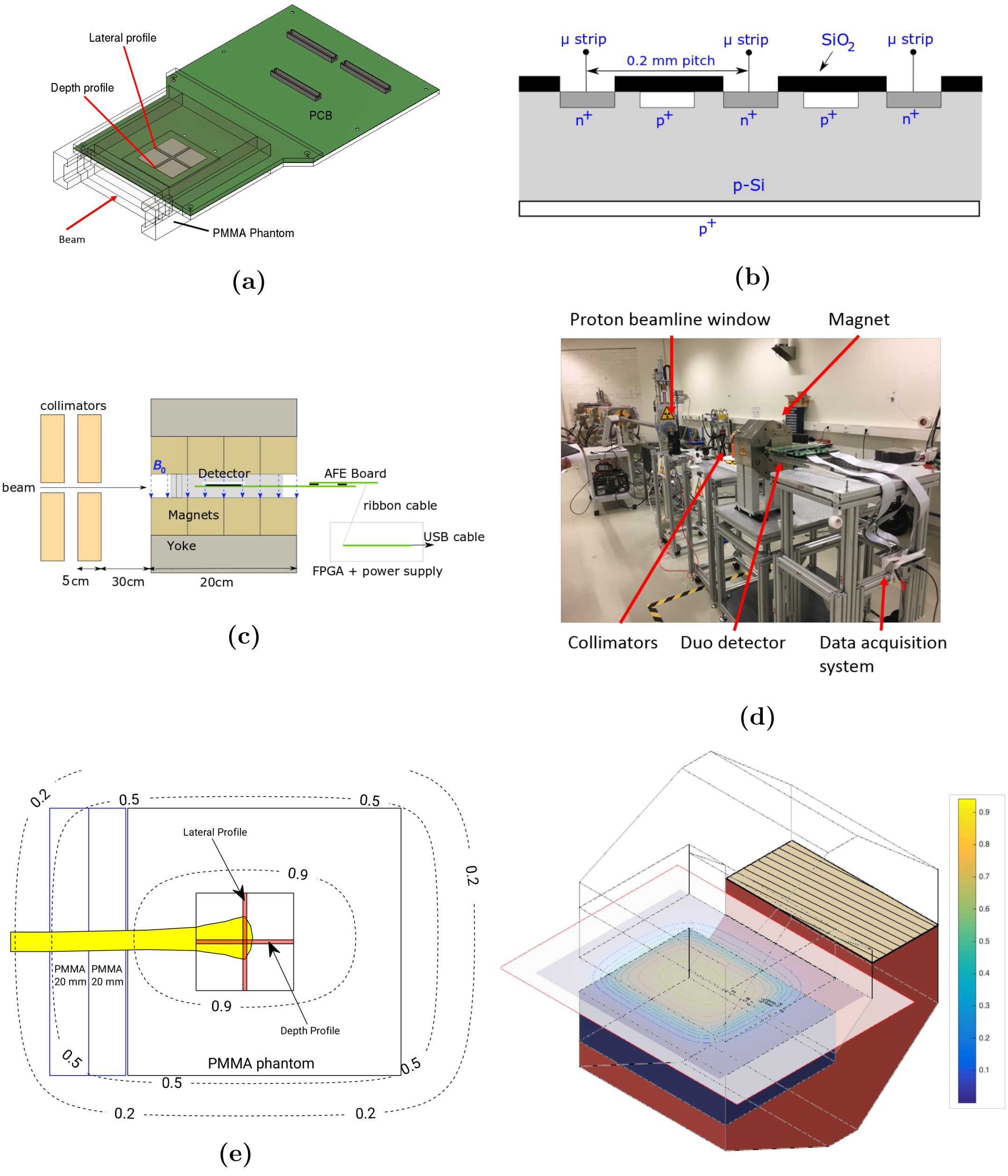

(a) (b) (c) (d) (e) (f)

Figure 5.1: An overview of the DUO detector and experimental setup. (a) A schematic diagram of the DUO detector and surrounding PMMA phantom. (b) A sectional view through a detector profile detailing the sensitive n+ zones spaced by 0.2 mm. (c) A schematic diagram of the experimental layout showing the detector system, magnet, phantom and collimators. (d) Photo of the actual experimental setup in fixed horizontal proton beamline. (e) A sectional top view of the detector and phantom showing the extent of the magnetic field in T. (f) A sectioned view of magnet showing the magnitude of magnetic field (T) from the COMSOL model at the central plane between the NdFeB magnet banks.

5.2.5 Monte Carlo simulation

A Geant4 Monte Carlo simulation was developed, modelling accurately the set-up of the experiment, with the aim of achieving a better understanding of the experimental results. Geant4 version 10.2.p02 was used, and the particle transport was simulated by using a Physics List that was derived from the Hadrontherapy advanced example of Geant4. The Geant4 Binary Cascade (BIC) model was used to model inelastic hadronic interactions of protons, neutrons and nuclear recoils. The elastic hadronic scattering (G4HadronElasticPhysicsHP), radioactive decay and photo-nuclear interactions were modelled as well. The HP data libraries were used to describe more accurately neutron interactions below 20 MeV. The models are described in detail in Allison etal [120]. The detector was modelled accurately according the engineering drawings and included the key elements such as PCB, PMMA phantom, silicon chip, resin coating on silicon and air gaps around silicon. Dose was scored using two methods, (1) over the entire detector and phantom geometry at 1 mm^3 resolution, and (2) inside the active volume of the silicon chip at 10 µm × 1 mm × 1 mm where the depth into silicon is the first dimension of 10 µm. To model the magnetic field, a 3D look-up-table (LUT) containing the magnetic field values was read into the simulation. The LUT was created from a COMSOL 3D finite element model of the C-shaped permanent magnet device. The COMSOL model matched the measured central plane magnetic field of 0.95 T and was within +/- 2% over the entire plane between the magnet pole faces (40×40 cm area) [87]. For the proton beam model, a generic parallel monoenergetic beam of 50 mm diameter was incident on the 10 mm brass collimator. The beam energies were matched to the nominal beamline energies of 90 MeV, 109 MeV, and 125 MeV. As the primary purpose of the Monte Carlo simulation was to aid in interpretation of the experimental results, a fully benchmarked beamline model was therefore not used or warranted for the present study.

5.3 Results

5.3.1 Experimental measurements

Figs. 5.2-5.4 display the results obtained for the simultaneous measurement of the lateral profile and depth profile for both in the presence of a 0.95 T magnetic field and the 0 T case. The nominal beam energies of 90 MeV, 109 MeV and 125 MeV were used in combination with additional PMMA build-up, as described previously, to generate a Bragg peak at the detector cross-hair location. In each of the Figs. 5.2-5.4, the left images, part (a) and (c), display a graphical color-mapped representation of how the dose was presented on the GUI display of the detector system in real-time.

The 2 orthogonal active detector strips are also outlined, as well as the direction that the beam was incident from. Parts (b) and (d) display a comparison of the depth and lateral profiles respectively. The uncertainty in the positioning of the detector array between measurements was estimated to be ± 0.5 mm. This was based on the accuracy of an externally mounted laser system that defined the isocentre of the magnet assembly and beam line axis. This detector/phantom was essentially aligned to the laser lines

Depth Dose Profiles

The nominal Bragg peak is clearly identified as the primary peak in the B = 0 T profile in part (b) of each Fig. (5.2-5.4). When the magnetic field is applied, the central (and highest dose) section of the pencil beam and Bragg peak is no longer completely captured along the depth profile as it is slightly deflected laterally. This is evident in the lateral profiles as a lateral shift for the B = 0.95 T cases (see next section). Also evident in the depth dose profiles are multiple smaller peaks as well as the primary Bragg peak. These multiple peaks are in fact Bragg peaks from protons that have traveled in different paths from the bulk of the protons in the beam. This is attributed to the silicon detector being embedded in a phantom with multiple materials in the beam path. Unfortunately, and due to mechanical warping after construction, the PMMA phantom enclosure for the detector also contained a small air gap along the same plane as the detector and parallel to the proton beam. Further to this, a small air-gap existed above the silicon. The other materials present are a 0.3 mm thick layer of PCB which the silicon array is mounted on, and the 0.47 mm thick silicon detector itself. The overall result of transporting protons through the mixed mediums gives rise to the complex depth profiles observed. Merchant etal however, successfully used these multiple Bragg peaks observed from a similar edge-on measurement of proton beams using a similar monolithic silicon detector for range verification [73]. The main identifiable peaks are labeled in part (b) of each figure. These include:

1. PMMA + Silicon Bragg Peak: Protons which travel through primarily the PMMA build-up, then through some of the silicon array base cause this Bragg peak.
2. PMMA + Silicon + PCB SOBP: This is a somewhat spread-out Bragg peak (SOBP) originating from a combination of paths which include significant transport through the PCB layer (denser than PMMA).
3. Pure Silicon BP: Some protons were able to travel through the air-gap and directly reach the silicon array before energy loss. In the cases of the 109 MeV and 125 MeV experiments, these beams were reduced in energy by the additional PMMA slabs to around 90 MeV before reaching the detector phantom. At this point some

protons were able to travel through the small air gap down to the silicon.

As the proton beam is attenuated in a complex manner, it is therefore impossible to draw any concrete dosimetry values from these profiles. Instead, the value comes from the spatial information regarding the positions of the Bragg peaks. With an improved detector phantom design, for example no air-gaps present, the depth dose profiles would display much more clear Bragg peak information without the long dose tail.

Lateral Dose Profiles

As can be seen in parts (d) of each of the Figs. 5.2-5.4, overall the lateral dose profiles depict a consistent 2 mm lateral deflection of the proton beams at the level of the Bragg peak (or magnet centre) for each energy. The deflection was calculated by simple examination of the shift in the FWHM of each of the lateral profiles, B = 0 T and B = 0.95 T for each beam energy. This consistency is expected as the different energy proton beams undergo a similar magnetic deflection process. For the case of the 90 MeV beam, protons travel mostly undeflected until they reach the phantom edge which is around 60 mm before the magnet centre. At this position the magnetic field has ramped up to 0.95 T and the Lorentz deflection force is consistent from that depth onwards. For the other energies, the beam is transmitted through either 20 mm (109 MeV) or 40 mm (125 MeV) of extra PMMA before reaching the phantom edge. This reduces these two beam energies down to around 90 MeV as they enter the phantom, or magnetic deflection volume. Thus all lateral profiles will inherently display a similar lateral beam deflection amount.

The lateral beam profile shapes (without magnetic field) are also observed to be energy dependent and not perfectly symmetrical. As described in the methods section, the research beamline is not strictly a spatially symmetrical beam. Even over the central 10 mm of collimated beam, the profile can be non-symmetrical. The high resolution lateral profile of the DUO detector system has indeed shown this result, for example consider the 109 MeV result at B = 0 T [see Fig. 5.3(d)]. When the magnetic field is introduced, the profiles may change in an even more complex manner. In this case, the path of the protons will deflect laterally by the Lorentz force as expected, but there is clear changes to the way they travel through the complex phantom geometry and small air gaps. For example, there will be a very small change in the direction vectors of each proton as they reach the edge of the PMMA phantom (60 mm before magnet centre). At that point they then may take different average paths (as compared to B = 0 T) before stopping near the cross-

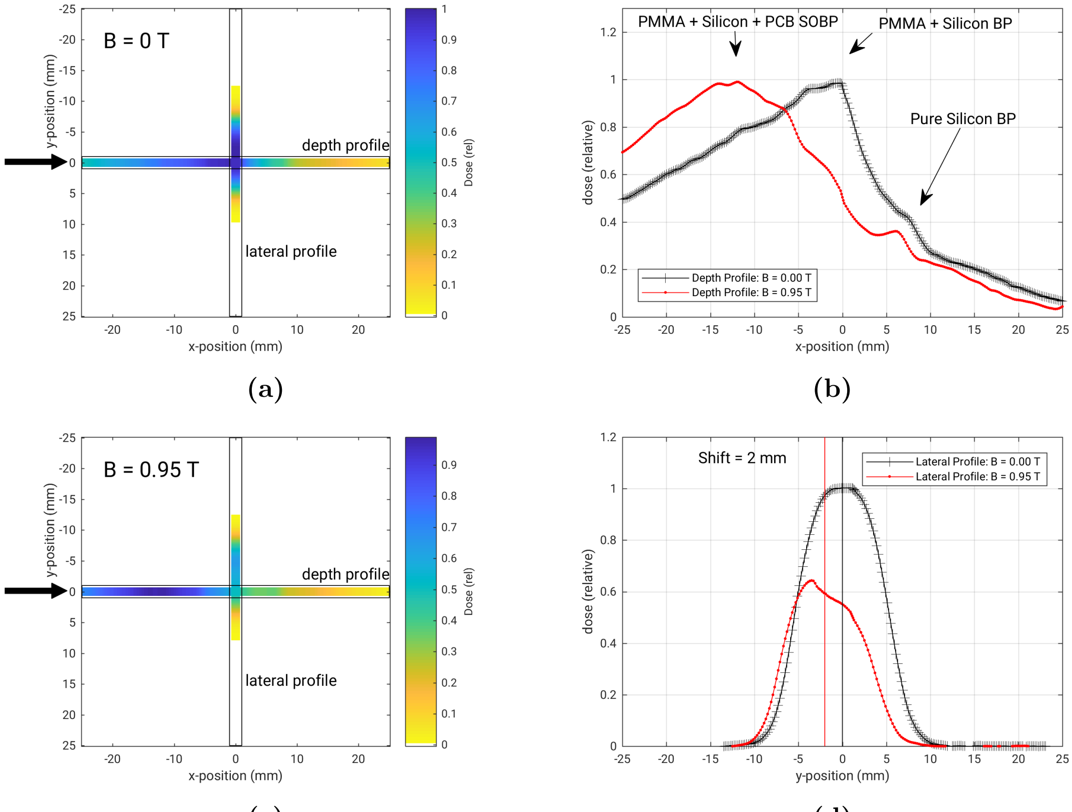

(a) **(b)**

(c) **(d)**

Figure 5.2: Results for the 90 MeV proton beam measurements. (a) Diagram of the detector reading with the scoring profiles shown for the B = 0 T case. (b) The depth dose profiles for both the B = 0.95 T and 0 T case. (c) Detector display for the B = 0.95 T case. (d) Lateral dose profile displays for both B = 0 T and B = 0.95 T cases.

hair of the DUO detector in the silicon, in particular how much of their path is through the air-gaps. Similar to the depth-dose profile data in the previous section, an improved detector phantom design would lead to greater confidence in drawing out true dosimetry values from the profile data.

A further dosimetric consideration is the potential for a change in the detector's response when measuring the magnetically deflected beams, i.e. if the detector has some non uniform angular response. This arises from the protons crossing the detector strips at some small angle rather than being perpendicular to the lateral strip (lateral profile) and parallel to the longitudinal strip (depth profile) as is the case for no deflection. In the current experimental setup we predict and observe a lateral deflection that is very small (≈2 mm) considering the overall proton path length taken in the magnetic field volume (≈100 mm). Simple trigonometry tells us this is about a 1 degree change in the proton trajectory and so no measurable response changes would be expected. Future potential clinical applications, where protons may be in

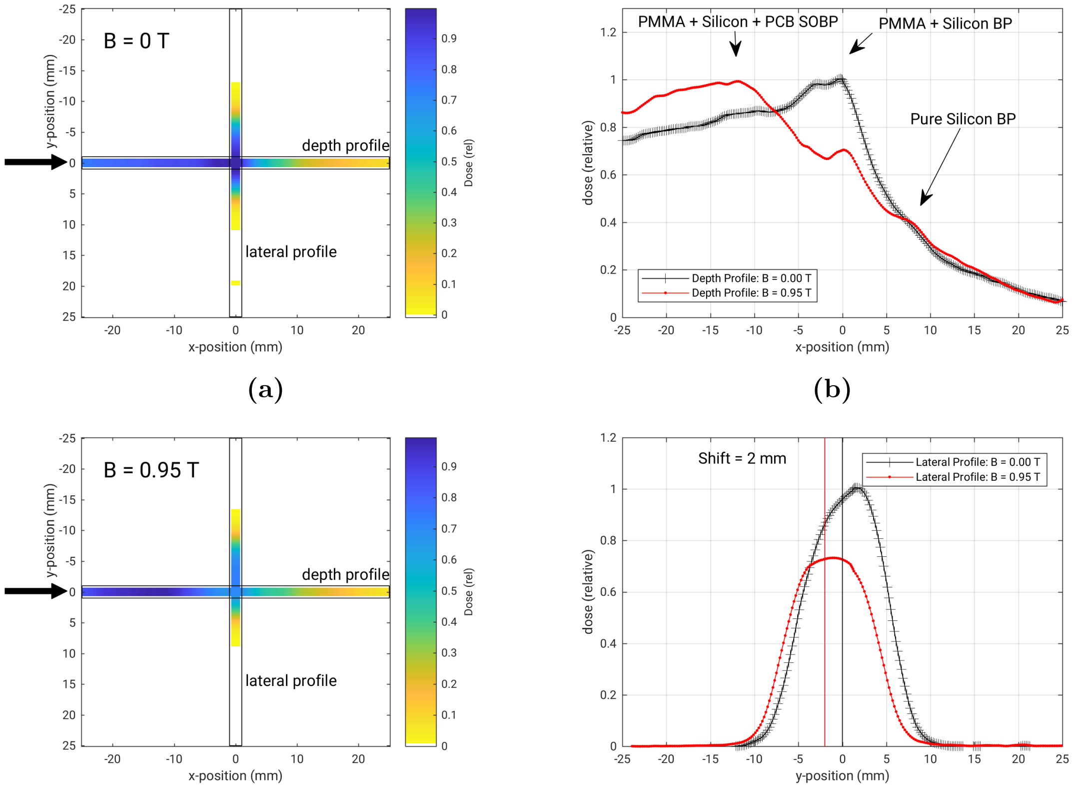

(a) **(b)**

(c) **(d)**

Figure 5.3: Results for the 109 MeV proton beam measurements. (a) Diagram of the detector reading with the scoring profiles shown for the B = 0 T case. (b) The depth dose profiles for both the B = 0.95 T and 0 T case. (c) Detector display for the B = 0.95 T case. (d) Lateral dose profile displays for both B = 0 T and B = 0.95 T cases.

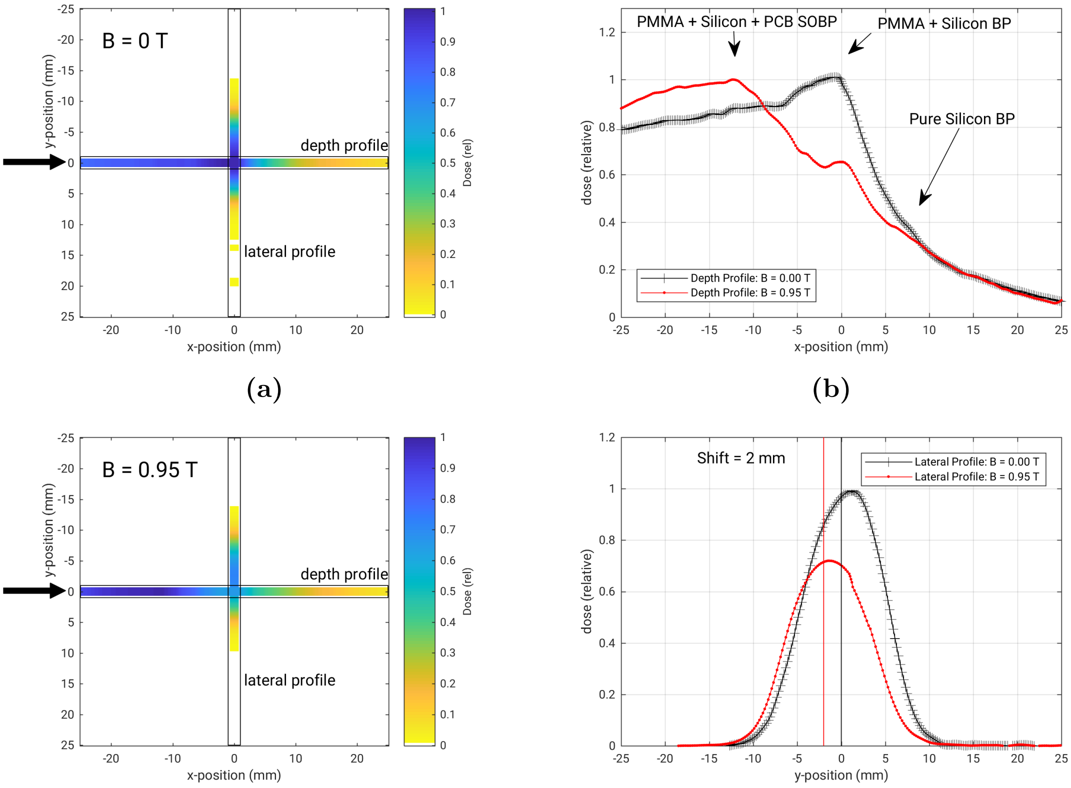

(a) (b)

(c) (d)

Figure 5.4: Results for the 125 MeV proton beam measurements. (a) Diagram of the detector reading with the scoring profiles shown for the B = 0 T case. (b) The depth dose profiles for both the B = 0.95 T and 0 T case. (c) Detector display for the B = 0.95 T case. (d) Lateral dose profile displays for both B = 0 T and B = 0.95 T cases.

stronger magnetic fields, and travel longer distances, would certainly result in more proton beam deflection. This would lead to protons arriving at the detector from both polar and azimuthal angles. The angular response of any detectors measuring this scenario would obviously need full characterisation in 3D.

As a final comment on the dosimetry performance of the detector system we note the recent work published by Lühr et al [88] describing a small but measurable proton beam induced electron return effect (ERE). In our experiments we are not examining or subject to the classical ERE or dose changes that occurs on the exit side of a phantom [16, 25, 30, 31], but there will be indeed some spiralling of very low energy secondary electrons present in the air-gap above the silicon array. These could be magnetically encouraged to return to (or travel towards) the silicon chip causing an over response. However the silicon chip is covered with a resin of average thickness of 0.3 mm. The previous work of Lühr et al describes a 2.2% increase in dose at 1 T due to the proton beam ERE on the exit side of a phantom using EBT3 film measurements at a depth of 0.156 mm. For our detector with a 0.3 mm resin protective layer we expect almost no penetration of these very low energy electrons to generate an over response. In any case, as described in the previous sections, the air-gap above our current silicon detector is not required and attempts are being made to eliminate this volume.

5.3.2 Monte Carlo Modeling

As outlined in the methods section, the Monte Carlo simulation is designed to aid in the interpretation of the experimental results. Without a fully benchmarked beamline model and complete knowledge of the magnitude of the air-gaps within the phantom at every location, expecting to achieve a match to experiments is almost impossible. This is typical of modeling particle beams with finite range such as protons. Fig. 5.5(a) shows the most important finding of the Monte Carlo simulations. A diagram of the dose distribution on a sectional view through the DUO detector and phantom used in the experiment from the Monte Carlo simulation for a 90 MeV proton beam. The immediate observation is the lack of a pristine and distinctly defined Bragg peak. The air gaps in the detector phantom have allowed protons to travel with minimal energy loss to the level of the silicon in the phantom. These protons then stop over various ranges depending on how they travel through the silicon and air gap. The result, as clearly also depicted in the experimental data is the presence of the long dose tail in the depth-dose profiles. Further examination of the 90 MeV simulation is presented in Fig. 5.55(b). This is a zoomed section from part (a) surrounding the silicon array. All the phantom

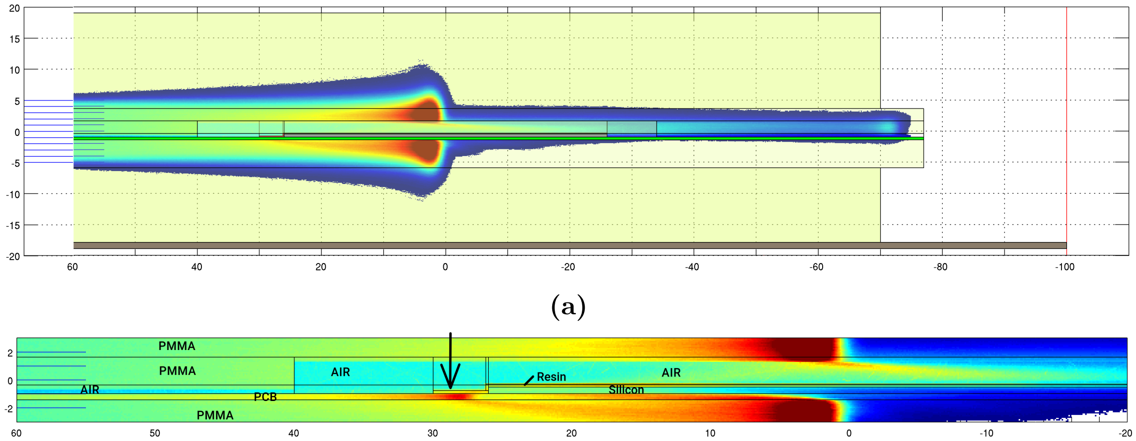

(a)

(b)

Figure 5.5: Monte Carlo calculated dose distribution on a sectional view through the DUO detector and phantom used in the experiment for a 90 MeV proton beam. Part (a) shows how the pencil beam stops in a complicated manner throughout the detector phantom with its multiple components of different materials. (b) shows a zoomed region around the nominal Bragg peak location. The arrow indicates a Bragg peak generated by protons that traveled almost entirely through the PCB of the detector base. Units are mm.

materials are listed, and the dose hot spots at various locations depict multiple Bragg peaks occurring in the phantom components. These Bragg peaks can all be traced to corresponding common paths taken by the protons in the beam. An interesting example is the Bragg peak shown in the PCB which occurs 30 mm from the phantom edge (as indicated by the arrow in Fig. 5.6(b)). This represents protons that have traveled entirely through through the PCB with higher density (than PMMA), and so they stop first. Careful examination of the various possible proton paths has been performed, and this has led us to the conclusions described in the previous section regarding the reason for the various small peaks along the depth-dose profile in the experimental data. For the proton beam lateral deflection the ~2 mm deflection was observed, similar to the previous studies [87].

5.4 Conclusion

This study has presented the first application of a novel high spatial resolution real-time silicon based detector system for use in detecting the Bragg peak of proton pencil beams, in particular within a transverse magnetic field of 0.95 T. The device also appears to correctly map out the changes induced by a 0.95 T transverse magnetic field to proton pencil beams, namely the gross lateral deflection. The Monte Carlo simulation study was critical to understanding the detector response observed in the depth profiles. Future efforts will be directed towards improving the detector packaging to reduce the Bragg peaks caused by the proton paths through different combinations of detector packaging materials. For example, removal of the air gap around the detector using a suitable gel material is under investigation. A successful phantom design will open up the opportunity to conduct further targeted research into the unique dosimetry requirements anticipated in future efforts towards MRI-guided proton therapy.

Chapter 6

Development of a device for imaging, radiation and optical isocentre determination on the Australian MRI-Linac

This chapter contains results that have been published in the Journal of Physics: Conference Series.

Causer, T., Alnaghy, SJ., Alnaghy, S., Roberts, N., Petasecca, M., Rosenfeld, A., Metcalfe, P., Oborn, B.M., "Imaging and radiation isocentre determination for inline MR-guided radiotherapy systems- proof of principle using MR-phantom with embedded monolithic silicon detector" *Journal of Physics: Conference Series*, no. 1662 012008, 2020.

Contributions: Causer T. performed the measurements, analyzed the data, and wrote the manuscript with support from all the authors. Alnaghy S,J., Alnaghy S., Roberts, N., Oborn, B.M and Petasecca M. assisted with the experimental work. Dong B. operated the Australian MRI Linac for the distortion measurements presented. Metcalfe, P., Rosenfeld, A., Oborn, B.M were involved in planning experiments and supervising the work. Causer T. designed the Isocentre phantoms and the University of Wollongong engineering workshop constructed the phantoms used in the experimental measurements. The operation of the Unity MRI Linac was performed by Jameson, M.

6.1 Introduction

Multiple vendors are now offering real-time MRI-guided radiotherapy systems. The MRIdian (ViewRay) and Unity (Elekta) are both systems where the magnetic field is perpendicular to the radiation beam [14, 17]. The Australian MRI-linac and Aurora-RT (MagnetTx) prototypes both have the magnetic field orientated parallel to the radiation beam [19, 107]. The alignment of the imaging and radiation isocenter is an essential component of linac commissioning and ongoing QA, as any geometrical offset between them results in a population wide geometrical error for all image-guided treatments on that machine. This proves to be difficult to verify in MR-linac systems. The widely used Winston-Lutz method (WL) typically uses an MV imaging panel that is not available on all commercial MR-linacs. Additionally, in MR-linac systems where the magnetic field is perpendicular to the radiation beam, the presence of the static magnetic field alters the electron trajectory. This causes asymmetry in the dose kernel which can hinder accurate geometrical QA-tests that rely on beam profiles such as a star shot to measure the radiation isocenter [121] . Van Zijp et al demonstrated the use of electron dense materials to minimise the magnetic field effect in MR-linac specific QA, showing that 2-3 mm thick copper plates were sufficient to reduce the electron path length in order to perform accurate geometrical QA-tests in a 1.5 T magnetic field [122]. The MRIdian supplied procedure for MR-MV isocentre coincidence measurement uses 2 pieces of radiochromic film and a proprietary cylindrical daily quality assurance (DQA) acrylic phantom [123]. The Elekta Unity supplied method of performing the MV beam to MR Imaging isocentre coincidence check uses zirconium balls surrounded by MR visible fluid to determine the alignment between the MR and MV coordinate systems, the Position of the MV beam is based on projections of the zirconium balls imaged using the Unitys on-board MV imaging panel implying the MV beam location is being determine from fluence [124]. The magnetic field has little influence on the MV Imaging panel of the Unity, by design the active coil shielding creates a region of low magnetic field where both the linac head and MV Imaging panel operate [125]. Latifi et al demonstrated a method of MR-MV isocentre characterisation on a MRIdian system using Suncorp IC ProfilerMR and reported a gantry angle dependant MR isocentre offset [126]. Dorsch et al has presented a phantom design that uses fiducial markers to determine the phantom positioning relative to the imaging isocentre and polymer gel with a star shot measurement to measure the radiation isocentre location [127]. In this chapter, the authors describe the design and feasibility testing of a device that combines a high resolution monolithic silicon detector with an MRI visible phantom for characterisation of optical, MR imaging and radiation isocentre for inline MR-guided radiotherapy systems.

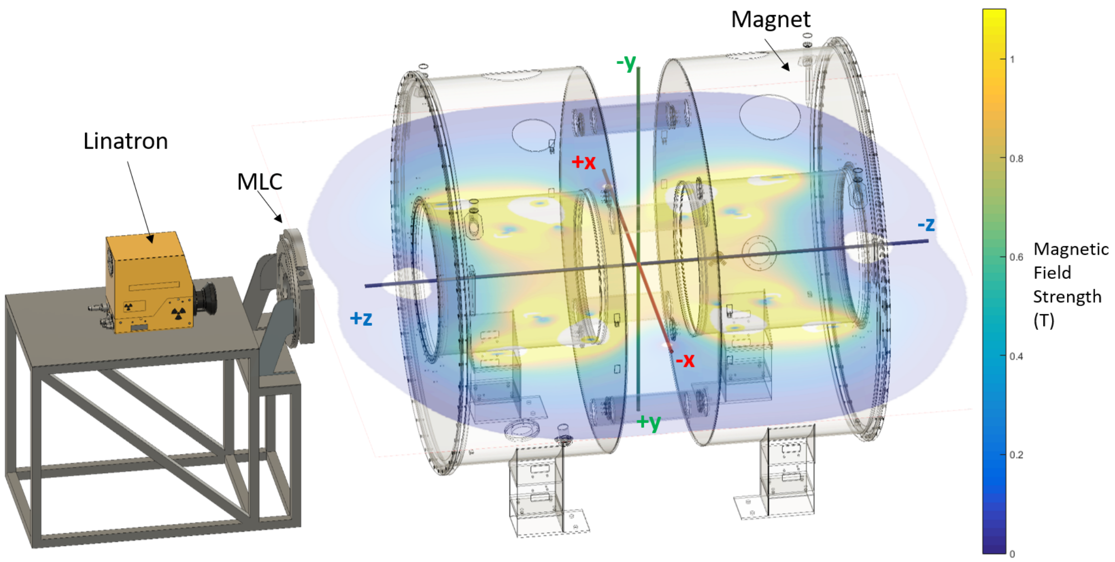

Figure 6.1: Visualisation of Australian MRI Linac with magnetic field strength and coordinate system originating at the systems isocentre

6.1.1 The Australian MRI-Linac

The Australian MRI-Linac uses a Linatron-MP (Varex, USA) linear accelerator radiation source that generates two nominal flattening filter free beam energies, 4 MV and 6 MV [20]. The Linatron is mounted to a stainless steel table that is mounted on a pair of linear guide rails used to adjust the source-to-isocenter distance (SID) from 1.8 to 3.2 m. There are eight fixed docking points on the linear rail system to allow reproducible SID setups. A clinical Millennium 120 leaf (Varian Medical Systems, Palo Alta, CA) multileaf collimator (MLC) is also mounted to the table, this maintains a constant source to collimator distance. The system does not have a secondary collimation system. The MLC is fixed, does not rotate and the leaves travel horrizontally in the x-axis shown in Fig 6.1.

The MRI system uses a 1.0 T bespoke split bore magnet (Agilent, UK). The bore diameter is 62 cm and the gap in the magnet is 50 cm, the split bore layout allows the Linatron to be setup perpendicular or parallel to the B_0 field. The Linatron is currently in the parallel configuration. The magnet is actively shielded to produce a zero Gauss region at 1.2-1.4 m from isocentre. The imaging gradients are provided by two separate parts (Tesla, UK) that are fitted to both halves of the magnet and do not protrude into the bore [128].

6.2 Isocenter QA Device Prototype Development

The Australian MRI linac system isocenter alignment is characterised by the positions of the optical, MR imaging and radiation isocentre. The radiation source is at a fixed angle with fixed spatial relationship to the MLC collimation. Beam walkout may be introduced from the movable table system the Varian linatron source and MLC are mounted to that allows selectable SIDs. The MR imaging isocenter is defined by the fixed geometry of the MRI gradient coils. The optical isocenter is marked by laser cross hairs to match the MR imaging isocenter.

The spatial relationship of the optical, imaging and radiation isocenter is an importance component of a QA program as geometrical offset between these points may result in a population wide geometrical error for all image-guided treatments on that machine. The American Association of Physicists in Medicine Task Group 142 recommends daily confirmation of beam co-incidence from a single angle with imaging isocenter [129]. The Australian MRI linac isocenter facility's measurement procedure outlined in section 7.2 takes roughly 4 hours and is not feasible to incorporate into routine daily QA.

The goal is to design a QA device that is capable of measuring the spatial relationship of the optical, MR imaging and radiation isocentre of the Australian MRI linac. The aim is to design a device that meets both the time requirements for use in daily QA as well as the accuracy requirements of commissioning measurements and monthly QA.

6.2.1 Design Criteria:

MRI Compatible - The device must meet the IEC definition of MRI safe or MRI conditional, the former being the device poses no known hazards in all MRI environments and the later classification indicating the device been demonstrated to pose no known hazards in a specified MRI environment with specified conditions of use [130]. The device must operate as intended when at the centre of the MRI scanner bore in the 1 T magnetic field. Both the construction and operation of the device should not interfere with the operation of the MRI. This imposes the condition that the design should not contain any ferromagnetic materials.

Real time beam central axis spatial measurement – To measure the location of the radiation beam central axis relative to the imaging and optical isocenter a real time monolithic silicon detector will be incorporated into the device. The detector must be magnetic field compatible, have real time readout and a high spatial resolution.

MRI Visualisation – The phantom must contain enough MR visible material to perform scans using clinical scanning sequences. Ideally the MR visible material should be permanently contained within the phantom to simplify the devices use and reduce the amount of time required to setup and perform the measurements.

Practical design – To meet the practical requirements for daily use, the device needs to be light weight such that a single person is able to perform the measurements. Ideally the device would not contain liquids that may leak or require filling/emptying.

MRI imaging isocenter characterisation accuracy – MR images contain geometric distortion predominantly due to the inhomogeneity in the main magnet, the nonlinearity in the gradient fields and the eddy currents associated with the switching of the gradient coils [131]. The geometric distortion typically is lowest at the center of the magnet and increases in magnitude with distance radially outwards from the center. Imaging markers used to determine the position of the phantom relative to the imaging isocenter should be located close to the center of the MRI to minimise the influence of the image distortion in the analysis. Stereotactic radiosurgery requires that the coincidence of the imaging and treatment isocentre are ≤ 1 mm while radiation therapy requires a nominal spatial accuracy of ≤ 2 mm [129]. The uncertainty in the measurement of the coincidence of the imaging and treatment isocentre is influenced by the uncertainty in the beam central axis determination using the detector, the imaging isocentre determined from phantom scans and the accuracy in when the device is manufactured as the analysis assumes the detector is located centrally within the phantom.

6.2.2 3D distortion quantification of the Australian and Elekta Unity MRI Linacs

Geometric distortion in MRI is caused by both patient factors and system specific factors [132]. The spatial encoding of MRI data is achieved via frequency and phase encoding which both rely on the application of gradients to the main magnetic field (B_0). As such system specific distortions result from the non-linearities of the gradient coils and variations in the homogeneity B_0 field within the scanner [133]. Each MRI has its own unique uniformity and gradient non-linearities. The patient induced distortions are also due to additional B_0 inhomogeneity introduced by the chemical and physical makeup of the human body. Chemical shift is the term for the shift in the frequency encoding direction of fatty tissue relative to non-fatty tissue due to the different resonate frequency of fat relative to water [134]. Magnetic susceptibility artefacts arise from variations in the magnetisation properties of different tissue types, such as at air-tissue interfaces [135]. The magnitude of the patient related distortions are dependent on the field strength of the scanner and increase in magnitude at higher field strengths.

MRI Linac	Sequence	TE/TR (ms)	Field of View (mm)	Voxel size (mm)	Pixel BW (Hz/pix)
Australian MRI Linac	SE	14/3060	380.0 x 380.0 x 360.0	0.742 x 0.742 x 3.000	130
Elekta Unity	GR	3.401/6.69	560.0 x 560.0 x 400.0	1.094 x 1.094 x 1.000	431

Table 6.1: Acquisition parameters of sequences used for 604-GS phantom scans on the Australian MRI Linac and Unity MRI Linac. SE - Spin-echo pulse sequence, GR - Gradient echo sequence

To inform the design of the isocentre device the geometric distortion of the Australian and Elekta Unity MRI Linacs is characterised using the model 604-GS large field of view MRI distortion phantom (CIRS, Norfolk, VA, USA). The 604-GS phantom is a hollow PMMA cylinder, 300 mm long and 330 mm in diameter. The phantom contains a 3D grid of 3 mm diameter rods, with 2152 control points spaced at intervals of 20.3 mm inferior-superior, 20.5 mm anterior-posterior and 21.5 mm in the left-right directions. The phantom is supplied empty and the user is required to choose an appropriate filling solution to provide the MR signal. The phantom was filled with a copper sulphate solution recommended in AAPM report 100 [136]. The phantom measures the imaging distortion by comparing the positions of the control points in the MR image with their nominal positions. The Analysis of the 604-GS distortion phantom scans was performed using the commercial software 'Disotortion Check' (model 603S, CIRS, Norfolk, VA, USA).

Australian MRI Linac

The 604-GS phantom was scanned with the centre of the phantom aligned to the centre of the Agilent magnet using the Australian MRI Linacs external lasers [see Fig. 6.2]. The Acquisition parameters of the imaging sequence used are listed in Table 6.1. There are no distortion corrections currently available for imaging on the Australian MRI Linac, corrections have been applied offline by Shan et al however are not yet available within the workflow at the Australian MRI Linac facility [137]. The magnitude of the measured distortion is displayed in Fig 6.3(a), showing the increase with increasing distance from isocentre, with greater than 3 mm distortion at 75 mm from isocentre. The distortion in the central axial, sagittal and coronal planes are displayed in contour plots in Fig. 6.4(a), 6.5(a) and 6.6(a) respectively.

Unity MRI Linac

Although the isocentre device is intended for the specific requirements of the Australian MRI Linac, application on other MRI Linac systems is desirable. The 604-GS

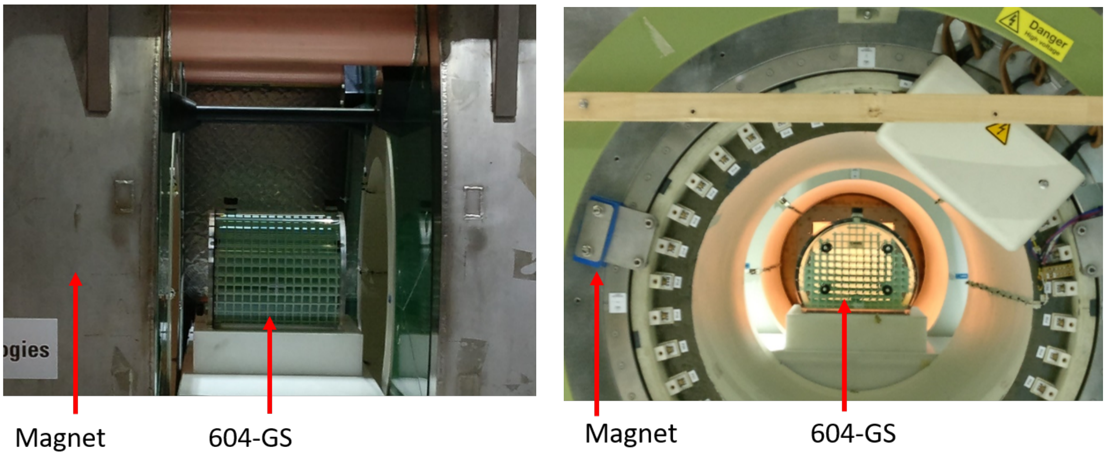

(a) (b)

Figure 6.2: Photographs of model 604-GS MRI distortion phantom (CIRS, Norfolk, VA, USA) setup on the Australian MRI Linac.

phantom was scanned with the centre of the phantom aligned to the isocentre of the Unity MRI Linac using a combination of external lasers and couch top positioning aids, the acquisition parameters for the imaging sequence used are listed in table 6.1. 3D distortion corrections are applied online. The magnitude of the measured distortion shown in Fig 6.3(b) is less than 0.4 mm at 75 mm radially from isocentre and less than 1.3 mm distortion at 200 mm from isocentre. The distortion in the central axial, sagittal and coronal planes are displayed in contour plots in Fig. 6.4(b), 6.5(b) and 6.6(b) respectively.

6.2.3 Initial Prototype Design

An initial prototype phantom [see Fig 6.7] was developed to test the feasibility of embedding a monolithic silicon detector into a MRI compatible phantom that also combines the use of MR markers to locate the imaging isocenter and external grooves to allow alignment with the setup lasers for simultaneous characterisation of optical isocenter.

The proposed method is to align the phantom to lasers, perform volumetric imaging and then use a beam that is collimated to be symmetric about central axis to irradiate the detector from the beam angle being investigated. The known spatial relationship between the MR fiducial, strip detector and laser alignment markings allows calculation of the relative isocentre locations in the plane of measurement shown in Fig 6.9.

The initial prototype was constructed with a monolithic silicon strip detector, (sDMG-256A) consisting of 256 phosphorous implanted (n+) strips of 20 µm × 2000 µm with

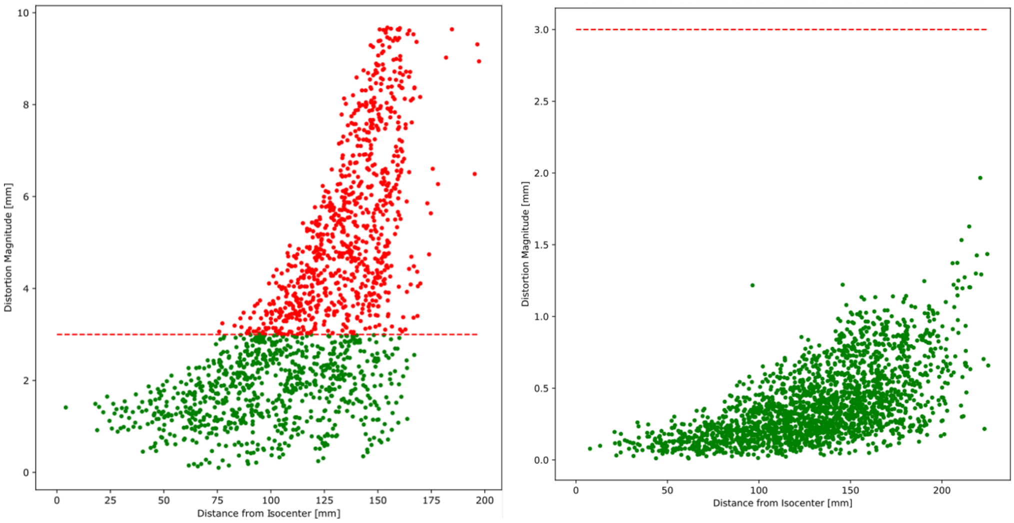

(a) **(b)**

Figure 6.3: Distortion at each measured fiducial point relative to its 3D vector distance from isocentre measured with CIRS Model 604-GS, (a) Australian MRI Linac (b) Unity MRI Linac.

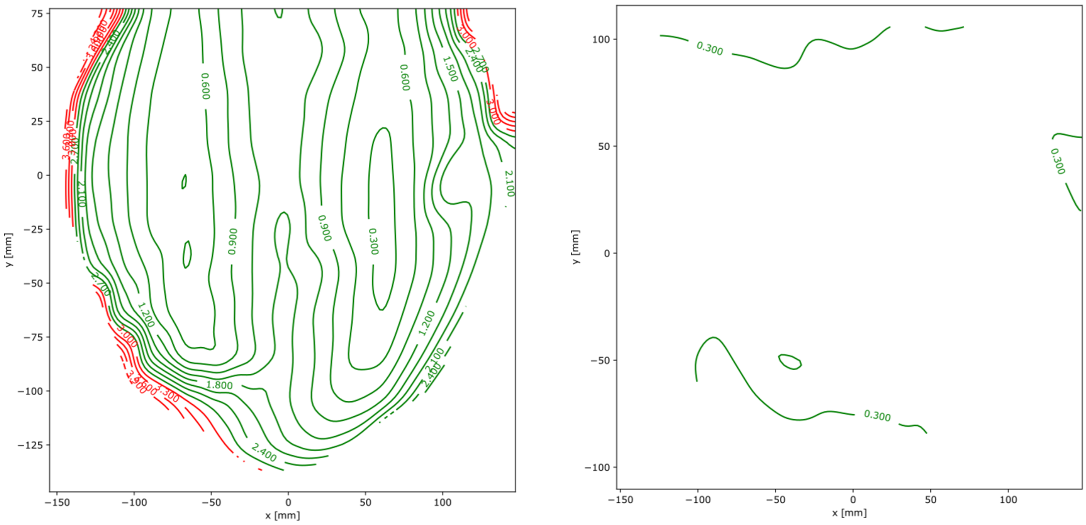

(a) **(b)**

Figure 6.4: Contour plot of distortion magnitude in the central axial plane measured with CIRS Model 604-GS, (a) Australian MRI Linac (b) Unity MRI Linac.

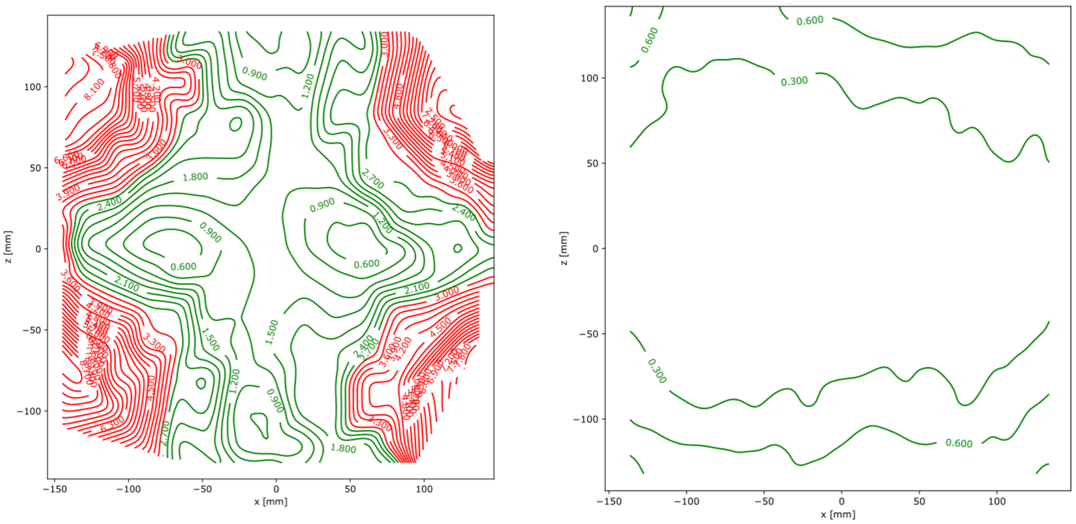

(a) **(b)**

Figure 6.5: Contour plot of distortion magnitude in the central sagittal plane measured with CIRS Model 604-GS, (a) Australian MRI Linac (b) Unity MRI Linac.

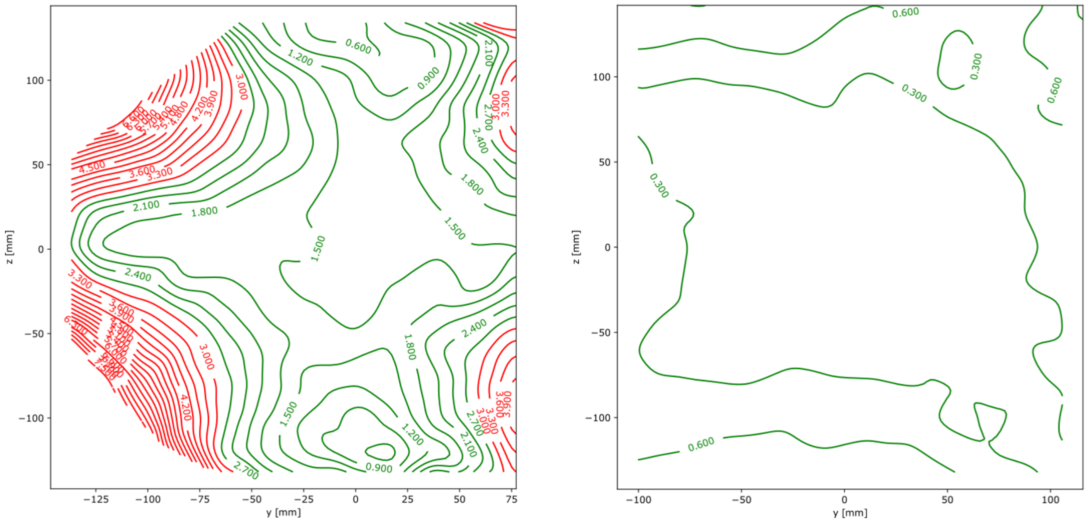

(a) **(b)**

Figure 6.6: Contour plot of distortion magnitude in the central coronal plane measured with CIRS Model 604-GS, (a) Australian MRI Linac (b) Unity MRI Linac.

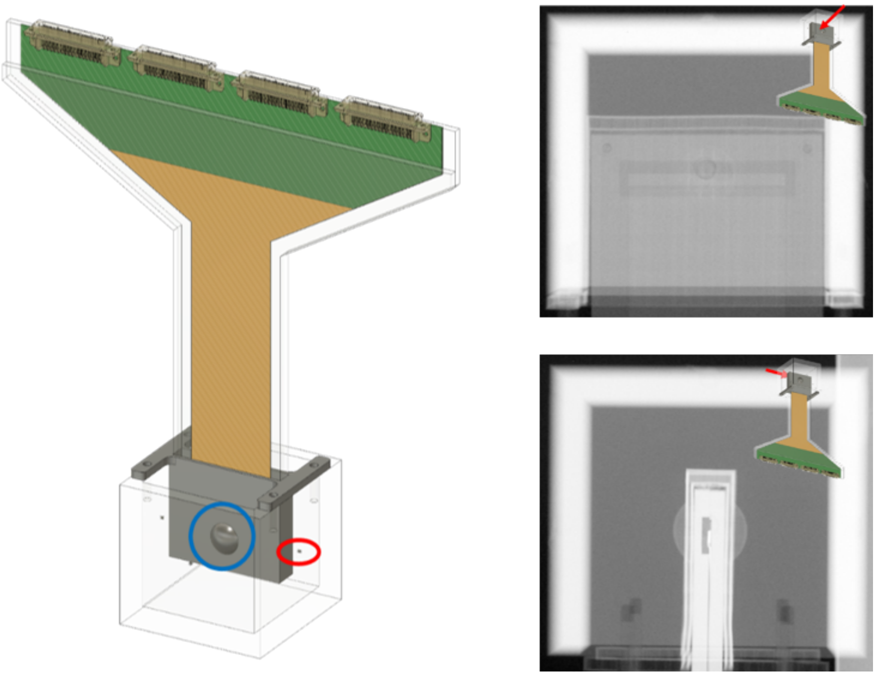

Figure 6.7: Left - sDMG-256A detector mounted in isocentre localisation phantom, blue circle – central MR fiducial, red circle – laser/MR fiducials. Right - Orthogonal radiographs of phantom and sDMG-256 detector.

200 µm pitch on a bulk p-type silicon substrate. The sDMG-256A detector, which is protected by PMMA housing, is mounted centrally in the MR compatible phantom. The phantom is filled with agar gel to provide MRI signal and contains a central fiducial for MR localisation and markings for laser alignment shown in Fig 6.7 and 6.9. MR fiducials were imbedded into the PMMA walls of the phantom 2.5 cm radially from the center of the phantom. Due to the one dimensional strip geometry of the sDMG-256A the radiation beam central axis offset can only be determined in one axis per irradiation.

6.2.4 Prototype testing on conventional linac

Measurements to test the feasibility of the proposed design for MV-imaging isocentre coincidence were performed on a Varian 2100iX linear accelerator (Varian Medical Systems, Palo Alto, CA) using a multileaf collimator defined 10 mm × 10 mm, 6 MV beam at the cardinal gantry angles [setup shown in Fig 6.8]. The phantom is aligned to lasers with the detector plane perpendicular to the beam pair being measured, volumetric imaging (MRI or CBCT) is performed and then use a symmetric beam to irradiate the detector from the beam angle being investigated. The FWHM is used to determine the centre of the MV beam, the known spatial relationship between the MR fiducial, strip detector and laser alignment markings allows calculation of the relative isocentre locations in the plane of measurement. The WL measurements

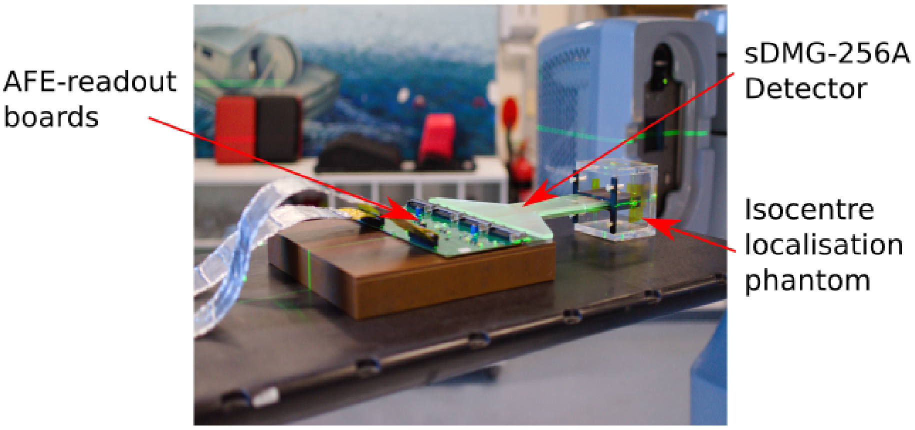

Figure 6.8: Isocenter characterisation measurement setup on Varian 2100iX.

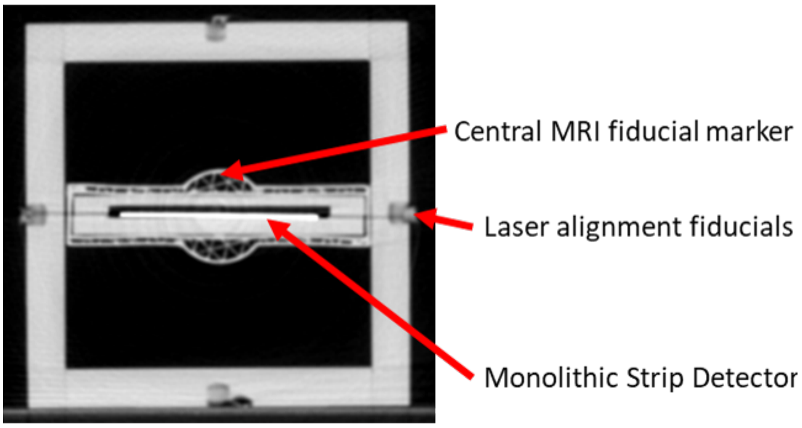

Figure 6.9: Axial slice from CBCT of phantom showing the plane containing the fiducials and detector.

made for comparison were performed using a QUASAR WL wand and analysed using DoseLab Pro (Mobius Medical Systems, LP, Tampa, FL). The measurements were repeated five times.

The MV-CBCT coincidence measured with the prototype phantom and with the WL method are shown in Table 6.2. The results for the two methods agree to within ±0.18 mm for the cardinal angle measurements performed.

The prototype device has shown the feasibility of using a high-resolution monolithic silicon detector in combination with an imaging phantom for MV-CBCT isocentre characterisation.

6.2.5 Prototype testing on the Australian MRI-linac

Multiple challenges were encountered testing the prototype device on the Australian MRI Linac. The challenges included triggering the detector system, the lower dose

Gantry Angle	Winston-Lutz Ave. ± 1SD (mm)	Prototype Phantom Ave. ± 1SD (mm)	Difference (mm)
0°	-0.23 ± 0.08	-0.30 ± 0.06	0.06
90°	-0.89 ± 0.07	-0.92 ± 0.09	0.03
180°	-0.44 ± 0.14	-0.26 ± 0.10	-0.18
270°	0.27 ± 0.06	0.19 ± 0.06	-0.08

Table 6.2: The MV-CBCT imaging isocentre coincidence measured with the prototype phantom and with the WL method.

per pulse of the Linatron source than a conventional Linac at the isocentre causing signal detector issues and MR imaging of the phantom.

Triggering the detector system

Clinical Linacs including the Varian Truebeam and Varian 2100iX have a variety of signals available at the modulator. One of these signals is a transistor-transistor logic (TTL) signal that is synchronous with the system clock of the Pulse Forming Network (called the SYNC from here on). Using the SYNC, detector systems can be triggered to perform measurements of the beam pulse by pulse, which gives pulse by pulse information of the beam and increases the signal to noise ratio. The Varian Linatron does not have an available SYNC signal.

To synchronise the DAQ of the sDMG-256A detector system with the Linatron a diode (n-type, 1mm^3 sensitive volume) with a bystable comparator circuit was used (referred to from here as the external trigger). The diode is placed within the radiation field, conveniently on the Australian MRI-linac it may be placed between the source and the MLCs so that it has minimal influence on the field.

Characterisation of the external trigger systems effect on the detector system was performed on an Varian 2100iX. The delay between the Clinacs SYNC and the external trigger was measured to be 7.60 µs using a oscilliscope [see Fig. 6.10]. The radiation pulse arrives after the SYNC and before the trigger (using the radiation pulse). The result is a loss in signal due to triggering part way though the radiation pulse. A signal loss of ≈55 % was observed when using the external trigger relative to the SYNC. To investigate if the use of the external trigger effects profile measurements required for the isocentre phantom a 6 MV 20 mm × 20 mm profile was measured on a Varian 2100iX using both the SYNC and external trigger system. Comparison of the profiles are shown in Fig 6.10(b), the profiles agree to within 0.3%.

The external trigger was tested with the sDMG-256A detector system at the Australian MRI linac initially with all components of the system outside the MRI's bore in the magnetic fringe field measured as 0.05 T at the detector using a MAGSYS

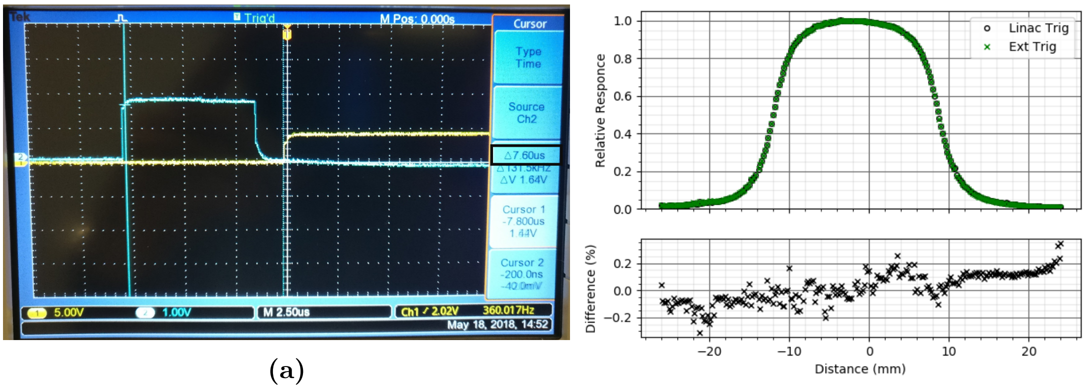

(a)

(b)

Figure 6.10: (a) Comparisoin of timing for the external triggers (Ch1-yellow) and the sync pulse (Ch2-blue) of a Varian 2100iX Linear accelerator (b) Beam profiles measured using sDMG-256A with the external trigger (green crosses) and the sync pulse (black circles) of a Varian 2100iX

HGM09s gaussmeter (Dortmund, Germany) [setup shown in Fig 6.11(a)]. This was to ensure operation of the system without magnetic field effects. The detector was setup at 100 cm SSD and with 1 cm of solid water build-up. The Linatron was operated in “High mode” (nominal energy 6 MV) with a radiation pulse frequency of 200 Hz, MLCs were set for a 2 cm × 2 cm at the surface of the solid water. Linearity of the detector system was measured by integrating the signal for a continuous irradiation for 5 s, 10 s , 15 s and 20 s. The detector response as a function of irradiation time was observed to be linear with $R^2 = 0.999$.

Signal detection issues

The dose per pulse from the Linatron source is lower than a conventional linac, the larger SID (180 cm) further decreasing the dose per pulse at the detector when setup at the centre of the MRI. Combined with the loss of signal from using the external trigger system, the sDMG-256A was unable to measure beam profiles both when considering individual beam pulses and integrated measurements when setup at the isocentre (SID 180 cm) of the Australian MRI-Linac.

MR Imaging Issues

Imaging the prototype device with the MR also has challenges due to the small volume of agar gel used to produce the MR signal. The head coil was required to produce usable images, phantom setup and MR image shown in Fig 6.12. This is undesirable for a daily QA device as use of the head coil adds extra complexity and time to the set up the measurement.

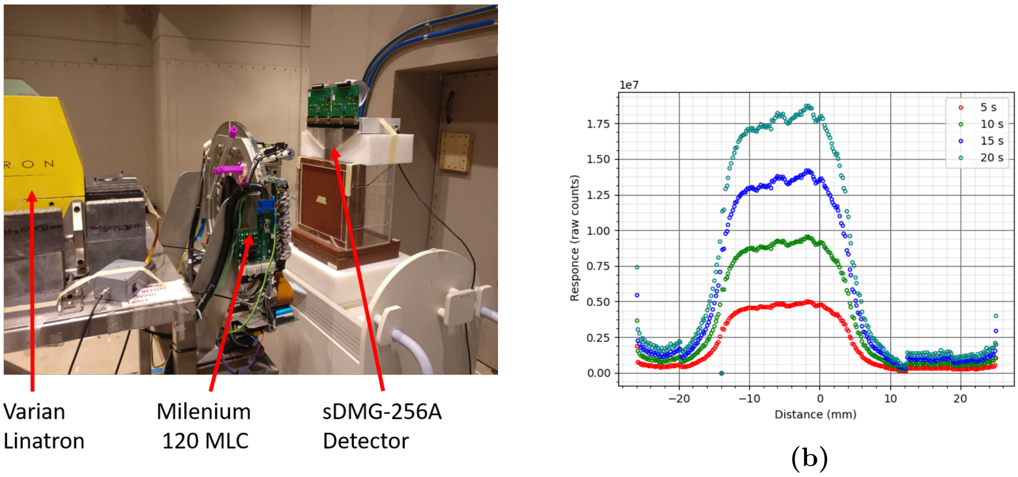

(a)

(b)

Figure 6.11: (a) Photo of actual setup testing the external trigger with the Linatron radiation source (b) Profiles measured during linearity test, profiles are 'uncorrected' for background and individual channel response variation

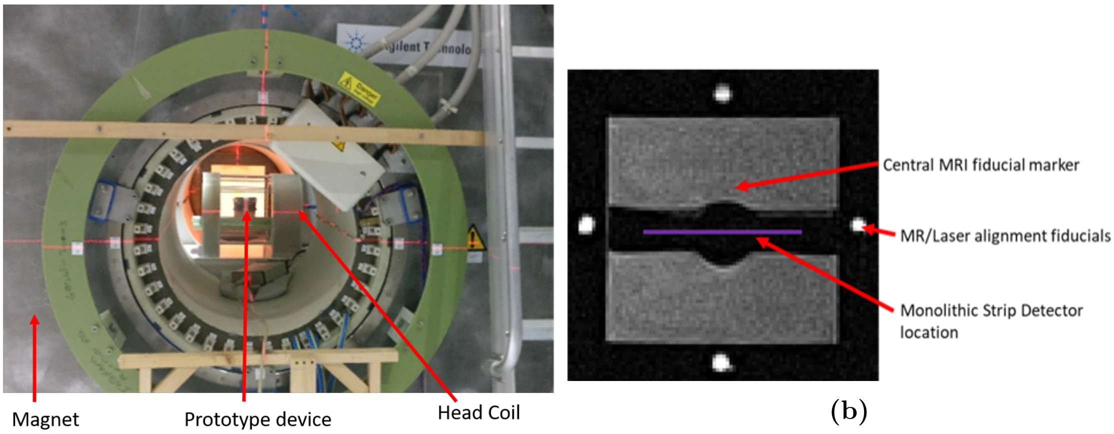

(a)

(b)

Figure 6.12: (a) Photo of actual setup testing the external trigger with the Linatron radiation source (b) MRI of phantom showing the plane containing the fiducials and detector

6.2.6 Lessons learnt from Initial Prototype Design

Detector choice – the sensitive volume of the sDMG-256A is too small for beam profile measurements of the Linatron using the external trigger at 1.84 m SAD. This also means that the DUO detector used in Chapter 5 will not be suitable due to the similar sensitive volume of the diodes.

MR Imaging – The small volume of MR visible material required the use of a head coil to produce usable images. It is desirable to avoid the use of the head coil for daily QA measurements as its use increases the time taken to set up the measurement.

6.3 Final Phantom Design

The final device design [see Fig 6.13] utilises the MP512 pixelated array detector that is based on the same monolithic silicon technology as the sDMG-256A and DUO detectors. The MP512 has 512 pixels arranged in a 22 x 22 array with another 7 pixels on each side of the array. Each sensitive volume has dimensions of 500 µm × 500 µm × 100 µm. The sensitive volume of the MP512 is 6 times larger than the sDMG-256A, this overcomes the insufficient SNR observed during testing of the sDMG-256A at the isocentre of the Australian MRI-Linac. The author assisted with the study by Alnaghy et al demonstrating the use of the MP512 on the Australian MRI Linac [100]. The 2D arrangement of the diodes of the MP512 allows the total beam central axis offset in the plane of the detector to be determined from a single measurement, halving the phantom setups required relative to using the sDMG-256A with its strip detector geometry. The phantom is constructed from PMMA, with external dimensions 200 mm × 200 mm × 160 mm, and holds a maxium of 3420 mL of agar gel. This removed the requirement to image the phantom using the head coil simplifying the phantom setup and decreasing the time required to use the phantom. Laser alignment cross hairs are located on four sides of the phantom. The phantom is symmetric about the plane of the detector with a void on each side to contain the MR visible material. Ten MR fiducials have been placed within 3 cm radial distance of the center of the phantom.

6.3.1 Final Design Assessment

Construction of the PMMA phantom was undertaken by the University of Wollongong's engineering workshop using the provided 3D design files. The phantom was constructed from 10 mm thick PMMA sheets that were milled to size using a computer numerically controlled milling machine and bonded together using ace-

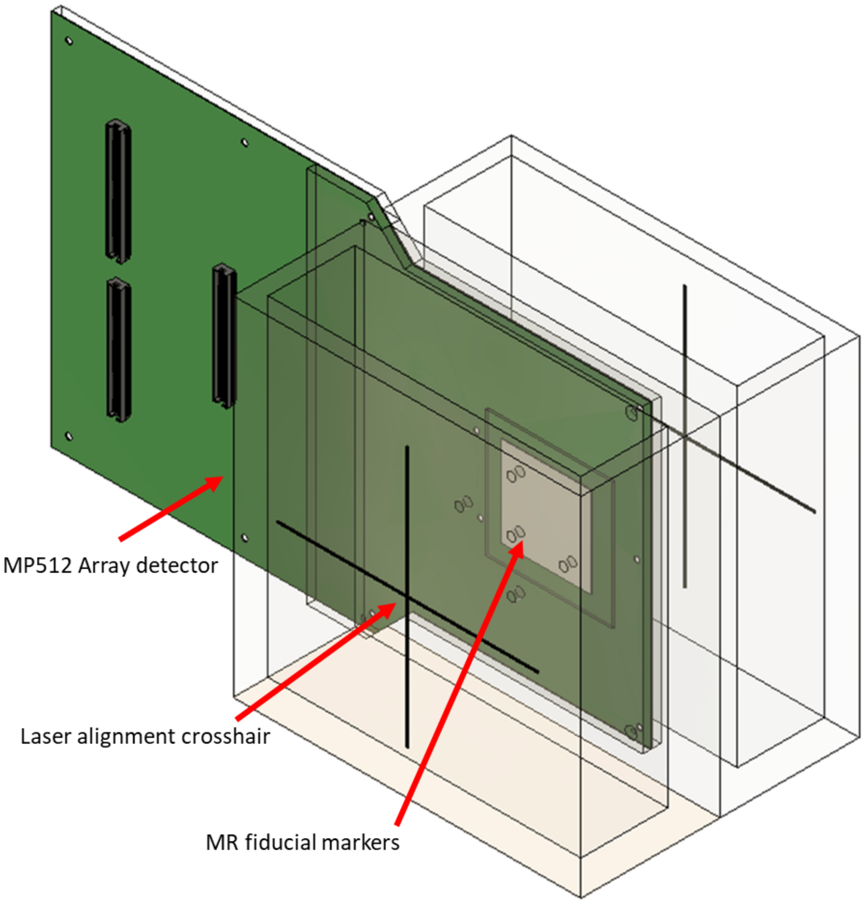

Figure 6.13: 3D model of Isocenter QA device designed for Australian MRI Linac.

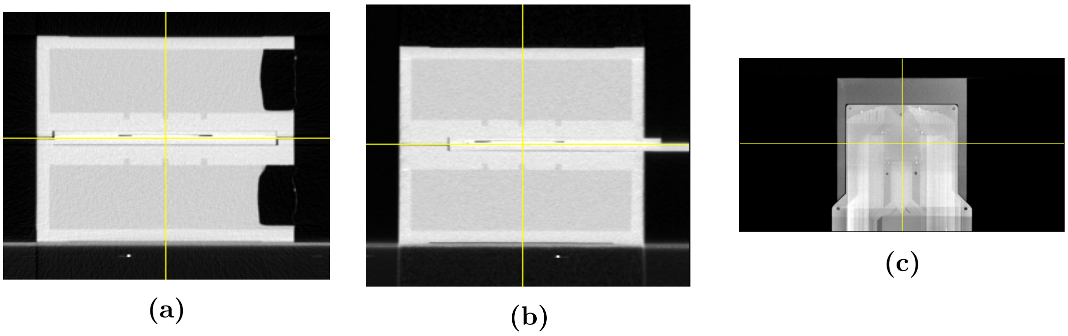
(a) (b) (c)

Figure 6.14: Phantom (a) axial slice on CT, (b) sagittal slice on CT, (a) coronal slice on CT.

tone. Imaging of the final phantom with both CT and planar X-ray to assess the construction of the phantom with focus on the spatial relationship of the laser alignment crosshair, MRI fiducial markers and the detector location is shown in Fig. 6.14. The alignment of the laser crosshairs and MRI fiducials were within the limitations of the imaging. However it was identified that the detector location is offset relative to the laser crosshairs and MRI fiducials as indicated by red arrows in Fig 6.15(a) showing the uneven gaps between the detector and the MR Fiducials. The magnitude of the detector offset is less than 1 mm, accurate determination proved difficuilt. The offset is a result of a combination of uncertainty in the mounting of the MP512 to its PCB, and the construction techniques of the phantom, namely the process of bonding the machined PMMA sheets together.

6.3.2 Testing on conventional linac

The phantom was setup using the laser alignment crosshairs on a Varian True beam [see Fig 6.15(b)], volumetric imaging was performed using CBCT and then a 6 MV 2 cm × 2 cm MLC defined field (symmetric about isocentre) was used to irradiate the phantom from beam angles perpendicular to the detector plan. The phantom had to be setup separately for gantry angles 0°/180° and 90°/270°. The known spatial relationship between the MR fiducials, MP512 detector array and laser alignment markings allows calculation of the relative isocentre locations in the plane of measurement. As with the prototype phantom, comparison measurements were performed using a QUASAR Winston-Lutz Wand Phantom (Modus Medical Devices, Canada) and analysed using DoseLab Pro (Mobius Medical Systems, LP, Tampa, FL). The measurements were repeated five times.

The MV beam – CBCT isocentre coincidence measured with the isocenter phantom and with the WL method are shown in Table 6.2. An example of the DoseLab (Mobius Medical Systems, Houston, TX) analysis of Winston-Lutz MV beam – CBCT isocentre coincidence for cardinal gantry angles is shown in Fig. 6.16. The

Gantry Angle		Winston-Lutz Ave. ± 1SD (mm)	Isophan Ave. ± 1SD (mm)	Difference (mm)
0°	x	0.04 ± 0.02	-0.47 ± 0.45	0.50
	y	-0.42 ± 0.10	-0.22 ± 0.03	-0.20
180°	x	0.64 ± 0.13	0.95 ± 0.05	-0.30
	y	0.07 ± 0.12	-0.35 ± 0.20	0.42
90°	x	0.21 ± 0.09	0.77 ± 0.10	-0.56
	y	-0.18 ± 0.10	0.01 ± 0.03	-0.19
270°	x	0.61 ± 0.08	0.03 ± 0.21	0.58
	y	-0.15 ± 0.10	-0.93 ± 0.08	0.78

Table 6.3: The MV-CBCT imaging isocentre coincidence measured with the Isocenter phantom and with the WL method.

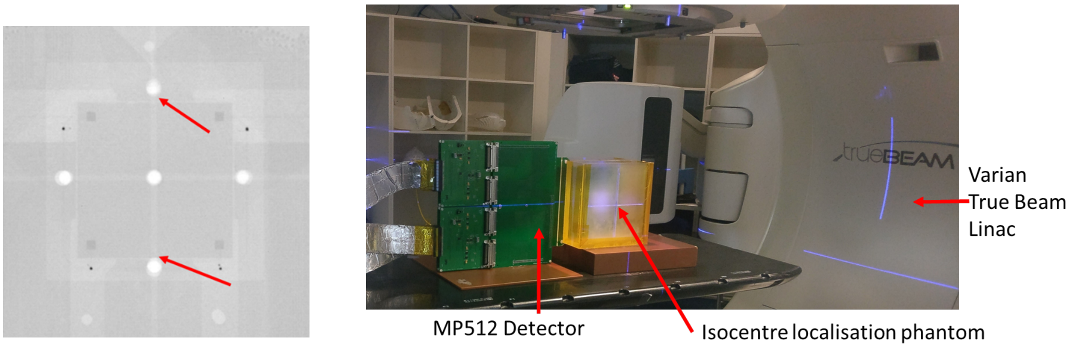

(a)

(b)

Figure 6.15: (a) Planar X-ray of phantom indicating offset between detector and the MR Fiducials/laser crosshair (b) Isocenter characterisation measurement setup on Varian TrueBeam.

2D fluence maps used to identify to centre of the MV beam are shown in Fig. 6.17. The results for the two methods vary by up to ±0.78 mm for the cardinal angle measurements performed. This is a larger variation than the first prototype phantom and may be due to uncertainties in the spatial relationship of the MP512 detector relative to the fiducials and laser alignment markings of the phantom as identified in section 6.3.1. The offset of the detector within the phantom relative to the fiducials/laser marks identified in section 6.3.1 has not been corrected for in the analysis.

6.4 Conclusion

The device has been developed with the goal of measuring the coincidence of the radiation beam with the MR imaging and optical isocenter of the Australian MRI Linac. The limitations of the initial prototype that were identified when testing on the Australian MRI Linac have been addressed in the final design, namely the

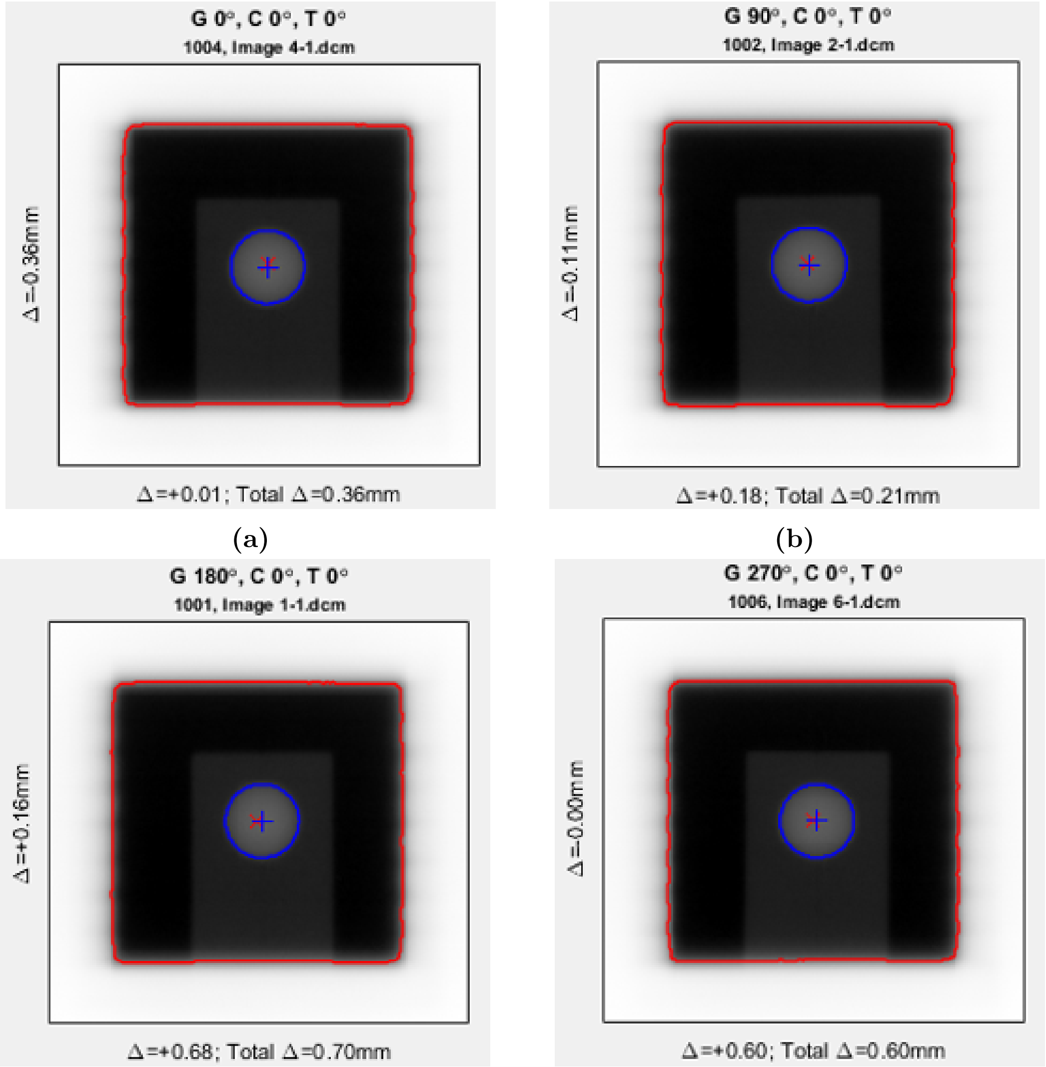

(a) **(b)**

(c) **(d)**

Figure 6.16: (a) - (d) DoseLab (Mobius Medical Systems, Houston, TX) analysis of Winston-Lutz MV-CBCT coincidence for cardinal gantry angles. Blue cross indicates the ball bearing center and the red cross marks the MV field center.

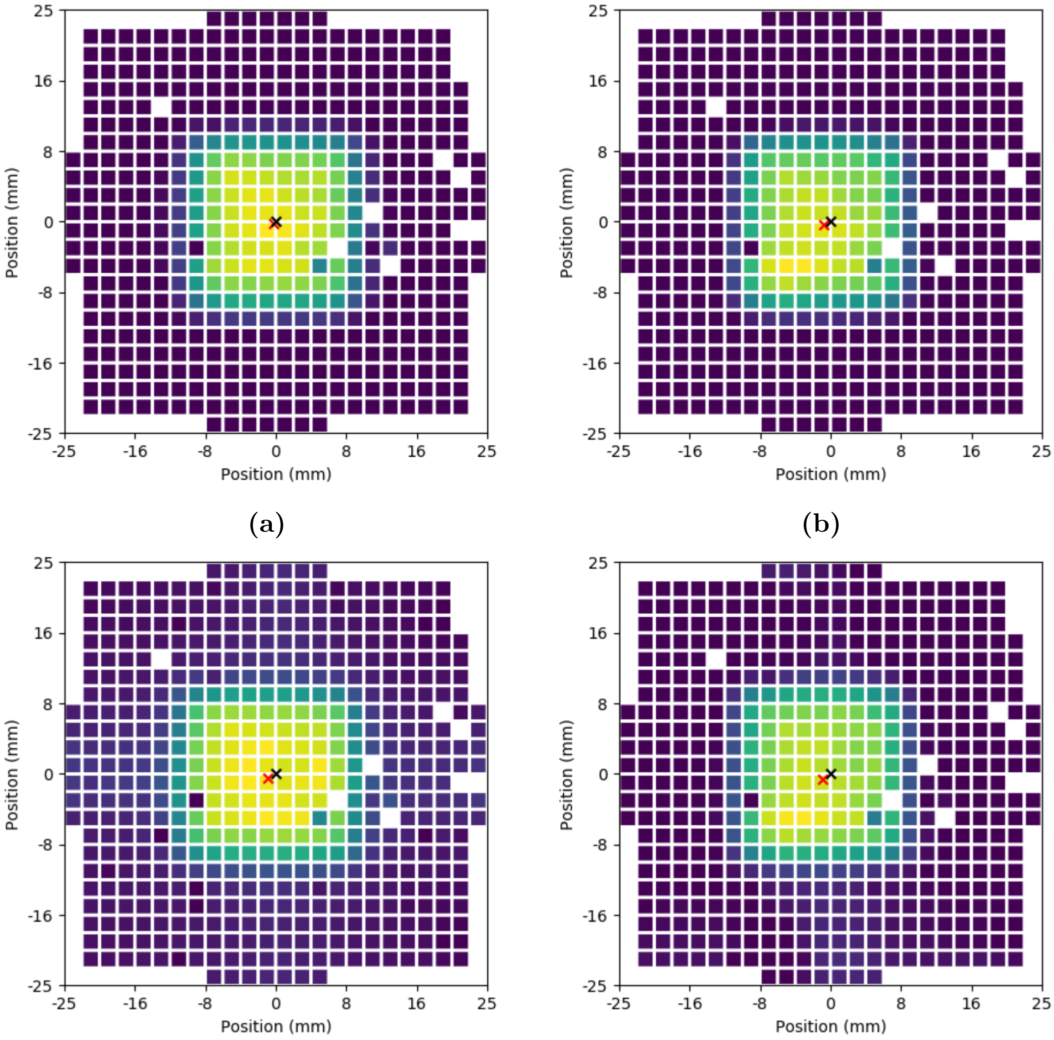

(a)

(b)

(c)

(d)

Figure 6.17: (a) 0° (b) 90° (c) 180° (d) 270°, Beam's eye view of 2 cm × 2 cm field symmetric about CAX as acquired by the MP512 for MV-CBCT coincidence for cardinal gantry angles of Varian Truebeam. Black cross indicates imaging isocenter, red cross indicates the calculated beam central axis.

detector choice to address the low signal challenges and the containment volume for MR visable material has been increased to address the requirement of the head coil for imaging. The final design was constructed and tested on a conventional Linac (Varian True beam) by comparing MV-CBCT coincidence measurements made with the prototype devive to measurments made with a commercial Winston-Lutz Wand Phantom and Doselab analysis softwere.

Chapter 7

Isocenter Characterisation of the Australian MRI-Linac

Contributions: The measurements and results presented using the MP512 detector with isocentre phantom were collected and analysed by Causer T. The isocentre results used for comparison of the data collected at the Australian MRI Linac was provided by the facility staff and were contributed to by Jelen, U., Begg, J., Dong B, Liney, G., and Roberts, N.. The work in this chapter was supervised by Metcalfe, P., Rosenfeld, A. and Oborn, B.M. The operation of the Unity MRI Linac for the isocentre measurements was performed by Jameson, M.

7.1 Overview

The alignment of the imaging and radiation isocenter is an essential component of linac commissioning and ongoing QA, as any geometrical offset between them results in a population wide geometrical error for all image-guided treatments on that machine. The optical isocenter indicated by the external lasers play an important role in initial patient setup as well as assisting with the setup of machine QA equipment, particularly QA equipment that is not MR visible. The coordinate system for the Australian MRI linac system originates at the center of the MRI bore. The z-axis is parallel to the beam CAX and the x-axis is parallel to the fixed direction of the MLC leaf motion and perpendicular to the y-axis as indicated in Fig 7.1. The first half of this chapter describes two methods of characterisation of optical, MR imaging and radiation isocentre for the Australian MRI-Linac. The first method is the procedure used by the facility staff to assess the system alignment, the second method described uses the novel QA device described in Chapter 6. The final sections of this chapter describe preliminary testing of the isocentre device on an

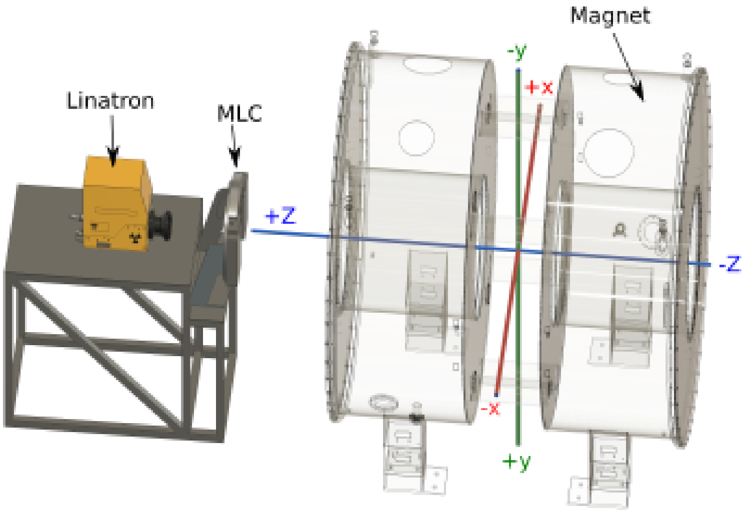

Figure 7.1: Diagram of Australian MRI-linac with a coordinate system originating at the system's isocentre overlaid

Elekta Unity MRI Linac.

7.2 Methodology

7.2.1 Australian MRI Linac facility

Equipment:

To determine the MR isocenter a dedicated MRI phantom is used. The phantom was designed by facility staff and manufactured by Leeds Test Objects. The phantom shown in Fig 7.2(a) is constructed of PMMA and consists of two chambers separated by 2 cm thick wall with five narrow bore holes connecting them and filled with MRI visible solution. Two acrylic plates with embedded fiducial markers for MV visibility are used with stand-alone EPID (XRD 1640 AL7-M PerkinElmer, USA) to assess beam alignment. The EPID has a detector size of 41 cm x 41 cm with a pixel matrix of 1,024 × 1,024.

Method:

The dedicated MR phantom is aligned to the lasers and imaged. The acrylic plates are then aligned to the lasers at two locations, at 2.265 m from the Linatron nozzle (i.e. 2.343 m from the source), and at the end of the bore, at 4.206 m from the Linatron nozzle (i.e. 4.284 m from the source). The EPID panel is set up at the first position (EPID position 1 in Fig. 7.3). Open field and MLC half-blocked fields were acquired (high energy mode, TR 200) for Linatron at SID positions 8 to 1.

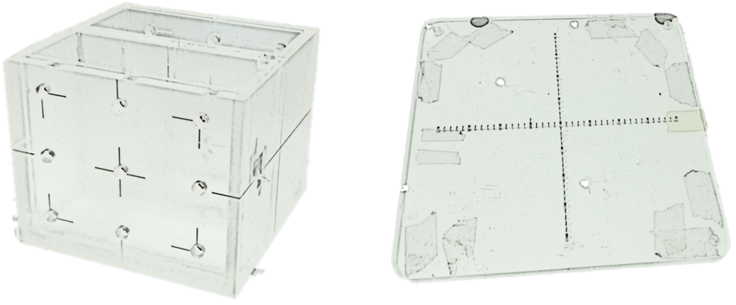

(a) **(b)**

Figure 7.2: Phantoms used by Australian MRI Linac facility staff when characterising ioscentre (a) dedicated MRI phantom manufactured by Leeds Test Objects (b) acrylic plate with embedded fiducial markers for MV visibility (two plates are used).

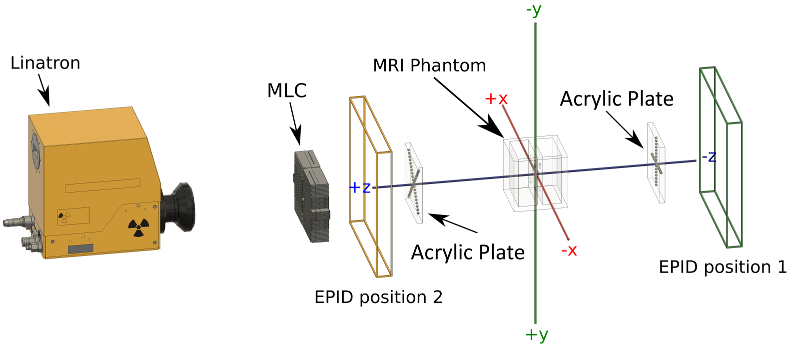

Figure 7.3: Schematic representation of the phantom setup used for geometrical alignment of the system by the Australian MRI Linac facility

The EPID panel is then set up in front of the bore (EPID position 2 in Fig. 7.3) at the distance of 1.515 m from the Linatron nozzle (i.e. 1.593 m from the source) as measured with the Linatron at position 8. Ball bearings (BB's) indicating the position of the 'outside' lasers were placed on the front face of the EPID. Open field and half-blocked fields were acquired (high energy mode, TR 50). Further details on the methodology and equipment used to characterise the Australian MRI linac's Isocentre alignment have been published by Jelen et al [138].

Data Processing:

The EPID imagings for the four half beam blocks (Left side, Right side, Top and bottom) are subtracted from one another and the results overlayed, example for Linatron position 8 shown in Fig 7.4. In the open field images acquired with EPID behind the bore, the coordinates of the shadow of the central BB of the proximal phantom with respect to the shadow of the central BB of the distal phantom were recorded as the source position relative to the laser. Open fields acquired with the

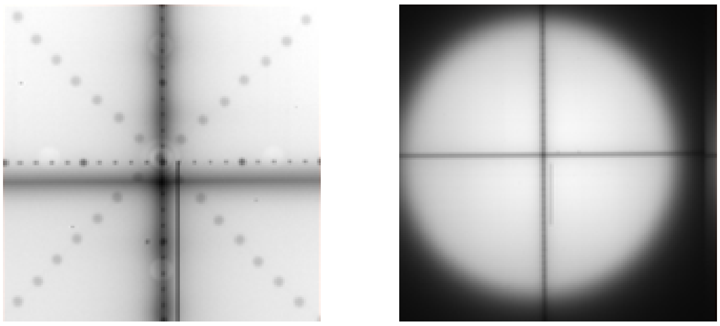
(a) (b)

Figure 7.4: Half blocked fields imaged behind the bore (left) and in front of the bore (right) for linatron at position 8, supplied by Australian MRI Linac facility.

EPID in front of the bore were used to assess the beam angle. The measurements were corrected for the source offset established above. Half-blocked fields were used to determine the projected position of the MLC central axis at the two EPID positions. Projections of the MLC CAX in the isocentre plane are interpolated from the positions based on the data obtained with EPID measured at each end of the MRI bore.

7.2.2 Measurement of system isocenter alignment using MP512 Isocentre Phantom

Method:

The QA device discussed in Chapter 6 (henceforth referred to as the MP512 Isocentre Phantom) is setup with its crosshair markings aligned with the external lasers, shown in Fig 7.5. The empty chambers of the device are prefilled with agar gel to provide MR signal. Alnaghy et al demonstrated increased noise in MR Imaging if the MP512 is powered on during image acquisition [100]. With the power to the MP512 detector system turned off the phantom is imaged using T1-weighted spin-echo sequence. The power is then turned on to the MP512 and irradiated using a MLC defined field symmetrical about CAX (field size is limited by the 50 mm × 50 mm array size).

Data Processing:

Within the MP512 Isocentre Phantom the MR fiducial markers are arranged so the centre of the XY plane coincides with a marker as well as the intersection of two pairs of fiducials [see Fig 6.13], the measured offset between the center of the phantom and the imaging isocenter indicates the offset between lasers and MR imaging ioscenter. The MP512 detector is located centrally within the device, the FWHM of the field in the X and Y direction is used to locate the beam CAX. The background signal

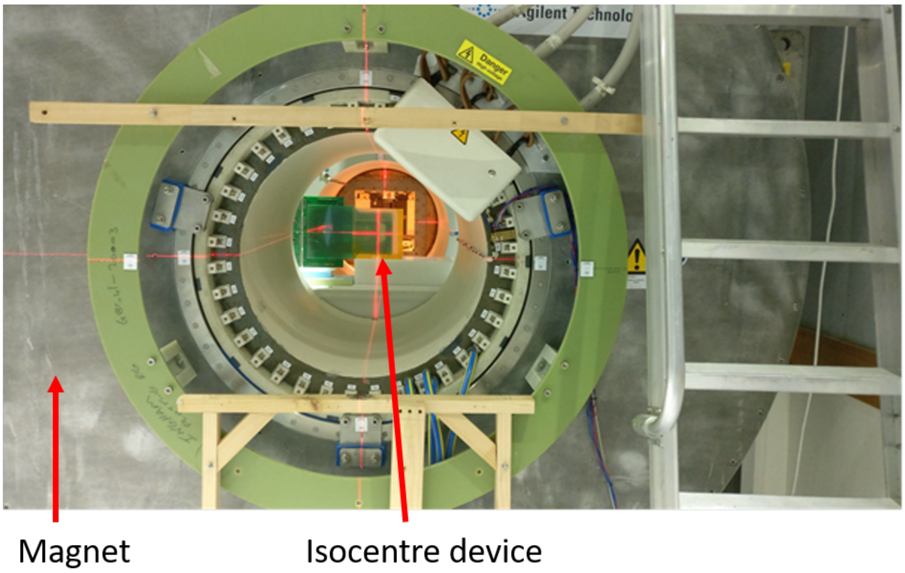

Figure 7.5: Photograph of QA device setup aligned to lasers in the Australian MRI-linac.

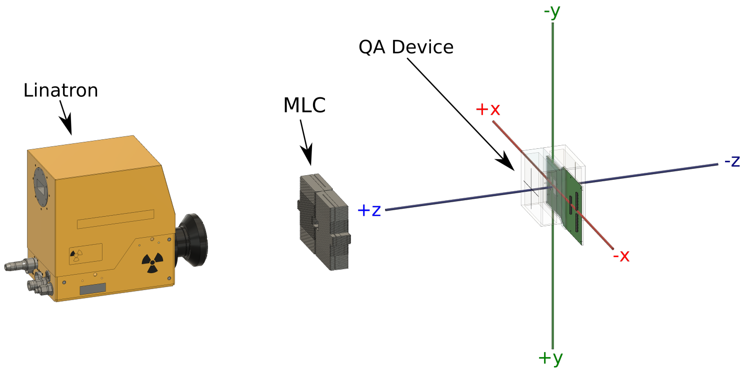

Figure 7.6: Schematic representation of the MP512 Ioscentre Phantom setup used for isocentre verification at the Australian MRI Linac facility

of the MP512 is sampled prior to irradiation. Processing to account for differences in pixel sensitivity and preamplifier gain has been applied by the method outlined in Wong et al [139]. This method requires irradiation with a uniform radiation field and in this case was performed separately on a Varian linac with a flattening filter to produce uniform irradiation of the array, as this is not feasible on the Linatron due to the flattening filter free beam. The accuracy of the FWHM measurements compared to EBT3 film using an MP512 detector on the Australian MRI Linac was investigated by Alnaghy et al [100]. Alnaghy et al showed the FWHM and penumbral widths matched between the MP512 and film to within 1mm, this was determine to be the experimental uncertainty of the measurements presented [100].

7.3 Results

7.3.1 Australian MRI Linac facility

The results for the facility determined MLC collimated MV beam centre projection at the imaging isocenter are shown in Fig 7.7. The offset of the MV beam is measured relative to the lasers, the lasers are assumed in the analysis to represent the MRI imaging isocentre as they are adjusted to match the imaging isocentre immediately prior to the MV centre measurements. In the x direction the beam CAX offset was at most 5.32 mm at Linatron position 1. In the y direction the beam CAX offset up to 1.8 mm at position 5. It should be noted that these multi mm offsets are corrected for (in the x-axis) with an MLC offset table however all measurements taken at the Australian MRI Linac for this thesis chapter were without offset table corrections.

7.3.2 MP512 Isocentre Phantom

The location of the optical ioscenter (lasers) determined from the location of the center of the phantom relative to the MR imaging isocenter was measured using the MRI console to be (0.95 mm, -0.01 mm , -2.34 mm) in x, y and z directions respectively. Selected slices of the MRI dataset are shown in Fig 7.9. Beam's eye view of symmetric field defined by two MLC leaf pairs resulting in a 1.8 cm x 1.8 cm square field at the isocentre (field size increases due to beam divergence for positions 2-5) symmetric about CAX as acquired by the MP512 for linatron positions 1 to 5 are shown in Fig. 7.10. The beam walk out is largest at position one with a 3.56 mm x-direction offset between the MR imaging isocenter and the beam CAX. The measurements agree reasonably well between the Australian MRI Linac facility method and the method employing the MP512 Isocentre Phantom developed in chapter 6, with the largest variation measured in the x-axis of 1.76 mm difference at

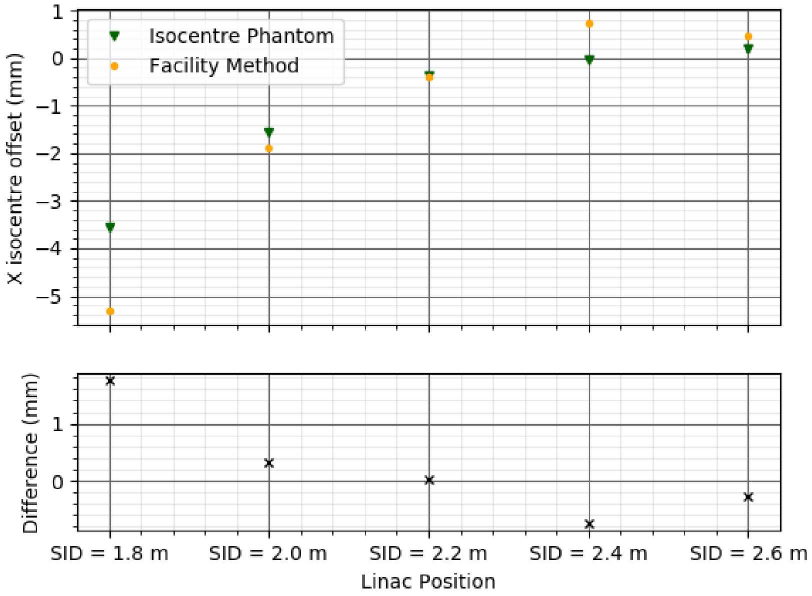

Figure 7.7: Horrizontal (x-axis) beam alignment for Linatron positions 1 - 5. X isocentre offset refers to the x-direction component (as defined in Fig 7.1) of the vector distance between the MRI imaging isocentre and the MV beam CAX

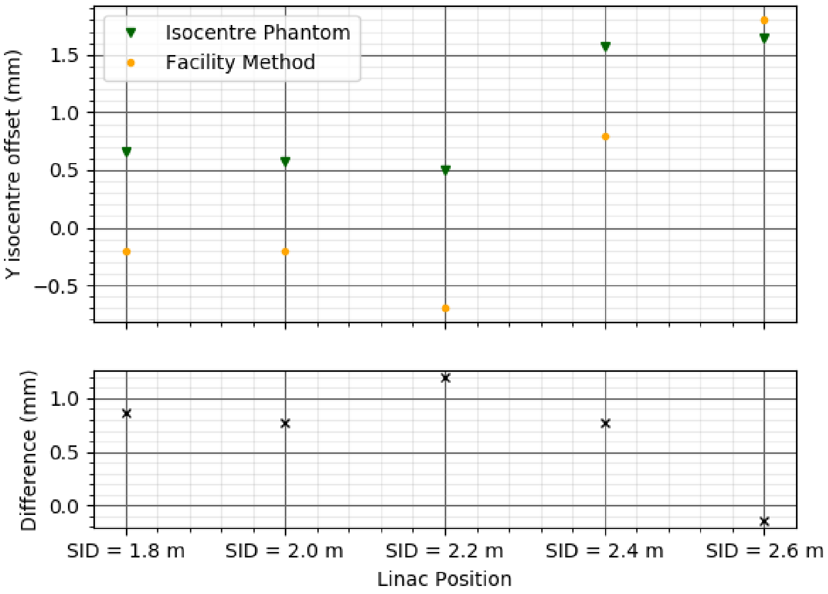

Figure 7.8: Verticle (y-axis) beam alignment for Linatron positions 1 - 5. Y isocentre offset refers to the y-direction component (as defined in Fig 7.1) of the vector distance between the MRI imaging isocentre and the MV beam CAX

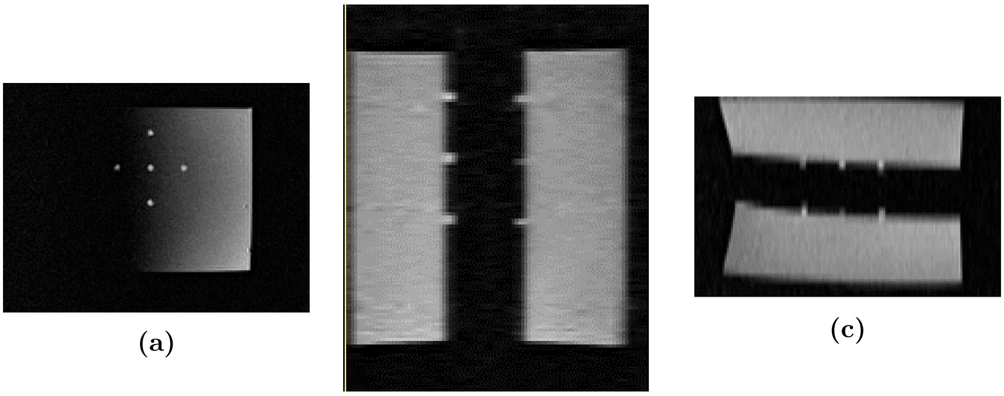

(a)

(b)

(c)

Figure 7.9: MR Images of Isocenter QA device Left: axial slice Middle: sagittal slice Right: coronal slice.

Linatron position 1 and a 1.2 mm difference in the y axis offset at Linatron position 3.

7.4 Preliminary Device testing on a Elekta Unity MRI Linac

The MP512 Isocentre Phantom was designed specifically to meet the isocentre QA requirements of the Australian MRI Linac, however with this is not currently a commercial MRI Linac system. The MRI Linacs that have been commercialised and are currently being utilised clinically differ from the Australian MRI Linac in that they have the linac mounted perpendicular to B_0 field direction and the linac rotates around the patient. Preliminary testing is presented of the novel QA device on a Elekta Unity MRI Linac to determine if design modifications are required for use on commercial MRI Linac systems.

7.4.1 Method

Using the MP512 Isocentre Phantom two plans were created on two separate CT datasets of the iso phantom with the isocentre of the plans located at the centre of the MP512 detector location [see Fig 7.11]. Two separate plans were required due to the plane of the detector needing to be changed for the $0^o/180^o$ beams and the $90^o/270^o$ beams to position the detector orthogonal to the beam direction. Each plans had two 20 mm × 20 mm, 200MU beams. The external trigger diode had to be positioned within the beam for each irradiation angle to trigger the detectors data acquisition system, phantom setup is shown in Fig. 7.12 for gantry 90° measurement. The detector was irradiated from each beam angle three times. The “adapt to

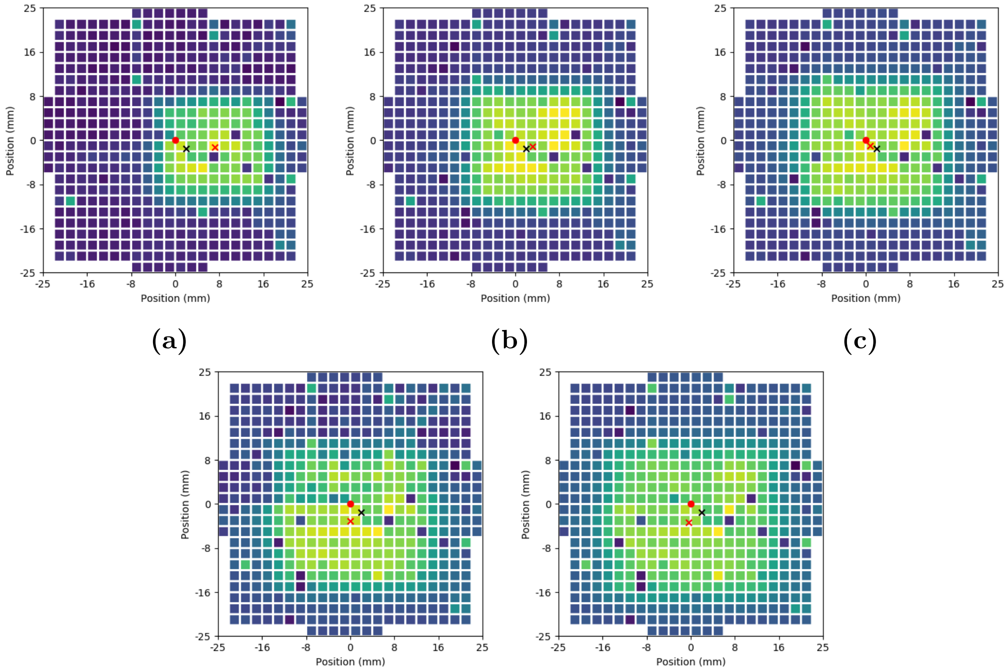

(a) **(b)** **(c)**

(d) **(e)**

Figure 7.10: (a) - (e) Beam's eye view of symmetric field about CAX as acquired by the MP512 for linatron positions 1 to 5 respectively (field size increases due to beam divergence for positions 2-5). Red dot indicates laser position (centre of the phatom), black cross indicates the imaging isocentre and the red cross in the calculated beam central axis.

position" clinical workflow was used for the measurements, a pre-treatment MRI is captured and an image match to the planning CT dataset is performed. The "adapt to position" workflow is used as this maintains the planning segment shapes.

7.4.2 Data processing

A subtraction of background signal was performed for each channel for every measurement and is sampled prior to each measurement. The 2D dose maps were normalised with respect to the maximum response within each measurement. The centre of the measured 2D dose maps was determined using the centre of the FWHM. The centre of the phantom within the MRI dataset was determined using the 10 fiducial markers located around the MP512 detector. The location of the phantom relative to the imaging isocentre was determined from the pre-treatment image match.

7.4.3 Results

The results of the beam central axis relative to the imaging defined centre in the plane orthogonal to the beam direction for gantry $0^o/180^o$ is given in table 7.1. The

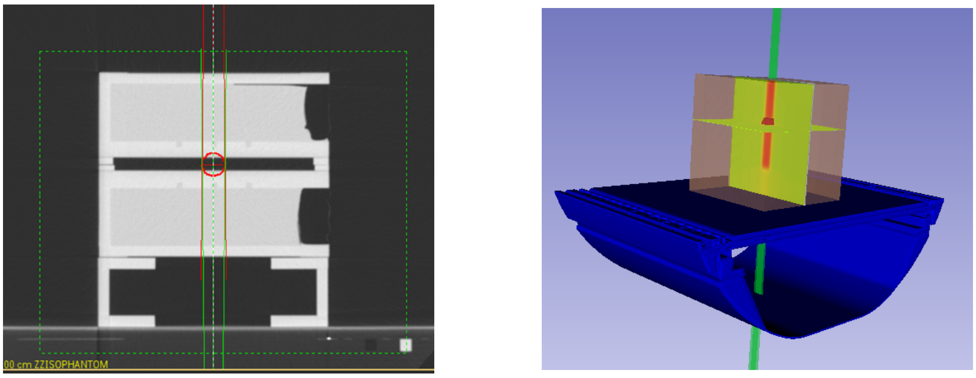

(a) (b)

Figure 7.11: (a) axial slice of CT planning dataset for $0^o/180^o$ beam angle, the dataset does not contain the detector. (b) 3D display of $0^o/180^o$ beam angle plan

Gantry 0°	Gantry 180°
X offset: 1.43 mm	X offset: 0.96 mm
Y offset: 1.27 mm	Y offset: 1.04 mm

Table 7.1: The quantification of the radiation isocentre accuracy by imaging the phantom location and 2D dose maps measured in phantom with MP512 for Gantry 0^o and 180^o.

results for gantry 90^o and 270^o are not given due to an "adapt to shape" workflow being inadvertently used during the experimental procedure. The 2D measured dose maps for gantry 90^o and 270^o are shown in Fig. 7.14(a) and 7.14(c) respectively. The measured beam offset for the gantry 0° and 180° was larger than expected and there is likely a number of contributing factors to the result. The offset between the MP512 detector elements and the imaging fiducials has not been accounted for in this measurement due to difficultly accurately determining the offset. The trigger diode had to be moved between the paired beam angles (0°/180°) and placed at the beam entrance as it was not recieving enough dose to trigger on the beam exit side of the phantom, the phantom may have been bumped during this process. The detector is surrounded by PMMA and an air gap directly above the detector element, due to the perpendicular configuration MV beam relative to the B_0 magnetic field of the Unity system, the dose profiles will be shifted asymmetrically relative to the beam fluence.

7.5 Conclusion

The MP512 Isocentre Phantom has been used at the Australian MRI Linac to measure the relative position of the imaging, optical and radiation isocentre for Linatron positions one to five. The results were compared to meaurements made by the Australian MRI Linac staff, using their in-house developed phantom and measurement

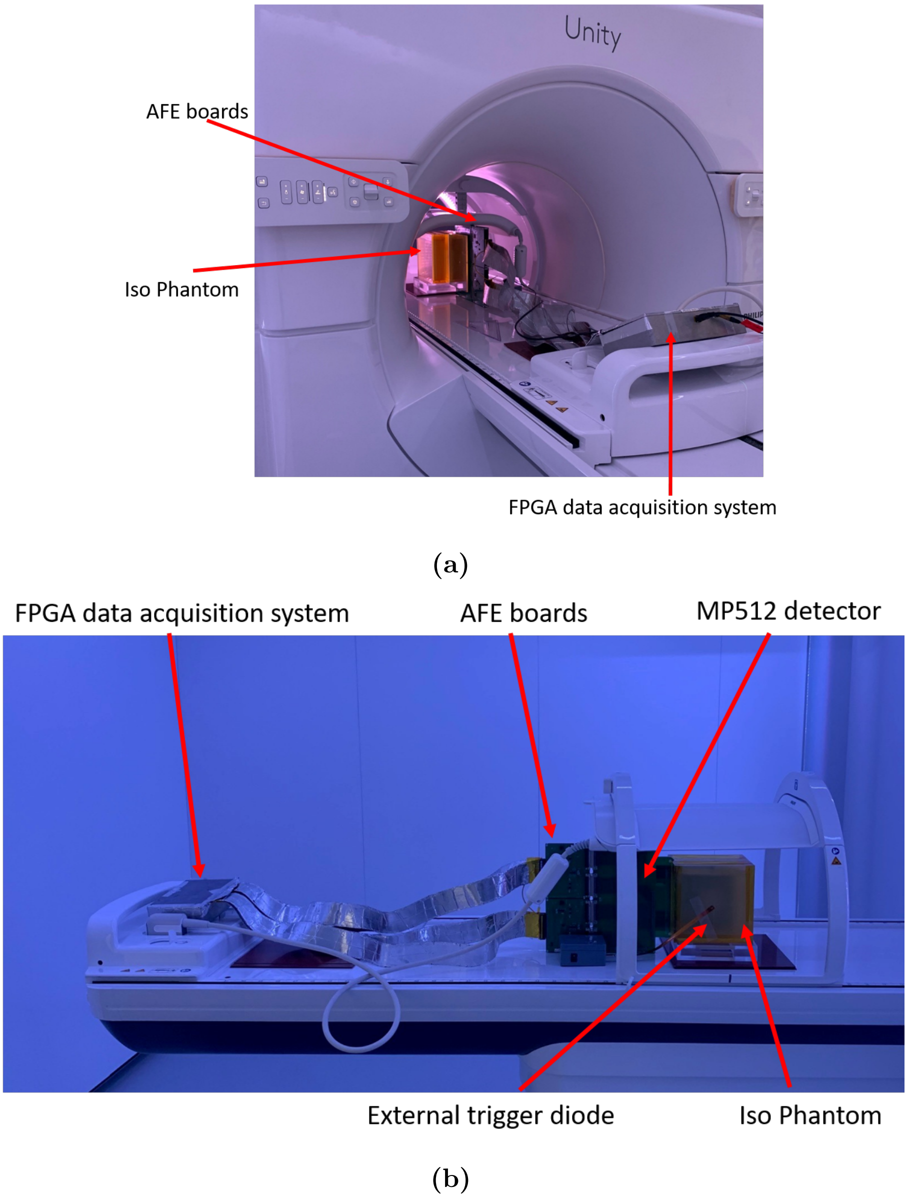

Figure 7.12: (a) Photo of the phantom setup inside the bore of the UNITY for the gantry $90^o/270^o$ measurements. (b) Photo of the phantom setup outside the bore of the UNITY for the gantry $90^o/270^o$ measurements. AFE - analog front end, FPGA - field programmable gate array

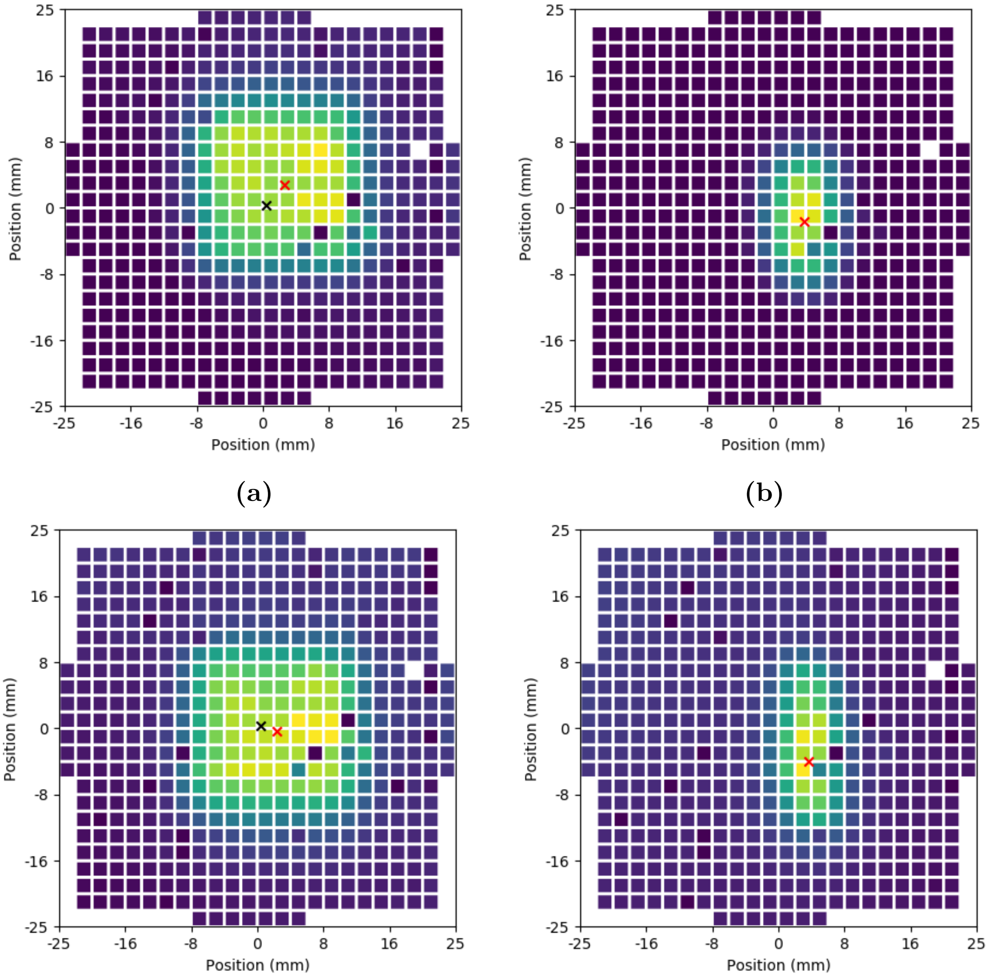

(a)

(b)

(c)

(d)

Figure 7.13: 2D dose maps measured in phantom with MP512 on the Unity, (a) 0° (b) 90° (c) 180° (d) 270°, the 90° and 270° fields are no longer 20 mm x 20 mm due to an adapt to shape workflow being inadvertently used during the experimental procedure. Black cross indicates imaging isocenter, red cross indicates the calculated beam central axis

technique. The device is simple to setup and quick to use however uncertainty in the manufacturing of the device could be improved, which may result in tighter agreement between the two measurement methods. A preliminary measurement using the MP512 Isocentre Phantom of imaging and radiation isocentre coincidence of an Elekta Unity has been presented. The MR Imaging of the phantom with the agar gel was successful and the MP512 detector with an external trigger diode successfully measured 2D dose distributions that were used to identify the MV beam central dose axis. However since the dose is perturbed dose to the perpendicular magnetic field, the central axis of the MV beams fluence will not be aligned with the central axis of the dose distribution. This measurement has been used to identify design changes that are required to adapt the device to suit commercial MRI Linacs where the B_0 magnetic field is perpendicular to the MV beam. The required modifications include the use of an electron dense material around the detector to minimise the offset between beam fluence profile and dose profile as suggested by Zijp et al [122]. Also incorporating multiple detector planes would remove the need to setup the detector in multiple planes, reducing the measurement time and reducing the added uncertainty introduced by the multiple setups.

Chapter 8

Discussion, Conclusion and Future Research

This thesis has presented a body of work investigating the application of a radiation detector system developed at the Centre for Medical Radiation Physics to quality assurance measurements of MRI guided x-ray and proton radiotherapy beams. The detector system is novel in design using a modular readout electronics with ion implanted monolithic silicon detector arrays (sDMG-256A, DUO, MP512) to provide superior spatial and temporal resolution in comparison to commercially available radiation array detectors. Following are the key results of this thesis, stated in terms of the aims:

Aim 1. Determine an experimental method to experimentally investigate the effect of a magnetic field on the response of dosimetry system for varying magnetic field strength and orientations relative to the incident radiation beam direction.

Chapter 3 reports on the design, construction and magnetic field verification of a Portable Magnetic Field Apparatus for Radiation Dosimetry Studies (MARDOS). The apparatus employs an adjustable iron yoke and magnetic field focusing cones. The apparatus utilises two $Nd_2Fe_{14}B$ permanent magnet banks totalling around 50 kg in mass to generate a magnetic field across the pole gap. The yoke design allows adjustment of the pole gap and exchanging of the focusing cones. Further to this, beam portal holes are present in the yoke and focusing cones, allowing for radiation beams of up to 5×5 cm^2 to pass through the region of high magnetic field between the focusing cone tips. Finite element magnetic modelling has been performed to predict the performance of the device, along with automated physical measurements of the magnetic field components at various locations. The adjustable pole gap and interchangeable cones allows rapid changing of the experimental set-up to allow different styles of measurements to be performed. A mostly uniform magnetic field of 1.2 T can be achieved over a volume of at least $3 \times 3 \times 3$ cm^3. This can be reduced in strength to 0.3 T but increased in volume to $10 \times 10 \times 10$ cm^3 via removal of the cone tips and/or adjustment of the iron yoke. Although small, these volumes are sufficient to house radiation detectors, cell culture dishes and various phantom arrangements targeted at examining small radiation field dosimetry inside magnetic field strengths that can be changed with ease. Most important is the ability to align the magnetic field both perpendicular to, or inline with the radiation beam.

Since the construction and characterisation of MARDOS, the device has been employed in a number of scientific studies that the author has contributed to the planning of the experimental work and with the devices use. These studies include the experimental verification of dose enhancement effects in a lung phantom from inline magnetic fields lead by Oborn et al, detector studies by Alnaghy et al and Gargett et al as well as a recent investigation of measurement and simulation of clinical electron beams in magnetic fields by Kueng et al [99, 104, 140, 141].

Aim 2. Experimentally characterise the radiation detector properties, including the effects of a strong magnetic field on a monolithic silicon array dosimeter proposed for use in quality assurance of radiation beam properties of MRI-guided radiotherapy systems.

Chapter 4 reports on the dosimetric characterisation of a monolithic silicon strip detector the sDMG256A, mounted to a flexible polymide (Kapton) printed circuit board. The detector was observed to have a linear response ($R^2 = 1$) over the range 20-1000 cGy. The dose per pulse response was investigated with an observed 10.3% variation over the range of (0.29×10^{-4} to 4.65×10^{-4}) Gy/pulse. The angular response of the sDMG-256A showed a less than 2% variation from $\pm45^o$ beam incidence, rapidly increasing to 20% for the central detector in the array for beam incidence of 90^o and 270^o as a result of the roughly 2.5 cm of silicon in the beam path for these angles. The uniformity of detector channel response was shown to be within 0.2% after normalisation to a uniform flood field. The effect of detector packaging design in a 1.2 T transverse magnetic field was investigated. A small air gap above the detector is currently required to protect the monolithic silicon array and its wire bonds. Decreasing the size of the air gap resulted in the difference in measured small field output factor with and without the magnetic field decreasing. Unfortunately the case of no air gap was unable to be tested due to risk of crushing the wire bonds. The high spatial and temporal properties of the sDMG256A would be beneficial for small field dosimetry in a MRI-Linac system however the small air gap in the packaging around the wire bonds is causing the detector response to small fields to vary relative to machine output factor. The detector would therefore require field size dependent output factor corrections for use with an MRI-Linac. To reduce the small field output dependence in a magnetic of the sDMG256A the air gaps around the wire bonds and above the detector need to be removed from the detector packaging, this is a challenge as the air gap is mechanically protecting the delicate wire bonds of the detector.

Aim 3. Use a monolithic silicon array dosimeter to measure therapeutic quality proton beams in a magnetic field environment that is representative of feasibly future real-time MRI-guided proton therapy systems.

Chapter 5 reports the experimental results of a high spatial resolution silicon-based detector (DUO) exposed to therapeutic quality proton beams in a 0.95 T transverse magnetic field. These experimental results are important for the development of accurate and novel dosimetry methods in future potential real-time MRI-guided proton therapy systems. A permanent magnet device was utilised to generate a 0.50 T - 0.95 T magnetic field over a $15 \times 20 \times 4$ cm^3 volume. Within this volume, a high-resolution silicon diode array detector was positioned inside a PMMA phantom. This detector contains two orthogonal strips containing 505 sensitive volumes spaced at 0.2 mm apart. Proton beams collimated to a circle of 10 mm diameter with nominal energies of 90 MeV, 110 MeV, and 125 MeV were incident on the detector from an edge-on orientation. This allows for a measurement of the Bragg peak at 0.2 mm spatial resolution in both the depth and lateral profile directions. The impact of the magnetic field on the proton beams, that is, a small deflection was also investigated. A Geant4 Monte Carlo simulation was performed of the experimental setup to aid in interpretation of the results. The nominal Bragg peak for each proton energy was successfully observed with a 0.2 mm spatial resolution in the 0.95 T transverse magnetic field in both a depth and lateral profiles. The proton beam deflection (at 0.95 T) was a consistent 2 ± 0.5 mm at the centre of the magnetic volume for each beam energy. However, a pristine Bragg peak was not observed for each energy. This was caused by the detector packaging having small air gaps between layers of the phantom material surrounding the diode array. These air gaps act to degrade the shape of the Bragg peak, and further to this, the non-water equivalent silicon chip acts to separate the Bragg peak into multiple peaks depending on the proton path taken. Overall, a promising performance of the silicon detector array was observed, however, with a qualitative assessment rather than a robust quantitative dosimetric evaluation at this stage of development. Future efforts will benefit from improving the detector packaging to reduce the Bragg peaks caused by the proton paths through different combinations of detector packaging materials. A successful phantom design will the allow the application of the high spatial and temporal properties of CMRP monolithic silicon detectors to the conduct further targeted research into the unique dosimetry requirements anticipated in future efforts towards MRI-guided proton therapy.

Aim 4. Design a quality assurance device utilising the high spatial resolution of monolithic silicon array detectors to characterise the spatial relationship of the optical, MR imaging and radiation isocentre of MRI-linac systems.

In Chapter 6, the development and testing of a prototype QA device for measurement of the optical, MR imaging and radiation isocentre of inline MRI-linac systems was performed. The prototype used the sDMG-256A detector for measurement of radiation beam centre, the proposed process was compared to Winston-Lutz method of isocentre measurement on a conventional Varian 2100iX linear accelerator using CBCT for the volumetric imaging. Initial testing of the prototype at the Australian MRI linac identified shortcoming with the initial prototype including the sensitive volumes of the sDMG-256 diodes are not large enough to measure a usable radiation profile with the radiation source of the Australian MRI linac. The volume of MR sensitive material in the initial prototype was also such that a head coil was required for MR imaging. Both of these issues were addressed in the final design, the sDMG-256A detector was swapped for the MP512 with larger sensitive volumes and a 512 x 512 2D array configuration and the volume of MR visible material was increased. In Chapter 7 the isocenter QA device developed in Chapter 6 was used to characterise the spatial relationship of the optical, MR imaging and radiation isocentre of the Australian MRI-linac system.

8.1 Future work

There are a number of studies outlined in this thesis that will benefit from future investigation or aid in future studies. The portable magnet apparatus was conceptualised with the goal of providing an MRI-linac like magnetic environment where measurements can be repeated without the magnetic field for radiation detector characterisation, radiation dosimetry and in-vivo radiobiology studies. To date the magnetic apparatus has found use in detector characterisation and radiation dosimetry studies, however has not yet been used for radiobiological studies. The apparatus is ideally suited for in-vivo radiobiology studies into the effects of a strong magnetic field during irradiation as it allows for experiments to be performed with varying magnetic field strengths, in both inline and crossline field orientation relative to the radiation source and unlike similar electromagnet apparatus without heat generation that may affect in-vivo cell studies.

The preliminary study into the application of a high spatial resolution silicon-based detector to measure Bragg peak locations of therapeutic quality proton beams in a 0.95 T transverse magnetic field further reiterated the conclusion from the detector characterisation in Chapter 3 that there is a need to remove the air gap from above the monolithic silicon array in the packaging of these detectors. The air gap above the detector is currently a requirement to protect the silicon array and fragile wire bonds however is observed to adversely affect the dosimetric performance in the presence of a magnetic field. The measurement of proton beam dosimetric properties using a real time high resolution detector system is an important step towards the clinical implementation of MRI guided proton therapy. Future work to improve the phantom design used in chapter 5 will open up the opportunity to conduct further targeted research into the unique dosimetry requirements anticipated in future efforts towards MRI-guided proton therapy.

The isocenter QA device developed in Chapter 6 and compared with the current Australian MRI-Linac facility procedure in Chapter 7 works for its intended purpose in its current design and offers advantages over the facilities procedure such as significant time savings. However the design is currently limited to inline MRI-Linacs where the beam fluence and dose are expected to have a coincident central axis. For the case of the current commercial MRI-linacs such as the Unity and the Viewray where the beam is perpendicular to the direction of magnetic field and the dose is asymmetrically perturbed from the fluence, the QA device would not accurately determine the location of the beam fluence. The preliminary measurement on an Elekta Unity presented in Chapter 7 demonstrated that further work is required to improve the performance of the isocenter QA device for application in commercial MRI-linacs include, again the removal of the air gap above the detector and to add a region of high z material immediately around the detector to reduce the pathlength of the secondary dose depositing electrons. The device also shows potential for QA vertification of small radiation fields delivered on MRI-Linacs for stereotactic fields where spatial position is as critical as radiation dose. This device can potentially validate both. On this journey the author worked with a prototype magnet then the prototype MRI-Linac device and near the end of this journey commercial clinical MRI-Linacs have become a reality. It is hoped this further validates the usefullness of these pioneering experiments.

Bibliography

[1] F. Bray, J. Ferlay, I. Soerjomataram, R. L. Siegel, L. A. Torre, and A. Jemal, "Global cancer statistics 2018: GLOBOCAN estimates of incidence and mortality worldwide for 36 cancers in 185 countries," *CA: A Cancer Journal for Clinicians*, vol. 68, no. 6, pp. 394–424, 2018.

[2] AIHW, "Cancer in Australia 2019," Tech. Rep., 2019.

[3] M. Barton *et al.*, "Review of optimal radiotherapy utilisation rates," *Collaboration for Cancer Outcomes Research and Evaluation*, 2013.

[4] V. Ahern *et al.*, "Particle Therapy in Australia: iacta alea est!" *Journal of Medical Imaging and Radiation Oncology*, vol. 64, no. 5, pp. 679–681, 2020.

[5] P. Munro, "Portal imaging technology: Past, present, and future," *Seminars in Radiation Oncology*, vol. 5, no. 2, pp. 115–133, 1995.

[6] J. Wong and H. Meertens, "A Review of Electronic Portal Imaging Devices (Epids)," *Medical Physics*, vol. 19, no. 1, pp. 1–16, 1992.

[7] D. A. Jaffray, J. H. Siewerdsen, J. W. Wong, and A. A. Martinez, "Flat-panel cone-beam computed tomography for image-guided radiation therapy," *International Journal of Radiation Oncology Biology Physics*, vol. 53, no. 5, pp. 1337–1349, 2002.

[8] P. Bhatnagar, M. Subesinghe, C. Patel, R. Prestwich, and A. F. Scarsbrook, "Functional imaging for radiation treatment planning, response assessment, and adaptive therapy in head and neck cancer," *Radiographics*, vol. 33, no. 7, pp. 1909–1929, 2013.

[9] T. T. Pham, G. P. Liney, K. Wong, and M. B. Barton, "Functional MRI for quantitative treatment response prediction in locally advanced rectal cancer," *The British Journal of Radiology*, vol. 90, no. 1072, p. 20 151 078, 2017.

[10] U. A. van der Heide, A. C. Houweling, G. Groenendaal, R. G. Beets-Tan, and P. Lambin, "Functional MRI for radiotherapy dose painting," *Magnetic Resonance Imaging*, vol. 30, no. 9, pp. 1216–1223, 2012.

[11] J. J. W. Lagendijk and C. J. G. Bakker, “MRI guided radiotherapy: a MRI based linear accelerator,” in *Radiotherapy and Oncology*, vol. 56, 2000, S60.

[12] M. Karlsson, M. G. Karlsson, T. Nyholm, C. Amies, and B. Zackrisson, “Dedicated Magnetic Resonance Imaging in the Radiotherapy Clinic,” *International Journal of Radiation Oncology Biology Physics*, vol. 74, no. 2, pp. 644–651, 2009.

[13] D. A. Jaffray *et al.*, “A Facility for Magnetic Resonance-Guided Radiation Therapy,” *Seminars in Radiation Oncology*, vol. 24, no. 3, pp. 193–195, 2014.

[14] S. Mutic and J. F. Dempsey, “The ViewRay System: Magnetic Resonance–Guided and Controlled Radiotherapy,” *Seminars in Radiation Oncology*, vol. 24, no. 3, pp. 196–199, 2014.

[15] S. Klüter, “Technical design and concept of a 0.35 T MR-Linac,” *Clinical and Translational Radiation Oncology*, vol. 18, pp. 98–101, 2019.

[16] A. J. Raaijmakers, B. W. Raaymakers, S. Van Der Meer, and J. J. Lagendijk, “Integrating a MRI scanner with a 6 MV radiotherapy accelerator: Impact of the surface orientation on the entrance and exit dose due to the transverse magnetic field,” *Physics in Medicine and Biology*, vol. 52, no. 4, pp. 929–939, 2007.

[17] B. W. Raaymakers *et al.*, “First patients treated with a 1.5 T MRI-Linac: Clinical proof of concept of a high-precision, high-field MRI guided radiotherapy treatment,” *Physics in Medicine and Biology*, vol. 62, no. 23, pp. L41–L50, 2017.

[18] B. G. Fallone *et al.*, “First MR images obtained during megavoltage photon irradiation from a prototype integrated linac-MR system,” *Medical Physics*, vol. 36, no. 6 Part1, pp. 2084–2088, 2009.

[19] B. G. Fallone, “The Rotating Biplanar Linac–Magnetic Resonance Imaging System,” *Seminars in Radiation Oncology*, vol. 24, no. 3, pp. 200–202, 2014.

[20] G. P. Liney *et al.*, “Technical Note: Experimental results from a prototype high-field inline MRI-linac,” *Medical Physics*, vol. 43, no. 9, pp. 5188–5194, 2016.

[21] G. P. Liney *et al.*, “Technical Note: The first live treatment on a 1.0 Tesla inline MRI-linac,” *Medical Physics*, vol. 46, no. 7, pp. 3254–3258, 2019.

[22] T. R. MacKie, A. F. Bielajew, D. W. Rogers, and J. J. Battista, “Generation of photon energy deposition kernels using the EGS Monte Carlo code,” *Physics in Medicine and Biology*, vol. 33, no. 1, pp. 1–20, 1988.

[23] A. J. Raaijmakers, B. W. Raaymakers, and J. J. Lagendijk, “Magnetic-field-induced dose effects in MR-guided radiotherapy systems: Dependence on the magnetic field strength,” *Physics in Medicine and Biology*, vol. 53, no. 4, pp. 909–923, 2008.

[24] B. W. Raaymakers, A. J. E. Raaijmakers, A. N. T. J. Kotte, D Jette, and J. J. W. Lagendijk, “Integrating a MRI scanner with a 6 MV radiotherapy accelerator: dose deposition in a transverse magnetic field,” *Physics in Medicine and Biology*, vol. 49, no. 17, pp. 4109–4118, 2004.

[25] A. J. E. Raaijmakers, B. W. Raaymakers, and J. J. W. Lagendijk, “Integrating a MRI scanner with a 6 MV radiotherapy accelerator: Dose increase at tissue-air interfaces in a lateral magnetic field due to returning electrons,” *Physics in Medicine and Biology*, vol. 50, no. 7, pp. 1363–1376, 2005.

[26] A. J. Raaijmakers, B. W. Raaymakers, and J. J. Lagendijk, “Experimental verification of magnetic field dose effects for the MRI-accelerator,” *Physics in Medicine and Biology*, vol. 52, no. 14, pp. 4283–4291, 2007.

[27] A. J. E. Raaijmakers, B Hårdemark, B. W. Raaymakers, C. P. J. Raaijmakers, and J. J. W. Lagendijk, “Dose optimization for the MRI-accelerator: IMRT in the presence of a magnetic field,” *Physics in Medicine and Biology*, vol. 52, no. 23, pp. 7045–7054, 2007.

[28] C. Kirkby, T. Stanescu, S. Rathee, M. Carlone, B. Murray, and B. G. Fallone, “Patient dosimetry for hybrid MRI-radiotherapy systems,” *Medical Physics*, vol. 35, no. 3, pp. 1019–1027, 2008.

[29] ICRU, “Determination of Dose Equivalents Resulting from External Radiation Sources (Report 39),” Tech. Rep., 1985.

[30] B. M. Oborn, P. E. Metcalfe, M. J. Butson, and A. B. Rosenfeld, “High resolution entry and exit Monte Carlo dose calculations from a linear accelerator 6 MV beam under the influence of transverse magnetic fields,” *Medical Physics*, vol. 36, no. 8, pp. 3549–3559, 2009.

[31] B. M. Oborn, P. E. Metcalfe, M. J Butson, and A. B. Rosenfeld, “Monte carlo characterization of skin doses in 6 MV transverse field MRI-linac systems: Effect of field size, surface orientation, magnetic field strength, and exit bolus,” *Medical Physics*, vol. 37, no. 10, pp. 5208–5217, 2010.

[32] A. F. Bielaiew, “The effect of strong longitudinal magnetic fields on dose deposition from electron and photon beams,” *Medical Physics*, vol. 20, no. 4, pp. 1171–1179, 1993.

[33] W. R. Nelson, H Hirayama, and D. W. Rogers, “EGS4 code system,” Dec. 1985.

[34] S. W. Ramahi, S. A. Naqvi, and J. Chu, "Achieving a smaller penumbra region for better planning in conformal radiotherapy by using a longitudinal magnetic field," *Annual International Conference of the IEEE Engineering in Medicine and Biology - Proceedings*, vol. 4, pp. 3260–3263, 2000.

[35] D. W. Litzenberg *et al.*, "An apparatus for applying strong longitudinal magnetic fields to clinical photon and electron beams," *Physics in Medicine and Biology*, vol. 46, no. 5, N105–N115, 2001.

[36] C. Kirkby, B. Murray, S. Rathee, and B. G. Fallone, "Lung dosimetry in a linac-MRI radiotherapy unit with a longitudinal magnetic field," *Medical Physics*, vol. 37, no. 9, pp. 4722–4732, 2010.

[37] B. M. Oborn, P. E. Metcalfe, M. J. Butson, A. B. Rosenfeld, and P. J. Keall, "Electron contamination modeling and skin dose in 6 MV longitudinal field MRIgRT: Impact of the MRI and MRI fringe field," *Medical Physics*, vol. 39, no. 2, pp. 874–890, 2012.

[38] A. Keyvanloo *et al.*, "Skin dose in longitudinal and transverse linac-MRIs using Monte Carlo and realistic 3D MRI field models," *Medical Physics*, vol. 39, no. 10, pp. 6509–6521, 2012.

[39] A Keyvanloo *et al.*, "Minimal skin dose increase in longitudinal rotating biplanar linac-MR systems: Examination of radiation energy and flattening filter design," *Physics in Medicine and Biology*, vol. 61, no. 9, pp. 3527–3539, 2016.

[40] A Keyvanloo *et al.*, "Retraction: Minimal skin dose increase in longitudinal rotating biplanar linac-MR systems: Examination of radiation energy and flattening filter design (2016 phys. med. biol. 61 3527)," *Physics in Medicine & Biology*, vol. 65, no. 7, p. 079 701, 2020.

[41] B. W. Raaymakers, A. J. E. Raaijmakers, and J. J. W. Lagendijk, "Feasibility of MRI guided proton therapy: magnetic field dose effects," *Physics in Medicine and Biology*, vol. 53, no. 20, pp. 5615–5622, 2008.

[42] R. Wolf and T. Bortfeld, "An analytical solution to proton bragg peak deflection in a magnetic field," *Physics in Medicine and Biology*, vol. 57, no. 17, N329–N337, 2012.

[43] B. M. Oborn, S. Dowdell, P. E. Metcalfe, S. Crozier, R. Mohan, and P. J. Keall, "Proton beam deflection in MRI fields: Implications for MRI-guided proton therapy," *Medical Physics*, vol. 42, no. 5, pp. 2113–2124, 2015.

[44] S. M. Schellhammer and A. L. Hoffmann, “Prediction and compensation of magnetic beam deflection in MR-integrated proton therapy: a method optimized regarding accuracy, versatility and speed,” *Physics in Medicine and Biology*, vol. 62, no. 4, pp. 1548–1564, 2017.

[45] J Hartman *et al.*, “Dosimetric feasibility of intensity modulated proton therapy in a transverse magnetic field of 1.5 T,” *Physics in Medicine and Biology*, vol. 60, no. 15, pp. 5955–5969, 2015.

[46] H. Fuchs, P. Moser, M. Gröschl, and D. Georg, “Magnetic field effects on particle beams and their implications for dose calculation in MR-guided particle therapy,” *Medical physics*, vol. 44, no. 3, pp. 1149–1156, 2017.

[47] M. Moteabbed, J. Schuemann, and H. Paganetti, “Dosimetric feasibility of real-time MRI-guided proton therapy,” *Medical Physics*, vol. 41, no. 11, p. 111 713, 2014.

[48] C. Kurz *et al.*, “A Monte-Carlo study to assess the effect of 1.5 T magnetic fields on the overall robustness of pencil-beam scanning proton radiotherapy plans for prostate cancer,” *Physics in Medicine and Biology*, vol. 62, no. 21, pp. 8470–8482, 2017.

[49] F. Padilla-Cabal, D. Georg, and H. Fuchs, “A pencil beam algorithm for magnetic resonance image-guided proton therapy,” *Medical Physics*, vol. 45, no. 5, pp. 2195–2204, 2018.

[50] B. M. Oborn, S. Dowdell, P. E. Metcalfe, S. Crozier, R. Mohan, and P. J. Keall, “Future of medical physics: Real-time MRI-guided proton therapy,” *Medical Physics*, vol. 44, no. 8, e77–e90, 2017.

[51] S. M. Schellhammer *et al.*, “Integrating a low-field open MR scanner with a static proton research beam line: proof of concept,” *Physics in Medicine & Biology*, vol. 63, no. 23, 23LT01, 2018.

[52] B. W. Raaymakers *et al.*, “Integrating a 1.5 T MRI scanner with a 6 MV accelerator: Proof of concept,” *Physics in Medicine and Biology*, vol. 54, no. 12, N229–N237, 2009.

[53] I Meijsing *et al.*, “Dosimetry for the MRI accelerator: the impact of a magnetic field on the response of a Farmer NE2571 ionization chamber.,” *Physics in medicine and biology*, vol. 54, no. 10, pp. 2993–3002, 2009.

[54] K Smit, B van Asselen, J. G. M. Kok, A. H. L. Aalbers, J. J. W. Lagendijk, and B. W. Raaymakers, “Towards reference dosimetry for the MR-linac: Magnetic field correction of the ionization chamber reading,” *Physics in Medicine and Biology*, vol. 58, no. 17, pp. 5945–5957, 2013.

[55] D. J. O'Brien, D. A. Roberts, G. S. Ibbott, and G. O. Sawakuchi, "Reference dosimetry in magnetic fields: formalism and ionization chamber correction factors," *Medical Physics*, vol. 43, no. 8Part1, pp. 4915–4927, 2016.

[56] M. Reynolds, B. G. Fallone, and S. Rathee, "Dose response of selected ion chambers in applied homogeneous transverse and longitudinal magnetic fields," *Medical Physics*, vol. 40, no. 4, p. 042 102, 2013.

[57] C. K. Spindeldreier *et al.*, "Radiation dosimetry in magnetic fields with Farmer-type ionization chambers: Determination of magnetic field correction factors for different magnetic field strengths and field orientations," *Physics in Medicine and Biology*, vol. 62, no. 16, pp. 6708–6728, 2017.

[58] V. N. Malkov and D. W. Rogers, "Monte Carlo study of ionization chamber magnetic field correction factors as a function of angle and beam quality," *Medical Physics*, vol. 45, no. 2, pp. 908–925, 2018.

[59] Glenn G. Knoll, *Radiation Detection and Measurement (4th Edition)*. 2010.

[60] M. Reynolds, B. G. Fallone, and S. Rathee, "Dose response of selected solid state detectors in applied homogeneous transverse and longitudinal magnetic fields," *Medical Physics*, vol. 41, no. 9, p. 092 103, 2014.

[61] M. Reynolds, B. G. Fallone, and S. Rathee., "Technical Note: Response measurement for select radiation detectors in magnetic fields," *Medical Physics*, vol. 42, no. 6, pp. 2837–2840, 2015.

[62] H. H. Li *et al.*, "Patient-specific quality assurance for the delivery of60Co intensity modulated radiation therapy subject to a 0.35-T lateral magnetic field," *International Journal of Radiation Oncology Biology Physics*, vol. 91, no. 1, pp. 65–72, 2015.

[63] A. C. Houweling *et al.*, "Performance of a cylindrical diode array for use in a 1.5 T MR-linac," *Physics in Medicine and Biology*, vol. 61, no. 3, N80–N89, 2016.

[64] J. H. De Vries *et al.*, "Characterization of a prototype MR-compatible Delta4 QA system in a 1.5 tesla MR-linac," *Physics in Medicine and Biology*, vol. 63, no. 2, 02NT02, 2018.

[65] B. Delfs *et al.*, "The 1D lateral dose response functions of photon-dosimetry detectors in magnetic fields - Measurement and Monte-Carlo simulation," *Physics in Medicine and Biology*, vol. 63, no. 19, p. 195 002, 2018.

[66] C. H. Choi, J. M. Park, H. J. An, and J. in Kim, "Effect of low magnetic field on single-diode dosimetry for clinical use," *Physica Medica*, vol. 60, pp. 132–138, 2019.

[67] P. Liengsawangwong, N. Sahoo, X. Ding, M. Lii, M. T. Gillin, and X. R. Zhu, “Dosimetric Characteristics of a Two-Dimensional Diode Array Detector Irradiated with Passively Scattered Proton Beams.,” *Cancers*, vol. 7, no. 3, pp. 1425–35, 2015.

[68] W. D. Newhauser, K. D. Myers, S. J. Rosenthal, and A. R. Smith, “Proton beam dosimetry for radiosurgery: implementation of the ICRU Report 59 at the Harvard Cyclotron Laboratory,” *Physics in Medicine and Biology*, vol. 47, no. 8, pp. 1369–1389, 2002.

[69] E. Grusell, J. Medin, and E. Grusell, “General characteristics of the use of silicon diode detectors for clinical dosimetry in proton beams,” *Physics in Medicine and Biology*, vol. 45, p. 2573, 9 Sep. 2000.

[70] S Onori *et al.*, “Dosimetric characterization of silicon and diamond detectors in low-energy proton beams,” *Physics in Medicine and Biology*, vol. 45, no. 10, pp. 3045–3058, 2000.

[71] F. Bisello, D. Menichelli, M. Scaringella, M. Zani, and M. Bucciolini, “Development of silicon monolithic arrays for dosimetry in external beam radiotherapy,” *Nuclear Instruments and Methods in Physics Research Section A: Accelerators, Spectrometers, Detectors and Associated Equipment*, vol. 796, pp. 85–88, 2015.

[72] P. Wang *et al.*, “Proton computed tomography using a 1D silicon diode array,” *Medical Physics*, vol. 43, no. 10, pp. 5758–5766, 2016.

[73] A. Merchant *et al.*, “Feasibility study of a novel multi-strip silicon detector for use in proton therapy range verification quality assurance,” *Radiation Measurements*, vol. 106, pp. 378–384, 2017.

[74] A. J. Wroe *et al.*, “Initial testing of a pixelated silicon detector prototype in proton therapy,” *Journal of Applied Clinical Medical Physics*, vol. 18, no. 5, pp. 315–324, 2017.

[75] G. A. McAuley, A. V. Teran, J. D. Slater, J. M. Slater, and A. J. Wroe, “Evaluation of the dosimetric properties of a diode detector for small field proton radiosurgery,” *Journal of Applied Clinical Medical Physics*, vol. 16, pp. 51–64, 6 2015.

[76] A. Niroomand-Rad *et al.*, “Radiochromic film dosimetry: Recommendations of AAPM Radiation Therapy Committee Task Group 55,” *Medical Physics*, vol. 25, no. 11, pp. 2093–2115, 1998.

[77] M. L. Reyhan, T. Chen, and M. Zhang, “Characterization of the effect of MRI on Gafchromic film dosimetry,” *Journal of Applied Clinical Medical Physics*, vol. 16, no. 6, pp. 325–332, 2015.

[78] F. J. Reynoso, A. Curcuru, O. Green, S. Mutic, I. J. Das, and L. Santanam, “Technical Note: Magnetic field effects on Gafchromic-film response in MR-IGRT,” *Medical Physics*, vol. 43, no. 12, pp. 6552–6556, 2016.

[79] Y. Roed, H. Lee, L. Pinsky, and G. Ibbott, “PO-0763: Characterizing the response of Gafchromic EBT3 film in a 1.5 T magnetic field,” *Radiotherapy and Oncology*, vol. 123, S403, 2017.

[80] B. Delfs *et al.*, “Magnetic fields are causing small, but significant changes of the radiochromic EBT3 film response to 6 MV photons,” *Physics in Medicine and Biology*, vol. 63, no. 3, p. 035 028, 2018.

[81] D. L. Barten, D. Hoffmans, M. A. Palacios, S. Heukelom, and L. J. Van Battum, “Suitability of EBT3 GafChromic film for quality assurance in MR-guided radiotherapy at 0.35 T with and without real-time MR imaging,” *Physics in Medicine and Biology*, vol. 63, no. 16, p. 165 014, 2018.

[82] F. Padilla-Cabal, P. Kuess, D. Georg, H. Palmans, L. Fetty, and H. Fuchs, “Characterization of EBT3 radiochromic films for dosimetry of proton beams in the presence of magnetic fields,” *Medical Physics*, vol. 46, no. 7, pp. 3278–3284, 2019.

[83] O. Volotskova, X. Fang, M. Keidar, H. Chandarana, and I. J. Das, “Microstructure changes in radiochromic films due to magnetic field and radiation,” *Medical Physics*, vol. 46, no. 1, pp. 293–301, 2019.

[84] A. Darafsheh, Y. Hao, B. Maraghechi, J. Cammin, F. J. Reynoso, and R. Khan, “Influence of 0.35 T magnetic field on the response of EBT3 and EBT-XD radiochromic films,” *Medical Physics*, vol. 47, no. 9, pp. 4543–4552, 2020.

[85] “Radiographic film dosimetry of proton beams for depth-dose constancy check and beam profile measurement,” *Journal of Applied Clinical Medical Physics*, vol. 16, pp. 318–328, 3 May 2015.

[86] R. Castriconi *et al.*, “Dose–response of ebt3 radiochromic films to proton and carbon ion clinical beams,” *Physics in Medicine and Biology*, vol. 62, p. 377, 2 Dec. 2016.

[87] S. M. Schellhammer, S. Gantz, A. Lühr, B. M. Oborn, M. Bussmann, and A. L. Hoffmann, “Technical Note: Experimental verification of magnetic field-induced beam deflection and Bragg peak displacement for MR-integrated proton therapy,” *Medical Physics*, vol. 45, no. 7, pp. 3429–3434, 2018.

[88] A. Lühr, L. N. Burigo, S. Gantz, S. M. Schellhammer, and A. L. Hoffmann, "Proton beam electron return effect: Monte Carlo simulations and experimental verification," *Physics in Medicine and Biology*, vol. 64, no. 3, p. 035 012, 2019.

[89] J. H. D. Wong *et al.*, "A silicon strip detector dose magnifying glass for IMRT dosimetry," *Medical Physics*, vol. 37, no. 2, pp. 427–439, 2010.

[90] J. H. Wong *et al.*, "The use of a silicon strip detector dose magnifying glass in stereotactic radiotherapy QA and dosimetry," *Medical Physics*, vol. 38, no. 3, pp. 1226–1238, 2011.

[91] E. Debrot, M. Newall, S. Guatelli, M. Petasecca, N. Matsufuji, and A. B. Rosenfeld, "A silicon strip detector array for energy verification and quality assurance in heavy ion therapy," *Medical Physics*, vol. 45, no. 2, pp. 953–962, 2018.

[92] J. H. D. Wong *et al.*, "Characterization of a novel two dimensional diode array the "magic plate" as a radiation detector for radiation therapy treatment," *Medical Physics*, vol. 39, no. 5, pp. 2544–2558, 2012.

[93] A. Espinoza *et al.*, "The feasibility study and characterization of a two-dimensional diode array in "magic phantom" for high dose rate brachytherapy quality assurance," *Medical Physics*, vol. 40, no. 11, p. 111 702, 2013.

[94] A. Espinoza *et al.*, "The evaluation of a 2D diode array in "magic phantom" for use in high dose rate brachytherapy pretreatment quality assurance," *Medical Physics*, vol. 42, no. 2, pp. 663–673, 2015.

[95] M. Gargett, B. Oborn, P. Metcalfe, and A. Rosenfeld, "Monte Carlo simulation of the dose response of a novel 2D silicon diode array for use in hybrid MRI-LINAC systems," *Medical Physics*, vol. 42, no. 2, pp. 856–865, 2015.

[96] A. H. Aldosari *et al.*, "A two dimensional silicon detectors array for quality assurance in stereotactic radiotherapy: MagicPlate-512," *Medical Physics*, vol. 41, no. 9, p. 091 707, 2014.

[97] M. Petasecca *et al.*, "MagicPlate-512: A 2D silicon detector array for quality assurance of stereotactic motion adaptive radiotherapy," *Medical Physics*, vol. 42, no. 6, pp. 2992–3004, 2015.

[98] N. Stansook *et al.*, "Technical Note: Angular dependence of a 2D monolithic silicon diode array for small field dosimetry," *Medical Physics*, vol. 44, no. 8, pp. 4313–4321, 2017.

[99] M. Gargett *et al.*, “A high resolution 2D array detector system for small-field MRI-linac applications,” *Biomedical Physics & Engineering Express*, vol. 4, no. 3, p. 035 041, 2018.

[100] S. J. Alnaghy *et al.*, “High resolution silicon array detector implementation in an inline MRI-linac,” *Medical Physics*, vol. 47, no. 4, pp. 1920–1929, 2020.

[101] K. A. Shukaili *et al.*, “A 2D silicon detector array for quality assurance in small field dosimetry: DUO,” *Medical Physics*, vol. 44, no. 2, pp. 628–636, 2017.

[102] K. A. Shukaili *et al.*, “Characterization of ELEKTA SRS cone collimator using high spatial resolution monolithic silicon detector array,” *Journal of Applied Clinical Medical Physics*, vol. 19, no. 4, pp. 114–124, 2018.

[103] C. S. Porumb *et al.*, “Characterisation of Silicon Diode Arrays for Dosimetry in External Beam Radiation Therapy,” *IEEE Transactions on Nuclear Science*, vol. 63, no. 3, pp. 1808–1817, 2016.

[104] S. J. Alnaghy *et al.*, “A feasibility study for high-resolution silicon array detector performance in the magnetic field of a permanent magnet system,” *Medical Physics*, vol. 46, no. 9, pp. 4224–4232, 2019.

[105] I. Fuduli *et al.*, “Multichannel data acquisition system comparison for quality assurance in external beam radiation therapy,” *Radiation Measurements*, vol. 71, pp. 338–341, 2014, Proceedings of the 17th Solid State Dosimetry Conference (SSD17).

[106] I Fuduli *et al.*, “A comparative analysis of multichannel data acquisition systems for quality assurance in external beam radiation therapy,” *Journal of Instrumentation*, vol. 9, no. 06, T06003–T06003, 2014.

[107] P. J. Keall, M. Barton, and S. Crozier, “The Australian Magnetic Resonance Imaging–Linac Program,” *Seminars in Radiation Oncology*, vol. 24, no. 3, pp. 203–206, 2014.

[108] J. Bourhis *et al.*, “Treatment of a first patient with flash-radiotherapy,” *Radiotherapy and Oncology*, vol. 139, pp. 18 –22, 2019, FLASH radiotherapy International Workshop.

[109] N. Esplen, M. S. Mendonca, and M. Bazalova-Carter, “Physics and biology of ultrahigh dose-rate (FLASH) radiotherapy: A topical review,” *Physics in Medicine & Biology*, vol. 65, no. 23, 23TR03, 2020.

[110] T. Inaniwa *et al.*, “Enhancement of biological effectiveness of carbon-ion beams by applying a longitudinal magnetic field,” *International Journal of Radiation Biology*, vol. 95, no. 6, pp. 720–724, 2019.

[111] C. Theriault, E. Paetzell, R. Chandrasekar, C. Barkey, Y. Oni, and W. O. Soboyejo, "An in-vitro study of the effects of temperature on breast cancer cells: Experiments and models," *Materials Science and Engineering C*, vol. 32, no. 8, pp. 2242–2249, 2012.

[112] F. Therriault-Proulx, Z. Wen, G. Ibbott, and S. Beddar, "Effect of magnetic field strength on plastic scintillation detector response," *Radiation Measurements*, vol. 116, pp. 10–13, 2018.

[113] J Agnew, F O'Grady, R Young, S Duane, and G. J. Budgell, "Quantification of static magnetic field effects on radiotherapy ionization chambers," *Physics in Medicine and Biology*, vol. 62, no. 5, pp. 1731–1743, 2017.

[114] S. L. Hackett *et al.*, "Consequences of air around an ionization chamber: Are existing solid phantoms suitable for reference dosimetry on an MR-linac?" *Medical Physics*, vol. 43, no. 7, pp. 3961–3968, 2016.

[115] M. S. Weinhous and J. A. Meli, "Determining pion, the correction factor for recombination losses in an ionization chamber," *Medical Physics*, vol. 11, no. 6, pp. 846–849, 1984.

[116] H. Palmans, P. Andreo, M. S. Huq, J. Seuntjens, K. E. Christaki, and A. Meghzifene, "Dosimetry of small static fields used in external photon beam radiotherapy: Summary of TRS-483, the IAEA–AAPM international Code of Practice for reference and relative dose determination," Tech. Rep. 11, 2018, e1123–e1145.

[117] J. Olsen, O. Green, and R. Kashani, "World's First Application of MR-Guidance for Radiotherapy.," *Missouri medicine*, vol. 112, no. 5, pp. 358–60, 2015.

[118] S. M. Bentzen *et al.*, "Quantitative Analyses of Normal Tissue Effects in the Clinic (QUANTEC): an introduction to the scientific issues.," *International journal of radiation oncology, biology, physics*, vol. 76, no. 3 Suppl, S3–9, 2010.

[119] I Fuduli *et al.*, "A comparative analysis of multichannel Data Acquisition Systems for quality assurance in external beam radiation therapy," *Journal of Instrumentation*, vol. 9, no. 06, T06003–T06003, 2014.

[120] J. Allison *et al.*, "Recent developments in GEANT4," *Nuclear Instruments and Methods in Physics Research, Section A: Accelerators, Spectrometers, Detectors and Associated Equipment*, vol. 835, pp. 186–225, 2016.

[121] H. Treuer *et al.*, "On isocentre adjustment and quality control in linear accelerator based radiosurgery with circular collimators and room lasers," *Physics in Medicine and Biology*, vol. 45, no. 8, pp. 2331–2342, 2000.

[122] H. M. Van Zijp *et al.*, “Minimizing the magnetic field effect in MR-linac specific QA-tests: The use of electron dense materials,” *Physics in Medicine and Biology*, vol. 61, no. 3, N50–N59, 2016.

[123] “Operator’s Manual for the MRIdian® System 4.5,” Tech. Rep., 2016.

[124] D. A. Roberts *et al.*, “Machine qa for the elekta unity system: A report from the elekta mr-linac consortium,” *Medical Physics*, vol. 48, e67–e85, 5 May 2021.

[125] R. H. Tijssen *et al.*, “Mri commissioning of 1.5t mr-linac systems – a multi-institutional study,” *Radiotherapy and Oncology*, vol. 132, pp. 114–120, Mar. 2019.

[126] K. Latifi, E. G. Moros, G. Zhang, L. Harrison, and V. Feygelman, “A Method to Determine the Coincidence of MRI-Guided Linac Radiation and Magnetic Isocenters,” *Technology in cancer research & treatment*, vol. 18, 2019.

[127] S. Dorsch *et al.*, “Measurement of isocenter alignment accuracy and image distortion of an 0.35 T MR-Linac system,” *Physics in Medicine and Biology*, vol. 64, no. 20, p. 205 011, 2019.

[128] G. P. Liney *et al.*, “Imaging performance of a dedicated radiation transparent RF coil on a 1.0 Tesla inline MRI-linac,” *Physics in Medicine and Biology*, vol. 63, no. 13, p. 135 005, 2018.

[129] E. E. Klein *et al.*, “Task group 142 report: Quality assurance of medical acceleratorsa),” *Medical Physics*, vol. 36, no. 9Part1, pp. 4197–4212, 2009.

[130] I. E. Commission, *Medical electrical equipment: Part 2-33. particular requirements for the safety of magnetic resonance equipment for medical diagnosis*, 2010.

[131] D. Wang and D. Doddrell, “Geometric Distortion in Structural Magnetic Resonance Imaging,” *Current Medical Imaging Reviews*, vol. 1, no. 1, pp. 49–60, 2005.

[132] M. O’donnell and W. A. Edelstein, “NMR imaging in the presence of magnetic field inhomogeneities and gradient field nonlinearities,” *Medical Physics*, vol. 12, no. 1, pp. 20–26, 1985.

[133] A. Janke, H. Zhao, G. J. Cowin, G. J. Galloway, and D. M. Doddrell, “Use of spherical harmonic deconvolution methods to compensate for nonlinear gradient effects on MRI images,” *Magnetic Resonance in Medicine*, vol. 52, no. 1, pp. 115–122, 2004.

[134] M. N. Hood, V. B. Ho, J. G. Smirniotopoulos, and J. Szumowski, "Chemical shift: The artifact and clinical tool revisited," *Radiographics*, vol. 19, no. 2, pp. 357–371, 1999.

[135] K. Krupa and M. Bekiesińska-Figatowska, "Artifacts in magnetic resonance imaging," *Polish Journal of Radiology*, vol. 80, no. 1, pp. 93–106, 2015.

[136] E. Jackson *et al.*, *AAPM report 100 - Acceptance Testing and Quality Assurance Procedures for Magnetic Resonance Imaging Facilities.* 2010.

[137] S. Shan *et al.*, "Geometric distortion characterization and correction for the 1.0 T Australian MRI-linac system using an inverse electromagnetic method," *Medical Physics*, vol. 47, no. 3, pp. 1126–1138, 2020.

[138] U. Jelen *et al.*, "Dosimetric optimization and commissioning of a high field inline mri-linac," *Frontiers in Oncology*, vol. 10, 2020.

[139] J. H. D. Wong *et al.*, "Characterization of a novel two dimensional diode array the "magic plate" as a radiation detector for radiation therapy treatment," *Medical Physics*, vol. 39, no. 5, pp. 2544–2558, 2012.

[140] B. M. Oborn *et al.*, "Experimental verification of dose enhancement effects in a lung phantom from inline magnetic fields," *Radiotherapy and Oncology*, vol. 125, no. 3, pp. 433–438, 2017.

[141] R. Kueng *et al.*, "Towards MR-guided electron therapy: Measurement and simulation of clinical electron beams in magnetic fields," *Physica Medica*, vol. 78, pp. 83–92, 2020.